

Diss. ETH No. 18396

H₂ PRODUCTION BY THE TWO-STEP
WATER-SPLITTING THERMOCHEMICAL CYCLE
BASED ON Zn/ZnO REDOX REACTIONS

A dissertation submitted to
ETH ZURICH

for the degree of
Doctor of Sciences

presented by
TOM MELCHIOR
Dipl. Masch.-Ing. ETH
born September 2, 1979
citizen of Luxembourg

accepted on the recommendation of
Prof. Dr. Aldo Steinfeld, examiner
Prof. Dr. Alan W. Weimer, co-examiner

2009

Abstract

Hydrogen production by the two-step water-splitting thermochemical cycle based on ZnO/Zn redox reactions is considered. The cycle consists of the following two steps: (1) endothermic ZnO dissociation in a solar chemical reactor, and (2) exothermic hydrolysis of Zn in a non-solar reactor. In the framework of the present work, several investigations considering both steps of the cycle are performed. With regard to the first step, thermal performance of an indirectly-irradiated reactor concept is assessed in experimental and numerical investigations. The second step of the cycle is examined in a hot-wall flow tubular reactor, aiming at the efficient co-synthesis of H₂ and Zn/ZnO nanoparticles.

A solar chemical reactor consisting of a cylindrical cavity-receiver containing a tubular opaque absorber is considered for performing thermochemical processes using concentrated thermal radiation as the energy source of high-temperature process heat. A lab-scale 5 kW reactor prototype is fabricated and tested in ETH's High Flux Solar Simulator. A 2D steady-state heat transfer reactor model is formulated that encompasses the governing mass and energy conservation equations coupling radiation/convection/conduction heat transfer to the chemical kinetics, and their solution by Monte Carlo ray-tracing and finite difference techniques. An Al₂O₃ absorber, withstanding temperatures above 2000 K, was used in ZnO decomposition experiments. The cavity was made of 10 wt% YO₂-stabilized ZrO₂. Validation of the reactor model was accomplished by comparing numerically computed and experimentally measured reaction rates, determined in batch-mode experiments with pre-sintered ZnO plates in the 1780–1975 K range, and temperatures, obtained in continuous-mode runs under pure Ar flow without chemical reaction. The reactor model is utilized to simulate a continuous chemical process. Nearly completion of the reaction extent and maximum solar-to-chemical energy conversion efficiency of 28.5% are found for a reactor temperature of 2300 K. Major sources of irreversibility were associated with re-radiation losses through the cavity's aperture and conduction through reactor walls. In contrast to 2D model predictions, where uniform temperature is assumed for carrier gas, reactants and inner absorber walls, continuous-mode ZnO dissociation experiments proved unsuccessful due to inefficient heat transfer.

The steam-gasification of biochar was selected as chemical reaction for continuous-mode operation. Particles of beech charcoal were used as the biomass feedstock in a continuous steam-particle flow through the tubular absorber. The reaction product is synthesis

gas (syngas) – mainly H₂ and CO. Silicon carbide was used as absorber material. Although its maximum applicable temperature is lower than that of alumina, the thermal conductivity is higher giving better resistance to thermal shocks. Experiments were carried out in the 1074–1523 K range. The reactor model was validated by comparing numerically computed and experimentally measured temperatures and carbon conversions. Maximum carbon conversion of 26% was found experimentally. Solar-to-chemical energy conversion efficiency was low with a maximum of 1.53%. The simulation model is further applied to assess the thermal performance of 100 kW and 1 MW scaled-up solar reactor containing multiple tubular absorbers, yielding a theoretical maximum energy conversion efficiency of 39.1 and 50.1%, respectively. Compared to the lab-scale reactor, conduction losses were significantly reduced due to the larger cavity volume-to-surface ratio. Consequently, major heat losses were only re-radiation losses through the aperture.

The second step of the two-step thermochemical cycle, hydrogen production by steam-hydrolysis of zinc, was investigated in an aerosol flow reactor. This hydrolysis reactor consists of a hot-wall tube containing a flow of Zn(g) that is steam-quenched to co-produce H₂ and Zn/ZnO nanoparticles. The effects of the quenching gas flow rate and reactor wall temperature on the Zn-to-ZnO chemical conversion and particle yield were examined. Solid products were characterized by X-ray diffraction, N₂ adsorption, and scanning electron microscopy. Quench rates of $2 - 6 \times 10^4$ K/s yielded overall chemical conversions of up to 95% at the expense of low particle yield due to significant wall deposition with subsequent hydrolysis. Aerosol particles with hexagonal structure were formed by Zn evaporation-condensation containing low ZnO mass fraction. In contrast, operation at quench rates up to 10^6 K/s led to increased particle yield but lower conversion. Filamentary and rod-like particles were formed with high ZnO content of up to 50% by surface reaction and coagulation. Major problems were related to wall depositions and low H₂ yield derived exclusively from hydrolysis of gas-borne particles collected in the filter.

A simple 1D monodisperse model accounting for coagulation, sintering, surface chemical reaction, and vapor and particle wall deposition by diffusion was utilized for reaction zone simulations. Validation was accomplished by comparing experimentally measured and numerically calculated overall chemical conversions and particle ZnO contents. The good agreement between these values was however accompanied by discrepancies in particle sizes. Sintering was found to be slow or even non-existent at prevailing reaction zone conditions. The influence of initial primary particle size, initial particle fraction and sintering rate on evolution of particle morphology was investigated.

Zusammenfassung

Die vorliegende Arbeit befasst sich mit der Wasserstoffherstellung durch Wasserspaltung in einem zweistufigen thermochemischen Zyklus mittels ZnO/Zn Redoxreaktionen. Der Zyklus besteht aus folgenden Schritten: (1) die endotherme Dissoziation von ZnO in einem solar-chemischen Reaktor, und (2) die exotherme Hydrolyse mit Zn in einem nicht-solaren Reaktor. Verschiedene Untersuchungen beide Schritte betreffend wurden im Rahmen dieser Arbeit durchgeführt. Hinsichtlich des ersten Schritts wurde die thermische Leistungsfähigkeit eines Reaktorkonzepts mit indirekter Bestrahlung mittels experimenteller und numerischer Untersuchungen beurteilt. Der zweite Zyklusschritt wurde in einem Strömungsreaktor mit beheizten Rohrwänden untersucht, mit dem Ziel einer effizienten, simultan erfolgenden Herstellung von H₂ und Zn/ZnO-Nanopartikeln.

Ein solar-chemischer Reaktor, bestehend aus einem zylindrischen Hohlraum-Receiver, der ein lichtundurchlässiges Absorberrohr enthält, wird zur Ausführung thermochemischer Prozesse in Betracht gezogen, in denen durch konzentrierte Wärmestrahlung bereitgestellte Hochtemperaturwärme genutzt wird. Ein im Labormassstab angefertigter 5 kW-Reaktorprototyp wurde im ETH-Solarsimulator getestet. Ein stationäres 2D-Wärmetransfer-Reaktormodell wurde entwickelt, welches die Strahlungs-, Wärmeleitungs- und Konvektionswärmeströme mit der chemischen Reaktionskinetik koppelt. Die relevanten Erhaltungsgleichungen wurden mittels Monte-Carlo-Ray-Tracing- sowie Finite-Differenzen-Methoden gelöst. Experimente zur ZnO-Zersetzung wurden mit einem Al₂O₃-Absorber durchgeführt, der Temperaturen über 2000 K standhält. Die Kavität besteht aus mit 10 Gewichtsprozent YO₂ stabilisiertem ZrO₂. Die Validierung des Reaktormodells wurde durch den Vergleich numerisch berechneter und experimentell gemessener Reaktionsraten (Batch-Modus) sowie Temperaturen (kontinuierlicher Strom) ausgeführt. Hierbei wurden die Reaktionsraten im Batch-Modus mit vorgesinterten ZnO-Plättchen in einem Temperaturbereich zwischen 1780 und 1975 K bestimmt, während Temperaturmessungen mit einem kontinuierlichen Argon-Strom ohne chemische Reaktion durchgeführt wurden. Das Reaktormodell wurde anschliessend zur Simulation eines kontinuierlichen chemischen Prozesses genutzt. Die Simulationen ergaben einen fast kompletten Reaktionsumsatz sowie einen maximalen Umwandlungswirkungsgrad von solarer zu chemischer Energie von 28.5% bei einer Reaktortemperatur von 2300 K. Die Hauptwärmeverluste sind durch Rückstrahlung

aus der Kavitätapertur und Wärmeleitung durch die Reaktorwände bedingt. Im Gegensatz zu den Voraussagen des 2D-Modells, in dem eine uniforme Temperatur in der Reaktionszone für Trägergas, Reaktanden und Absorberwand angenommen wurde, verliefen Experimente zur ZnO-Zersetzung im kontinuierlichen Strom aufgrund ineffizienten Wärmeübergangs nicht erfolgreich.

Die Wasserdampf-Vergasung von Kohle wurde als Modellreaktion für einen kontinuierlichen Prozess ausgesucht. Buchenholzkohlepartikel dienten als Biomasse-Ausgangsmaterial für den kontinuierlichen Wasserdampf- und Partikel-Strom im Absorberrohr. Das Reaktionsprodukt, hauptsächlich H_2 und CO , wird als Synthesegas bezeichnet. Als Absorbermaterial wurde Siliziumkarbid verwendet. Die maximal anwendbare Temperatur ist zwar niedriger als beim Aluminiumoxid, jedoch ist die thermische Leitfähigkeit höher, was zu einer Verbesserung der thermischen Stabilität führt. Die Experimente wurden in einem Temperaturbereich zwischen 1074 und 1523 K ausgeführt. Das Reaktormodell wurde durch den Vergleich numerisch berechneter und experimentell gemessener Temperaturen und Karbonumsätze verifiziert. Experimentell belief sich der maximale Karbonumsatz auf 26%. Der Umwandlungswirkungsgrad von solarer zu chemischer Energie war niedrig und belief sich maximal auf 1.53%. Des Weiteren wurde das Modell zur Leistungsbestimmung einer Aufskalierung der Reaktortechnologie genutzt. Anstelle des Einzelrohrabsorbers enthalten die aufskalierten Reaktoren ein Rohrbündel. Maximale Umwandlungswirkungsgrade von jeweils 39.1 und 50.1% wurden für Einstrahlungsleistungen von 100 kW und 1 MW bestimmt. Wärmeverluste sind hauptsächlich auf Rückstrahlung aus der Apertur zurückzuführen, da Wärmeleitungsverluste entscheidend verringert wurden durch das vergrößerte Verhältnis zwischen Kavitätvolumen und -oberfläche.

Der zweite Schritt des thermochemischen Zweistufen-Zyklus, die Wasserstoffproduktion durch Wasserdampf-Hydrolyse mit Zink, wurde in einem Aerosol-Strömungsreaktor untersucht. In diesem Heisswandreaktor wird ein Zinkdampfstrom durch Wasserdampf abgekühlt zur simultanen Wasserstoff- und Zn/ZnO-Nanopartikelproduktion. Der Einfluss der Kühlgasdurchflussmenge und der Reaktorwandtemperatur auf die Partikelausbeute sowie den Umsatz von Zn zu ZnO wurden untersucht. Die Partikeleigenschaften wurden durch Röntgenbeugungsanalyse, N_2 -Adsorption, und Rasterelektronenmikroskopie bestimmt. Kühlraten im Bereich von 2 bis 6×10^4 K/s resultierten in chemischen Gesamtumsätzen von bis zu 95%, jedoch auf Kosten der Partikelausbeute wegen erheblicher Wandablagerungen mit anschließender Hydrolyse. Die

bei diesem Verdampfungs-Kondensationsprozess entstandenen Partikel wiesen eine hexagonale Struktur mit niedrigem ZnO-Massengehalt auf. Der Betrieb bei höheren Kühlraten bis zu 10^6 K/s führte zu erhöhter Partikelausbeute jedoch niedrigeren Gesamtumsätzen. In diesen Experimenten entstanden faser- und stabförmige Partikel durch Oberflächenreaktion und Koagulation mit hohem ZnO-Gehalt bis zu 50%. Als Hauptprobleme stellten sich Wandablagerungen und niedrige Wasserstoffausbeute durch alleinige Hydrolyse an den im Filter eingesammelten Partikeln.

Ein einfaches monodisperses 1D-Modell wurde zur Simulation der Reaktionszone benutzt, welches Koagulation, Sintern, Oberflächenreaktion sowie Dampf- und Partikel-Wandablagerung durch Diffusion berücksichtigt. Die Validierung des Modells geschah mittels Vergleich der experimentell gemessenen und numerisch berechneten Gesamtumsätze und ZnO-Gehälter der Partikel. Die gute Übereinstimmung dieser Werte wurde jedoch von einer grossen Diskrepanz zwischen gemessenen und berechneten Partikelgrössen begleitet. Es stellte sich heraus, dass bei den vorherrschenden Gegebenheiten in der Reaktionszone das Sintern nur langsam oder gar nicht erfolgt. Der Einfluss der Anfangsgrösse der Primärpartikel, des Eingangspartikelanteils sowie der Sinterrate auf die Entwicklung der Partikelmorphologie wurde untersucht.

Acknowledgments

I want to express my gratitude to Prof. Aldo Steinfeld, who supervised my doctoral studies at the Professorship in Renewable Energy Carriers, ETH Zurich, and supported me in every aspect of my work. I thank Prof. Alan W. Weimer for his helpful discussions and suggestions, for critically reviewing this manuscript, and for acting as co-examiner.

Special thanks go to Prof. Sotiris E. Pratsinis and Dr. Frank O. Ernst from the Particle Technology Laboratory for the fruitful discussions on nanoparticle production and for the collaboration in the Zn-hydrolysis experimental campaign.

I am grateful to Dr. Christopher Perkins and Paul Lichty from the University of Colorado at Boulder for the design and construction of the solar cavity-receiver and the support in the experimental campaign.

Further I thank all my colleagues and members of the PRE group. In particular, my thanks go to Dr. Viktoria von Zedtwitz-Nikulshyna for being a great office mate and providing a great working ambiance every day. Nic Piatkowski also deserves special thanks for his effort during his diploma thesis. I thank Dr. Wojciech Lipinski, Dr. Reto Müller, Dr. Jörg Petrasch, Dr. Lothar Schunk, Dr. Dominic Trommer, Dr. Peter von Zedtwitz, Dr. Andreas Z'Graggen, Dr. Elena Gálvez, Dr. Peter Loutzenhiser, Dr. Hyung Chul Yoon, Philipp Haueter, Hansmartin Friess, Roman Bader, Patrick Coray, Christoph Gebald, Sophia Haussener, Illias Hischier, Gilles Maag, Anastasia Stamatiou, Clemens Suter, Jan Wurzbacher and Laurenz Schlumpf for providing an inspiring working environment. I want to acknowledge the contributions to the present work by the undergraduate students Enrico Guglielmini, Daniel Hess and Valerio Gianini.

Finally, my very special thanks go to my family, especially to my parents for their continuous and ongoing support.

Contents

Abstract.....	i
Zusammenfassung.....	iii
Acknowledgments.....	vii
Nomenclature.....	xi
1 Introduction	1
Part I A cavity-receiver containing a tubular absorber for high- temperature thermochemical processing using concentrated solar energy ..	5
2 Solar reactor	7
2.1 Solar reactor technology.....	7
2.2 Solar reactor configuration.....	8
3 Reactor modeling.....	11
3.1 Monte Carlo.....	11
3.2 Energy conservation.....	13
4 Solar thermal ZnO dissociation	19
4.1 Introduction	19
4.2 Experimental setup.....	20
4.3 Numerical results and experimental validation.....	21
4.4 Numerical simulation of the continuous chemical process.....	23
4.5 Continuous chemical process experiments	26
4.6 Summary and conclusions.....	28
5 Model validation – Solar-driven biochar gasification	29
5.1 Introduction	29
5.2 Thermodynamics and kinetics analyses	30
5.3 Experimental setup.....	31
5.4 Experimental validation of solar reactor model	34
5.5 Reactor scale-up	39
5.6 Summary and conclusions.....	43

Part II	Zn hydrolysis	45
6	H₂ production by steam-quenching of Zn vapor in a hot-wall aerosol flow reactor	47
6.1	Introduction	47
6.2	Experimental	48
6.3	Results and discussion.....	51
6.4	Summary and conclusions.....	61
7	Reaction zone modeling	63
7.1	Introduction	63
7.2	Model	64
7.3	Results and discussion.....	69
7.4	Summary and conclusions.....	78
8	Summary and outlook.....	81
	Appendix	85
	Bibliography	87
	Curriculum vitae	99

Nomenclature

Acronyms

BET	Brunauer-Emmet-Teller
CFD	Computational Fluid Dynamics
CPC	Compound Parabolic Concentrator
ETH	Eidgenössische Technische Hochschule
GC	Gas Chromatography
GHG	Greenhouse Gas
HFSS	High-Flux Solar Simulator
IR	Infrared
MC	Monte Carlo ray tracing
SEM	Scanning Electron Microscope
SSA	Specific Surface Area
TG	Thermogravimetry
VS	Vapor-Solid mechanism
XRD	X-Ray Diffraction

Latin characters

a	conductance coefficient, W/(m K)
a_{agg}	surface area of an aggregate, m^2
a_{sp}	surface area of completely fused aggregate, m^2
A	surface area, m^2
A_{aerosol}	aerosol surface area concentration per unit mass of carrier gas, m^2/kg
A_i	surface area per unit length of control volume i , m^2/m
A_{ZnO}	reactant surface area per unit length, m^2/m
b	grain-boundary width, m
c	particle velocity, m/s
c_p	heat capacity, J/(mol K)
C_c	Cunningham correction factor
C_x	concentration of species x per unit mass of carrier gas, mol/kg
d_{BET}	diameter calculated from SSA, m

d_{col}	collision diameter, m
d_{m}	Zn monomer diameter, m
d_{N_2}	N ₂ molecular diameter, m
d_{p}	particle diameter, m
d_{prim}	primary particle diameter, m
d_{t}	tube diameter, m
d_{Zn}	Zn crystallite size, m
d_{ZnO}	ZnO crystallite size, m
D	monomer diffusion coefficient, m ² /s
D_{f}	mass fractal-like dimension
D_{GB}	grain-boundary diffusion coefficient, m ² /s
D_{p}	particle diffusion coefficient, m ² /s
$e_{\lambda\text{b}}$	Planck's blackbody emissive power, W/(m ² μm)
E_{a}	apparent activation energy, J/mol
$F_{0-\lambda T}$	blackbody fractional function $F_{0-\lambda T} = \int_0^{\lambda} e_{\lambda\text{b}}(T) d\lambda / \sigma T^4$
$F_{0-\lambda T}^{-1}$	inverse fractional function
g	acceleration due to gravity, m/s ²
g_{trans}	transition parameter, m
G	velocity gradient, 1/s
h	convective heat transfer coefficient, W/(m ² K)
k	thermal conductivity, W/(m K)
k'	rate constant, 1/s
k_{B}	Boltzmann constant, 1.38×10^{-23} J/K
k_{s}	pre-exponential factor, mol/(m ² s)
k_0	pre-exponential factor, 1/s
K_{m}	monomer mass transfer coefficient, m/s
K_{p}	particle mass transfer coefficient, m/s
Kn	Knudsen number
l	reaction zone length, m
L	characteristic length, cm

m	number of grid points in radial direction
\dot{m}_{Ar}	Ar mass flow rate, g/min
$\dot{m}_{\text{charcoal}}$	charcoal feeding rate, g/min
M	molar mass, kg/mol
n	number of grid points in angular direction
n_{prim}	number of primary particles per aggregate
\dot{n}_x	molar flow rate of species x , mol/s
$\dot{n}_{0,x}$	inlet molar flow rate of species x , mol/s
N	total number concentration of aggregates per unit mass of carrier gas, #/kg
N_A	Avogadro number, $6.022 \times 10^{23} \text{ mol}^{-1}$
N_{ray}	sample of rays
Nu	Nusselt number
p_{Zn}	Zn vapor pressure, mmHg
P	total pressure, Pa
Pe	Peclet number
Pr	Prandtl number
q	heat flux, W/m ²
Q	power, W
Q'	power per unit length, W/m
r	radius; polar coordinate, m
\dot{r}	decomposition rate, g/(m ² s)
\dot{r}_s	reaction rate, mol/(m ² s)
R_u	universal gas constant, J/(mol K)
\mathfrak{R}_λ	random number from a uniform set [0, 1]
Ra	Rayleigh number
Re	Reynolds number
Sc	Schmidt number
Sh	Sherwood number
t	time, s
T	temperature, K

u	velocity, m/s
u_{salt}	saltation velocity, m/s
v_{agg}	aggregate volume, m^3
v_{prim}	primary particle volume, m^3
v_{Zn}	Zn monomer volume, m^3
v_{ZnO}	ZnO monomer volume, m^3
V	total aggregate volume concentration per unit mass of carrier gas, m^3/kg
\dot{V}	gas flow rate, $\text{l}_\text{n}/\text{min}$
w_{ap}	aperture width, m
x	axial coordinate, m
x_{ZnO}	ZnO mass fraction, wt %
X	overall chemical conversion
y_x	mole fraction of species x
Y	effective particle yield
$Y_{\text{p},0}$	initial particle fraction
Z	ZnO mole fraction

Greek characters

β	volumetric thermal expansion coefficient, $1/\text{K}$
β_{B}	Brownian coagulation coefficient, m^3/s
β_{coag}	coagulation coefficient, m^3/s
β_{sh}	shear-induced coagulation coefficient, m^3/s
γ	ZnO surface tension, J/m^2
δ	annular gap size, m
δ_{ij}	Kronecker function ($\delta_{ij} = 1$ for $i = j$; $\delta_{ij} = 0$ for $i \neq j$)
ΔG^0	Gibbs free energy change, kJ/mol
ΔH	enthalpy change, kJ/mol
ΔH_{R}	reaction enthalpy, kJ/mol
$\Delta H_{298\text{K}}^{\circ}$	standard enthalpy of formation at 298 K, kJ/mol
Δl	length of finite reaction zone section, m

Δr	radial mesh size, m
Δt	residence time in section of length Δl , s
ΔX	increase in conversion in section of length Δl
$\Delta \varphi$	angular mesh size, rad
ε	emissivity
η	energy conversion efficiency
θ	CPC acceptance angle, rad
λ	wavelength, m
λ_c	cut-off wavelength, m
λ_{gas}	gas mean free path, m
λ_p	particle mean free path, m
μ	dynamic viscosity, kg/(m s)
ν	kinematic viscosity, m ² /s
ρ	density, kg/m ³
ρ_{CPC}	CPC total hemispherical reflectivity
σ	Stefan-Boltzmann constant, 5.67×10^{-8} W/(m ² K ⁴)
τ	relaxation time, s
τ_{sin}	characteristic sintering time, s
φ	polar coordinate, rad

Subscripts and superscripts

a	absorber
agg	aggregate
ap	aperture
array	eight-tube absorber array
c	cavity
C	carbon
cp	center point
evap	evaporated
EZ	evaporation zone
f	in the filter

<i>f</i>	iteration step
<i>g</i>	gaseous phase
<i>i</i>	angular index of a grid point
in	inner side of absorber/cavity
<i>j</i>	radial index of a grid point
max	theoretical maximum amount
out	outer side of absorber/cavity
<i>p</i>	particle
prim	primary particle
<i>q</i>	quench gas
RZ	reaction zone
<i>s</i>	surface
sat	saturation
sg	surface growth
solid	solid phase
sur	surroundings
<i>w</i>	wall
<i>x</i>	species
λ	spectral
0	at reaction zone inlet
3mm	3 mm behind the inner cavity surface

1 Introduction

Total world energy consumption was 16 TW in 2005, and is projected to expand by 50% to 24 TW from 2005 to 2030 [1], mostly due to growth in world population and economic development. Today 80–90% of the energy demand is covered by fossil fuels such as oil, natural gas and coal, which mankind is consuming rapidly. Problems with energy supply are related not only to the limited reserve of fossil fuels, but also to environmental concerns such as global warming and pollution. Greenhouse gas (GHG) emissions show an increase well-proportioned with the quantity of fossil fuel consumption [2], which accounts for 56.6% of the GHG emissions [3]. One of the greatest impacts from fossil fuel combustion is the release of the GHG carbon dioxide. It is estimated that CO₂ contributes about 50% to the anthropogenic GHG effect [4]. Adding to the complexity of this problematic situation is the fact that large amounts of oil and gas reserves are located in politically unstable regions like the Gulf region.

Thus, the impacts on the environment by fossil fuel consumption combined with the foreseeable depletion of the reserves require a transition to environmentally appropriate technologies based on renewable sources. An attractive and promising way is the use of concentrated solar radiation to produce solar fuels, for example the solar-thermal production of renewable hydrogen [5]. Hydrogen as a fuel for highly efficient fuel cells, combustion engines or even turbines, has received a great deal of attention due to the growing concerns about the global warming effect and exhausting crude oil stocks. Nowadays, approximately 99% of hydrogen is produced from fossil fuels, mainly by steam-reforming of natural gas. Several routes for solar thermochemical production of hydrogen have been examined [6], and can be categorized under five main pathways: (1) solar decomposition of fossil fuels (natural gas, oil and other hydrocarbons), (2) steam-reforming of fossil fuels, (3) steam-gasification of coal, coke and other solid carbonaceous materials (e.g. biomass-derived char), (4) water thermolysis, and (5) thermochemical cycles for splitting of water. The hybrid solar/fossil processes (1) – (3) offer a viable route for fossil fuel decarbonization and CO₂ avoidance, and further create a transition path towards solar hydrogen, thus, providing the link between today's fossil-fuel-based technology and tomorrow's solar chemical technology [7]. They offer significant reduction in CO₂ emissions compared to conventional combustion-based processes as the product energy content has been upgraded by the solar input in an amount equal to the enthalpy change of the reaction. Apart from fossil fuels, biomass is an attractive

candidate for the thermal gasification process. It shows the greatest near-term chance of success with selling prices of hydrogen competitive with steam methane reforming [5]. For the single-step thermal dissociation of water (4), the Gibbs free energy change is not zero until it exceeds a temperature of 4300 K [8]. Even though reasonable degrees of dissociation can be achieved at temperatures above 2500 K, these high temperatures still pose severe problems about material for reactor construction and lead to significant re-radiation losses [6]. Water thermolysis is further impeded by the need of an effective technique for high-temperature separation of H₂ and O₂. These problems can be avoided by the use of thermochemical water-splitting cycles (5), among which the two-step cycles are most efficient [9]. These cycles use metal oxide redox reactions, where in the first, solar powered, endothermic step, the metal oxide is thermally dissociated to the metal or lower-valence metal oxide. The second, non-solar, exothermic step is the formation of hydrogen and the metal oxide by hydrolysis of the metal. The metal oxide is recycled to the first step. Hence, water-splitting thermochemical cycles, forming hydrogen and oxygen in different steps, bypass the need for high-temperature H₂/O₂ separation [10].

One of the most favourable candidates for the 2-step cycle is presumably the metal oxide redox pair ZnO/Zn because of its potential for reaching high exergy efficiency and economic competitiveness [8-9]. In addition ZnO is one of the rare oxides for which the Gibbs free energy change of the reaction $\Delta G^0 = 0$ below 2500 K [10]. The first step of the cycle is the endothermic dissociation of ZnO into Zn(g) and O₂ at temperatures above 1800 K using concentrated solar energy as the source of process heat:



The second step is the non-solar, exothermic hydrolysis of Zn at temperatures of about 700 K to form H₂ and ZnO:



Zinc oxide from this step is separated and recycled back to the first step. The chemical thermodynamics have been reported in various studies [8-13]. A second-law analysis of the cycle has shown a maximum exergy conversion efficiency of 29%, when using a solar cavity-receiver operated at 2300 K and subjected to a solar flux concentration ratio of 5000. A well-to-wheel analysis showed that the use of solar hydrogen in fuel cell cars reduces life cycle GHG emissions by 70% compared to advanced fossil fuel powertrains and by more than 90% if car and road infrastructure are not considered [14].

Thesis outline – This thesis is divided into two main parts. Part I focuses on solar thermochemical processes. An indirectly-irradiated reactor concept is presented. Results from experimental investigation and numerical simulation of ZnO dissociation (Eq. (1.1)) and steam-gasification of biochar are presented. Part II is dedicated to Zn hydrolysis, which constitutes the second, non-solar step of the Zn/ZnO thermochemical cycle (Eq. (1.2)). A detailed experimental, parametric study was carried out. Further, a simple model was used to simulate chemical reaction and particle dynamics in the reaction zone.

In chapter 2, the design of the cavity-receiver, which contains a tubular absorber that serves as reaction chamber, is described. In addition a short introduction to current solar reactor technology is given.

In chapter 3, a 2D steady-state heat transfer model of the cavity-receiver reactor is presented. It couples radiation, conduction and convection heat transfer to chemical kinetics. The numerical implementation by Monte Carlo ray-tracing and finite difference techniques is described.

Chapter 4 focuses on ZnO decomposition experiments and simulations. A review of earlier work on the first step of the ZnO/Zn thermochemical cycle is given. Experimental setup and procedure are described. Validation of the model presented in chapter 3 is performed in batch-mode experiments and continuous flow experiments without chemical reaction. The reactor model is further applied to simulate a continuous thermochemical process, identify major sources of irreversibility, and predict solar-to-chemical energy conversion efficiencies. Continuous chemical process was tested in the reactor, but proved unsuccessful. Results of these runs are briefly discussed.

The steam-gasification of biochar is considered in chapter 5 as the model reaction for experimental validation of continuous chemical process simulations. A brief introduction to biomass gasification in solar and non-solar applications is given. Thermodynamics and kinetics analyses are followed by a description of the experimental setup and procedure. Numerically computed temperatures and carbon conversions are compared to experimental results. The numerical model is further used to examine the performance of 100 kW and 1 MW reactor scale-up.

Chapter 6 focuses on the experimental investigation of Zn hydrolysis. Previous work on this process is reviewed in the introduction. The hot-wall aerosol flow reactor, featuring three zones for Zn evaporation, particle production by steam-quenching, and chemical reaction, is presented. A description of reactor periphery and analysis methods is provided. Results of parametric investigations are shown and discussed in detail.

A simple 1D monodisperse model is shown and used in chapter 7 to simulate chemical reaction and particle dynamics in the reaction zone of the hydrolysis reactor. Chemical conversions and particle ZnO contents obtained in simulations are compared to experimentally measured values. The effect of several parameters on particle dynamics is investigated. Discrepancies between calculated and measured particle characteristics are discussed.

Finally, chapter 8 gives a summary of the work that has been conducted. Problems encountered in this work are discussed and suggestions for improvement are given.

Part I

A cavity-receiver containing a tubular absorber for high-temperature thermochemical processing using concentrated solar energy

2 Solar reactor¹

2.1 Solar reactor technology

Solar receivers and reactors for highly concentrated solar applications usually feature the use of a cavity-type configuration, i.e. a well insulated enclosure designed to effectively capture incident solar radiation entering through a small opening – the *aperture* [15]. Because of multiple internal reflections, the fraction of the incoming energy absorbed by the cavity exceeds the surface absorptivity of the inner walls [16-18]. The larger the ratio of cavity area to the aperture area, the closer the cavity-receiver approaches a blackbody absorber, but at the expense of higher conduction losses through the insulated cavity walls. Smaller apertures will also reduce re-radiation losses but they intercept less sunlight. Consequently, the optimum aperture size becomes a compromise between maximizing radiation capture and minimizing radiation losses [19]. To some extent, the aperture size may be reduced with the help of non-imaging secondary concentrators, e.g. compound parabolic concentrators (CPC), placed at the receiver's aperture in tandem with the primary concentrating system [20].

Previous solar reactor designs featured the direct irradiation of ZnO through transparent quartz windows [21-25], providing efficient heat transfer directly to the reaction site. However, the window becomes a critical and troublesome component under high-pressure, severe gas environments, and scale-up designs. The use of a protecting partition plate introduced between the window and the reaction chamber has been suggested to bypass this problem [26]. Both directly- and indirectly-irradiated receivers suffer from intrinsic re-radiation losses through the aperture, which to some extent can be minimized by optimizing the geometrical design of the cavity. Examples of such analyses, with and without the use of selective windows, have been previously published [19,26-28].

The reactor design examined in the present study features a cavity-receiver containing an opaque absorber that serves as the reaction chamber. The absorber is exposed to concentrated solar radiation entering through the cavity's aperture and to IR radiation emitted by the hot cavity walls, while heat is transferred by conduction to the reaction chamber. This

¹ Material from this chapter has been published in: T. Melchior, C. Perkins, A.W. Weimer and A. Steinfeld. A cavity-receiver containing a tubular absorber for high-temperature thermochemical processing using concentrated solar energy. *International Journal of Thermal Sciences* **47** (11): 1496-1503 (2008).

Material from this chapter has been submitted for publication: T. Melchior, C. Perkins, P. Lichty, A.W. Weimer and A. Steinfeld. Solar-driven biochar gasification in a particle-flow reactor. *Chemical Engineering and Processing* **48** (8): 1279-1287 (2009).

arrangement eliminates the need of a window at the expense of having a less efficient heat transfer through the absorber walls. Thus, the disadvantages are linked to the limitations imposed by the materials of construction of the absorber such as the maximum operating temperature, inertness to the chemical reaction, thermal conductivity, radiative absorptance, and resistance to thermal shocks. This work describes the design and fabrication of a 5 kW reactor prototype based on such a configuration, and presents its thermal performance when subjected to concentrated solar energy.

2.2 Solar reactor configuration

The reactor configuration is shown schematically in Fig. 2.1. The radiation source is ETH's High-Flux Solar Simulator (HFSS) [29]: a high-pressure Argon arc enclosed in a 27 mm-diameter 200 mm-length water-cooled quartz envelope and closed-coupled to a precision optical reflector to produce an intense beam of concentrated thermal radiation, mostly in the visible and IR spectrum, that approaches the heat transfer characteristics of highly concentrating solar systems. The focusing mirror is a horizontal-axis trough of elliptical cross section and is positioned with one of the linear foci coinciding with the arc. The focal plane of the solar simulator is thus defined as the horizontal plane perpendicular to the ellipse's major axis containing the second linear focus. With this arrangement, radiative power fluxes exceeding 4500 kW/m^2 are attained at the focal plane and confined within a 45° rim angle. Power, power fluxes, and temperatures can be adjusted by simply varying the electrical input power to the arc electrodes.

The solar cavity-receiver consists of a cylinder made of 10 wt% YO_2 -stabilized ZrO_2 [30], with an inner radius $r_{c,\text{in}} = 2.54 \text{ cm}$ and an outer radius $r_{c,\text{out}} = 3.81 \text{ cm}$, and lined with Al_2O_3 insulation. It contains a windowless slab (rectangular) aperture of width 1.414 cm and length 15 cm. The impervious tubular absorber is positioned concentric with the cylindrical cavity. Alumina and silicon carbide are selected as absorber materials. The Al_2O_3 absorber (purity level of 99.8%), with an inner radius $r_{a,\text{in}} = 0.9525 \text{ cm}$, an outer radius $r_{a,\text{out}} = 1.27 \text{ cm}$ and a length of 35.5 cm, proves inert to hydrogen, carbon and refractory metals in many severe situations and can be used in both oxidizing and reducing atmospheres [31]. The melting point temperature of alumina is 2330 K, and the thermal conductivity is $8.2 \text{ W m}^{-1} \text{ K}^{-1}$ at 1073 K. The SiSiC absorber (reaction-bonded silicon-infiltrated silicon carbide, HALSIC-I: 88–92 vol% SiC, 12–8% metallic Si [32]), with an inner radius $r_{a,\text{in}} = 0.9 \text{ cm}$ and an outer radius $r_{a,\text{out}} = 1.25 \text{ cm}$, features a higher thermal conductivity of $45.2 \text{ W m}^{-1} \text{ K}^{-1}$ at

1073 K, thus, being more resistant to thermal shocks. However, the maximum operation temperature is lower at 1623 K. A water-cooled trough CPC is incorporated to the cavity's aperture, with its 150×20 mm rectangular entrance at the focal plane of the solar concentrating system, and its exit matching the aperture of the cavity. The result of such an optical arrangement is an augmentation of the mean radiation flux over the aperture by a factor of $\rho_{\text{CPC}}/\sin \theta$, where ρ_{CPC} is the CPC's reflectivity and θ its acceptance angle – in this case equal to the rim angle of the solar concentrating system, 45° . A water-cooled copper plate mounted on top of the reactor serves as protective shield for spilled radiation.

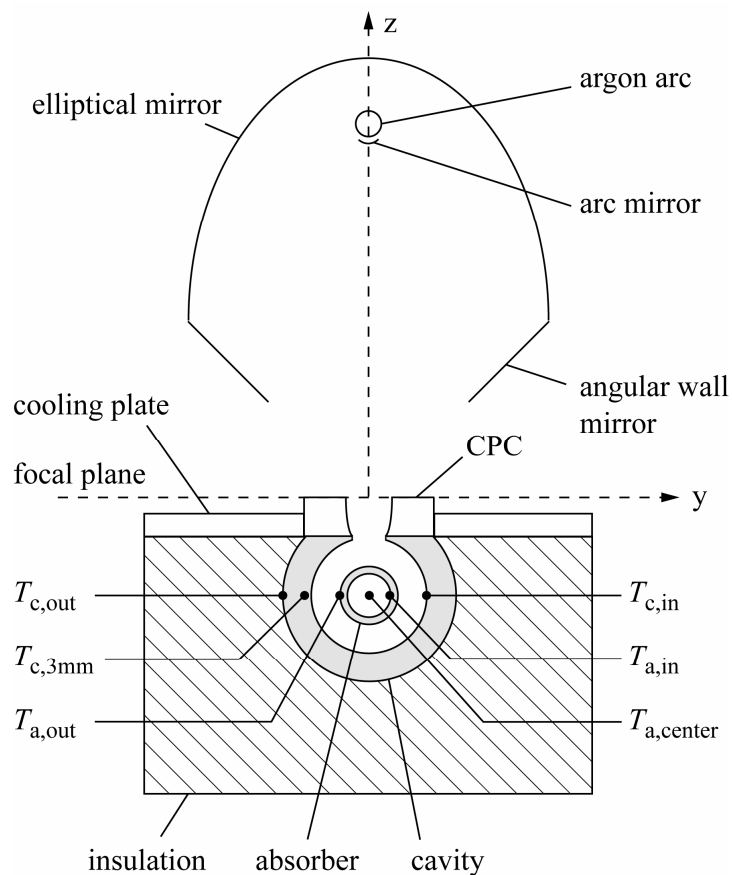


Figure 2.1: Solar reactor configuration: ETH's high-flux solar simulator delivers concentrated thermal radiation to the cavity containing the tubular absorber that serves as the reaction chamber. A CPC is incorporated to the cavity's aperture, with its entrance at the focal plane of the solar concentrating system, and its exit matching the aperture of the cavity (dimensions not to scale).

The incoming radiative flux distribution at the focal plane was measured optically on an Al_2O_3 -plasma-coated Lambertian target with a CCD camera equipped with optical filters and calibrated with a Kendall radiometer. Figure 2.2 shows the measured radiative flux distribution at the CPC entrance for an arc current of 300 A. The peak flux was 1490 kW/m^2 ,

and the mean over the CPC entrance was 1215 kW/m^2 . A mean flux of 1719 kW/m^2 can be achieved at the CPC exit that matches the aperture provided $\rho_{\text{CPC}} = 1$. Integration of the power flux over the CPC entrance (length of 150 mm) yielded a total solar power input, Q_{solar} , of 3.65 kW . Due to the small width of the CPC entrance of 2 cm , slight misalignments can lead to significant changes in solar power input. Therefore, Q_{solar} was averaged in the experimental validation assuming up to 1 cm displacement between the aperture's center and the location of peak radiative flux at the focal plane. The accuracy of the optical measurement combined with the reactor's misalignment led to an error of $\pm_{12}^{19} \%$ for Q_{solar} .

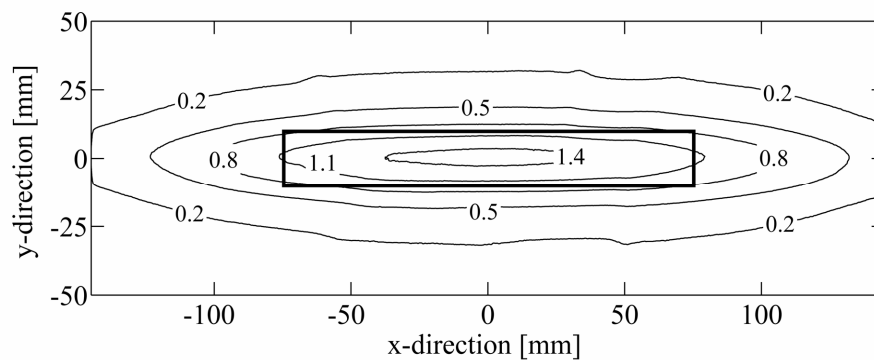


Figure 2.2: Solar radiative flux distribution (in MW/m^2) measured at the focal plane of ETH's High-Flux Solar Simulator. The rectangle with dimensions $150 \times 20 \text{ mm}$ represents the entrance of the CPC.

3 Reactor modeling²

The model domain, consisting of the cavity and absorber as shown in Fig. 2.1, is divided into a large number of control volumes having opaque, isothermal, non-gray, and diffuse surfaces. The nodal points assigned to the center of each control volume are equidistant in the radial (Δr) and angular ($\Delta\varphi$) direction. Two-dimensional steady-state mass and energy conservation equations are formulated for each control volume and solved by Monte Carlo (MC) ray-tracing and finite-difference techniques.

3.1 Monte Carlo

The radiative exchange inside the cavity is solved by applying the 3D collision-based MC ray-tracing method with energy partitioning [33]. The methodology consists of following stochastic paths of a large number of rays as they travel through the interacting boundary surfaces. Each ray, which has an associated direction and wavelength determined from the appropriate probability density functions, undergoes absorption and/or reflection at the absorber and/or cavity surfaces. Specifically, a ray reflected by a surface loses a fraction ε_λ of its power by absorption, where ε_λ is the surface's spectral emissivity. The medium in the annulus between cavity and absorber tube is assumed non-participating. Sources of stochastic rays are incoming solar radiation through the aperture and IR radiation emitted by the inner cavity surface and outer absorber surface. The concentrated solar radiation entering the cavity, Q'_{solar} , is assumed to have a uniform directional distribution over half hemisphere and a uniform power flux distribution over the aperture. Its value is given in power per unit length of the reactor (W/m) for the 2D-simulations. Planck's spectral distribution for a 5780 K blackbody is used to simulate the solar spectrum. The wavelength assigned to a generic ray is found from the inverse fractional function:

²Material from this chapter has been published in: T. Melchior and A. Steinfeld. Radiative transfer within a cylindrical cavity with diffusely/specularly reflecting walls containing an array of tubular absorbers. *ASME Journal of Solar Energy Engineering* **130** (2): 021013 (2008). [28]

Material from this chapter has been published in: T. Melchior, C. Perkins, A.W. Weimer and A. Steinfeld. A cavity-receiver containing a tubular absorber for high-temperature thermochemical processing using concentrated solar energy. *International Journal of Thermal Sciences* **47** (11): 1496-1503 (2008).

Material from this chapter has been submitted for publication: T. Melchior, C. Perkins, P. Lichty, A.W. Weimer and A. Steinfeld. Solar-driven biochar gasification in a particle-flow reactor. *Chemical Engineering and Processing* **48** (8): 1279-1287 (2009).

$$\lambda = F_{0-\lambda T}^{-1}(\mathfrak{R}_\lambda) / T \quad (3.1)$$

for $T = 5780$ K, where \mathfrak{R}_λ denotes a random number chosen from a uniform set $[0, 1]$. For diffuse reflection/emission from a surface, the ray direction is chosen randomly from a set that is weighted according to Lambert's cosine law. The wavelength of emission from a surface is found by solving the implicit equation

$$\mathfrak{R}_\lambda = \frac{\int_0^\lambda \varepsilon_\lambda e_{\text{lb}}(\lambda, T) d\lambda}{\varepsilon \sigma T^4} \quad (3.2)$$

where the Planck's blackbody spectral emissive power $e_{\text{lb}}(\lambda, T)$ is evaluated at the temperature of the location of emission. For the SiC-absorber, Eq. (3.2) is solved by applying the 3-band gray approximation using values of hemispherical spectral emissivity $\varepsilon_{\lambda,1}$, $\varepsilon_{\lambda,2}$ and $\varepsilon_{\lambda,3}$ given in Table 3.1, yielding:

$$\lambda = \begin{cases} \frac{F_{0-\lambda T}^{-1}\left(\frac{\varepsilon}{\varepsilon_{\lambda,1}} \mathfrak{R}_\lambda\right)}{T} & \text{for } \mathfrak{R}_\lambda \leq \varepsilon_{\lambda,1} F_{0-\lambda_{c,1}T} / \varepsilon \\ \frac{F_{0-\lambda T}^{-1}\left[F_{0-\lambda_{c,1}T} + \frac{\varepsilon}{\varepsilon_{\lambda,2}} \left(\mathfrak{R}_\lambda - \frac{\varepsilon_{\lambda,1}}{\varepsilon} F_{0-\lambda_{c,1}T}\right)\right]}{T} & \text{for } \varepsilon_{\lambda,1} F_{0-\lambda_{c,1}T} / \varepsilon < \mathfrak{R}_\lambda \leq \left(\varepsilon_{\lambda,1} F_{0-\lambda_{c,1}T} + \varepsilon_{\lambda,2} F_{\lambda_{c,1}T-\lambda_{c,2}T}\right) / \varepsilon \\ \frac{F_{0-\lambda T}^{-1}\left[F_{0-\lambda_{c,2}T} + \frac{\varepsilon}{\varepsilon_{\lambda,3}} \left(\mathfrak{R}_\lambda - \frac{\varepsilon_{\lambda,1}}{\varepsilon} F_{0-\lambda_{c,1}T} - \frac{\varepsilon_{\lambda,2}}{\varepsilon} F_{\lambda_{c,1}T-\lambda_{c,2}T}\right)\right]}{T} & \text{for } \left(\varepsilon_{\lambda,1} F_{0-\lambda_{c,1}T} + \varepsilon_{\lambda,2} F_{\lambda_{c,1}T-\lambda_{c,2}T}\right) / \varepsilon < \mathfrak{R}_\lambda \end{cases} \quad (3.3)$$

with the total emissivity ε calculated at the surface temperature T ,

$$\varepsilon = \varepsilon_{\lambda,1} F_{0-\lambda_{c,1}T} + \varepsilon_{\lambda,2} F_{\lambda_{c,1}T-\lambda_{c,2}T} + \varepsilon_{\lambda,3} (1 - F_{0-\lambda_{c,2}T}) \quad (3.4)$$

The wavelength of emission from a cavity surface element or an Al_2O_3 -absorber surface element is calculated similarly with the 2-band gray approximations given in Table 3.1.

The power carried per ray is given by:

$$Q'_{\text{ray}} = \frac{Q'_{\text{solar}}}{N_{\text{ray}}} \quad (3.5)$$

where N_{ray} is the sample of incoming rays. Thus, the number of rays emitted by the control volumes on the absorber and cavity surfaces is:

$$N_i = \frac{\varepsilon_i A_i \sigma T_i}{Q'_{\text{ray}}} \quad (3.6)$$

where $A_i = r_{a,\text{out}} \cdot \Delta\varphi_a$ for node i of the absorber, and $A_i = r_{c,\text{in}} \cdot \Delta\varphi_c$ for node i of the cavity. The history of a generic ray is a complete random sequence that terminates when it is absorbed or lost through the aperture to the surroundings. Statistically meaningful results are obtained for sample of rays N_{ray} of 10^5 .

Table 3.1: Gray-band approximations of spectral emissivity of silicon carbide, alumina and zirconia. Values taken from Ref. [34].

	SiC (absorber)	Al ₂ O ₃ (absorber)	ZrO ₂ (cavity)
emissivity $\varepsilon_{\lambda,1}$	0.90	0.40	0.20
emissivity $\varepsilon_{\lambda,2}$	0.60	0.95	0.90
emissivity $\varepsilon_{\lambda,3}$	0.85	-	-
cut-off wavelength $\lambda_{c,1}$ [m]	10.8×10^{-6}	5.0×10^{-6}	6.0×10^{-6}
cut-off wavelength $\lambda_{c,2}$ [m]	14.8×10^{-6}	-	-

3.2 Energy conservation

The overall steady-state energy balance for the system is:

$$\sum Q = 0 = Q_{\text{solar}} - Q_{\text{reradiation}} - Q_{\text{conduction}} - Q_{\text{convection}} - Q_{\text{gas}} - Q_{\text{reactants}} - Q_{\text{chemistry}} \quad (3.7)$$

where Q_{solar} is the solar power input to the cavity, $Q_{\text{reradiation}}$ is the power lost by re-radiation through the aperture, $Q_{\text{conduction}}$ is the total power lost by conduction through the reactor walls, $Q_{\text{convection}}$ is the power lost by natural convection to the surroundings, Q_{gas} is the power transferred by convection to the Ar gas stream inside the absorber, $Q_{\text{reactants}}$ is power used for heating the reactants, and $Q_{\text{chemistry}}$ is the power used for driving the chemical reaction. The steady-state energy conservation equation applied to each sub-system, i.e. the absorber and the cavity, is given by:

$$-\frac{\partial}{\partial r} \left(rk \frac{\partial T}{\partial r} \right) - \frac{\partial}{\partial \varphi} \left(\frac{k}{r} \frac{\partial T}{\partial \varphi} \right) = q \quad (3.8)$$

The discretised subsystems consist of n nodes in angular direction and m nodes in radial direction, with n and m being set to 20 and 10 for the absorber, and 40 and 20 for the cavity.

The boundary conditions are:

at the outer absorber and inner cavity surface,

$$q|_s = q_{\text{emission}} - q_{\text{absorption}} + q_{\text{convection}} \quad (3.9)$$

at the inner absorber surface,

$$q|_s = q_{\text{gas}} + q_{\text{reactants}} + q_{\text{chemistry}} \quad (3.10)$$

at the outer cavity surface,

$$q|_s = q_{\text{conduction}} \quad (3.11)$$

which, when discretised and solved for the node temperature $T_{i,j}$ yields:

$$T_{i,j} = \frac{1}{a_{\text{cp}}} \left(a_{i,j\pm 1} T_{i,j\pm 1} + a_{i-1,j} T_{i-1,j} + a_{i+1,j} T_{i+1,j} - A_i q|_s \right) \quad (3.12)$$

with the coefficients given by:

$$\text{in the radial direction:} \quad a_{i,j\pm 1} = \frac{k_{i,j\pm \frac{1}{2}} r_{i,j\pm \frac{1}{2}} \Delta \varphi}{\Delta r} \quad (3.13)$$

$$\text{in the angular direction:} \quad a_{i\pm 1,j} = \frac{k_{i\pm \frac{1}{2},j} \Delta r}{r_{i\pm \frac{1}{2},j} \Delta \varphi} \quad (3.14)$$

and the center-point coefficient a_{cp} being the sum of all neighbor coefficients. For the calculation of the thermal conductivity $k_{i+\frac{1}{2},j}$ between adjacent nodes, the harmonic mean of $k_{i,j}$ and $k_{i+1,j}$ is taken:

$$k_{i+\frac{1}{2},j}^{-1} = 0.5 \left(k_{i,j}^{-1} + k_{i+1,j}^{-1} \right) \quad (3.15)$$

Thermal conductivities of ZrO_2 , k_{ZrO_2} , SiC , k_{SiC} , and Al_2O_3 , $k_{\text{Al}_2\text{O}_3}$, are taken from Refs. [30,32,35]. For nodes located at the water-cooled copper plate boundary, $T_{i,j}|_{\text{Cu Plate}} = T_{\text{sur}}$. The related conductive heat loss is computed from the temperatures of the neighbouring grid points and the respective interface conductivities. Conduction heat loss through the insulation is calculated using 1D radial steady-state conduction heat transfer. $q_{\text{conduction}}$ is the sum of conduction losses to the copper plate and through the insulation. $q_{\text{absorption},i}$ is found by MC. The radiative flux emitted by surface A_i at $T_{i,1}$ is

$$q_{\text{emission},i} = \varepsilon_i \sigma T_{i,1}^4 \quad (3.16)$$

Natural convection has been considered in previous studies for horizontal concentric and eccentric annuli [36-40], for large cubical cavities [41], for single tube cylindrical frustum shaped receivers [42], for spherical, hemispherical, and cylindrical cavity-receivers [43-46].

However, none of these investigations is applicable for the present geometric configuration that contains a hot body inside the cavity and an upward-facing aperture. Transient 3D natural convective heat transfer was computed [47] using CFD software package ANSYS CFX 10.0 [48]. In this simulation, the inner cavity and outer absorber surfaces were treated as isothermal boundaries. The size of the surroundings and the length in axial direction were increased until they had an insignificant effect on the heat flows and the working fluid. A time step of 0.1s was found to be sufficient for producing accurate results at reasonable computed time. In each time step a convergence criterion of 10^{-4} was imposed on the residuals of the continuity, momentum, energy and mass equations. A period of 5s was considered in the simulation. Steady-state heat transfer was attained after 1s, yielding Nusselt number correlations as function of Rayleigh number (based on the annulus gap size $\delta = r_{c,in} - r_{a,out}$):

$$Ra_{\delta} = \frac{g\beta(T_{a,out} - T_{sur})\delta^3}{\nu^2} \cdot Pr \quad (3.17)$$

and temperature ratio $(T_{a,out} - T_{c,in})/T_{sur}$. Correlations of Nusselt number at the absorber Nu_{δ} (based on δ) and at aperture $Nu_{w_{ap}}$ (based on the aperture width w_{ap}) are:

$$Nu_{\delta} = h \cdot \delta / k_{air} = 0.1331 \cdot Ra_{\delta}^{0.3107} \left(\frac{T_{a,out} - T_{c,in}}{T_{sur}} \right)^{0.3411} \quad (3.18)$$

$$Nu_{w_{ap}} = h \cdot w_{ap} / k_{air} = 0.7515 \cdot Ra_{\delta}^{0.3334} \cdot \left(\frac{T_{a,out} - T_{c,in}}{T_{sur}} \right)^{-0.1386} \quad (3.19)$$

Equations (3.18) and (3.19) are valid for $50 < Ra_{\delta} < 1400$ and $0.65 < (T_{a,out} - T_{c,in})/T_{sur} < 4.00$.

The total natural convective heat loss of the absorber, computed with the heat transfer coefficient h from Eq. (3.18), is partially transferred to the cavity walls and partially lost to the surroundings through the aperture, the latter being computed with h from Eq. (3.19). Figure 3.1 shows the parity plots of the Nusselt number, the correlation coefficient, and the standard deviation of the fit. Properties of air are evaluated at the volume-mean temperature [37]:

$$T_{mean,air} = T_{a,out} - (T_{a,out} - T_{c,in}) \left\{ \frac{1}{1 - (r_{a,out}/r_{c,in})^2} + \frac{1}{2 \ln(r_{a,out}/r_{c,in})} \right\} \quad (3.20)$$

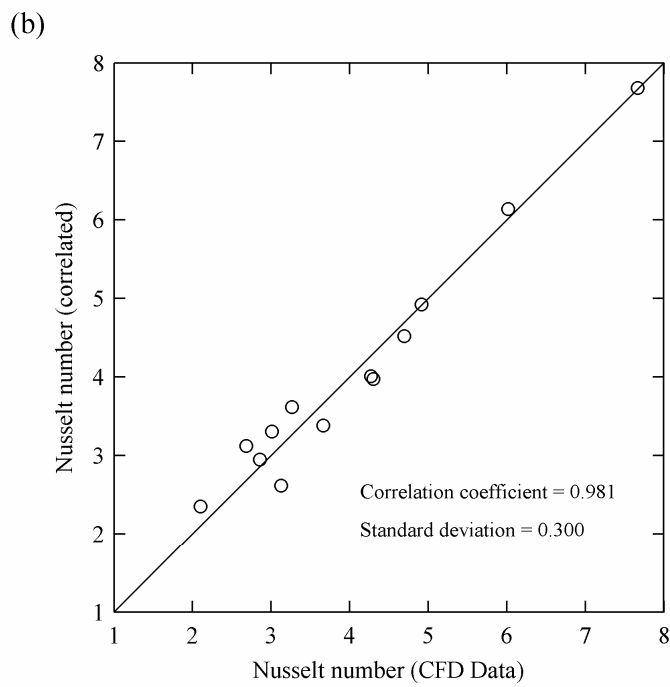
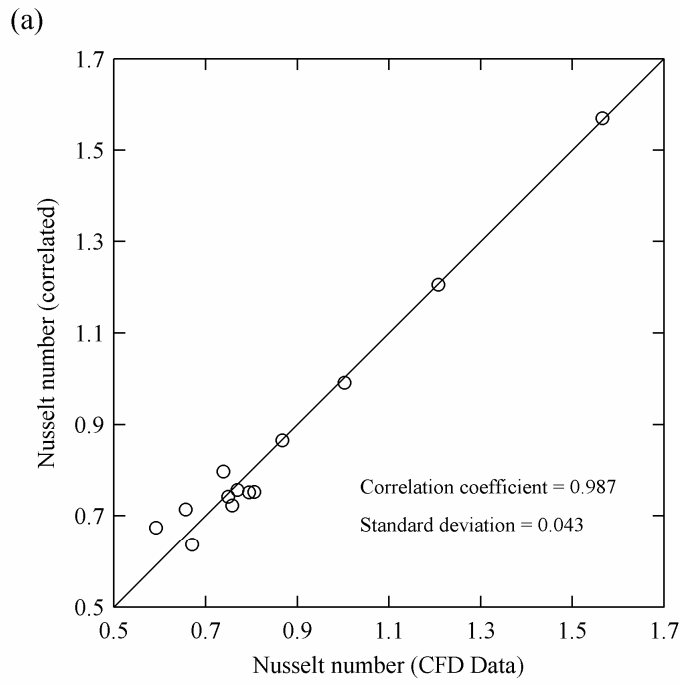


Figure 3.1: Parity plots of Nusselt number for natural convective heat transfer: (a) at the absorber; (b) at the aperture.

In case of ZnO-decomposition simulations, the reactant ZnO(s) enters the reactor at $T_{\text{sur}} = 300$ K and is heated to the reactor temperature at $T_{\text{a,in}}$:

$$q_{\text{reactants}} = \frac{\dot{n}_{0,\text{ZnO}} \Delta H \Big|_{\text{ZnO at } T_{\text{sur}} \rightarrow \text{ZnO at } T_{\text{a,in}}}}{2\pi r_{\text{a,in}} l} \quad (3.21)$$

The reaction extent $X_{\text{ZnO}} = 1 - \dot{n}_{\text{ZnO}} / \dot{n}_{0,\text{ZnO}}$ is determined at the reactor temperature based on the Arrhenius-type decomposition rate law [49],

$$\dot{r} = 1.356 \times 10^9 \exp(-328500 / R_u T) \text{ g m}^{-2} \text{ s}^{-1} \quad (3.22)$$

assuming a reaction zone length of $l = 15$ cm, an initial particle diameter of 7×10^{-6} m, and an argon carrier gas flow rate of $1 \text{ l}_n/\text{min}^3$. The power absorbed by the chemical reaction is then:

$$q_{\text{chemistry}} = \frac{\dot{n}_{\text{Zn}} \Delta H \Big|_{\text{ZnO at } T_{\text{a,in}} \rightarrow \text{Zn(g)}+0.5\text{O}_2 \text{ at } T_{\text{a,in}}}}{2\pi r_{\text{a,in}} l} \quad (3.23)$$

where $\dot{n}_{\text{Zn}} = X_{\text{ZnO}} \dot{n}_{0,\text{ZnO}}$ is the molar flow rate of ZnO decomposed. The power used to heat the Ar carrier gas is:

$$q_{\text{gas}} = \left(\dot{n}_{\text{Ar}} \int_{T_{\text{sur}}}^{T_{\text{a,in}}} c_{\text{p,Ar}}(T) dT \right) / 2\pi r_{\text{a,in}} l \quad (3.24)$$

Under pure Ar flow, the Nusselt number for internal flow in a circular tube $Nu_{d_{\text{a,in}}} = hd_{\text{a,in}} / k_{\text{Ar}} = 4.36$ [40] can be used. The temperature-dependent thermal conductivity of Ar k_{Ar} is taken from Ref. [50].

In biochar gasification simulations, the reactants steam and charcoal and the carrier gas enter the reactor at 473 K and are heated to the reactor temperature $T_{\text{a,in}}$. Thus,

$$q_{\text{reactants}} = \left(\dot{n}_{\text{H}_2\text{O}} \int_{473 \text{ K}}^{T_{\text{a,in}}} c_{\text{p,H}_2\text{O(g)}}(T) dT + \dot{n}_{\text{coal}} \int_{473 \text{ K}}^{T_{\text{a,in}}} c_{\text{p,coal}}(T) dT \right) / 2\pi r_{\text{a,in}} l \quad (3.25)$$

and

$$q_{\text{gas}} = \left(\dot{n}_{\text{Ar}} \int_{473 \text{ K}}^{T_{\text{a,in}}} c_{\text{p,Ar}}(T) dT \right) / 2\pi r_{\text{a,in}} l \quad (3.26)$$

with heat capacities c_p taken from Ref. [51]. The power absorbed by the gasification reaction is:

$$q_{\text{chemistry}} = \frac{X_C \cdot \dot{n}_{0,\text{C}} \cdot \Delta H_{\text{R}} \Big|_{T_{\text{a,in}}}}{2\pi r_{\text{a,in}} l} \quad (3.27)$$

³ l_n means litres under standard conditions at 273.15 K and 1 atm.

where $\dot{n}_{0,C}$ denotes the molar rate of carbon fed to the reactor. The rate law of the shrinking spherical particle model with an unreacted spherical core [52] is applied for the carbon conversion $X_C = 1 - \dot{n}_C / \dot{n}_{0,C}$:

$$\frac{dX_C}{dt} = k'(1 - X_C)^{2/3} \quad (3.28)$$

which was determined experimentally [53] (see section 5.2).

Heat transfer to the reaction zone occurs via combined radiation, conduction, and convection modes. Representative relaxation times are compared for assessing the relative importance of these different modes. The reference time scale for the fluid flow, $\tau_{\text{flow}} = L/u$, equals 0.006 s, with $L = 1$ cm as the characteristic length. Values are calculated for the continuous-mode biochar gasification. For convective heat transfer, the relaxation time of the temperature of a spherical particle submerged in a fluid at a different temperature [40], $\tau_{\text{convection}} = \rho_{\text{solid}} c_{p,\text{solid}} d_p^2 / (12k_g)$, is 10^2 times shorter to τ_{flow} . For radiative heat transfer, the relaxation time of the particle temperature with surroundings at T_∞ , $\tau_{\text{radiation}} = \rho_{\text{solid}} c_{p,\text{solid}} d_p / (24\sigma\epsilon T_\infty^3)$, is 10 times shorter than τ_{flow} . For simplicity, the reaction zone temperature is assumed to be constant at $T_{a,\text{in}}$. Its exact determination would require an extension to a 3D-model. Further simplification is introduced by assuming particles and gas flows being at the same temperature, justified by the high rate of convective/radiative heat transfer for μm -sized particles as indicated by the time scales $\tau_{\text{convection}}$ and $\tau_{\text{radiation}}$. Transient heat transfer within a two-phase solid-gas flow has been examined for solar reactors with particles directly exposed to concentrated solar radiation [54-55]. These previous studies revealed that the difference between the particle and gas temperatures at steady state is insignificant and reached a maximum of 50 K for μm -sized particles, as heat transfer between the solid and gas phases was predominantly by convection and by gas IR emission.

The reaction zone of length $l = 15$ cm is divided into finite elements of length $\Delta l = 10^{-4}$ m. The increase in carbon conversion ΔX_C as the reactants flow through a section of length Δl is then determined with Eq. (3.28) at $T_{a,\text{in}}$, with the residence time Δt calculated from the total volumetric flow, including both reactant and product gases. Since temperatures are not known a priori, the system of equations is solved iteratively with the Gauss-Seidel method using the convergence criterion $|1 - T_{i,j}^{f-1} / T_{i,j}^f| \leq 10^{-3}$ for every single node (i, j) and iteration step f .

4 Solar thermal ZnO dissociation⁴

4.1 Introduction

In this chapter the first step of the water-splitting cycle, the thermal dissociation of ZnO(s) into its elements, is considered. This reaction proceeds endothermically ($\Delta H_{298\text{K}}^{\circ} = 350$ kJ/mol) at above 1800 K [5,9,12]. Various exploratory tests were carried out in solar furnaces [11,21-23,56]. Perkins et al. [57] obtained net conversions in the range 6–17% in an electrically heated transport tube apparatus for aerosol ZnO dissociation. Recently, Schunk et al. [25] achieved a maximum Zn content in particles collected downstream of the reactor on a filter of 41.7 mol %. The reactor, featuring a rotating cavity receiver where ZnO is directly exposed to concentrated solar radiation, was operated in transient ablation mode with semicontinuous feed cycles of ZnO particles. Experimental runs exceeded 4 h of operation. Efficient separation of the effluents at reactor exit is crucial for the efficiency of the process. This can be achieved by a fast quench [58], either by adiabatic expansion in a Laval nozzle [59-60] or by injection of a cold gas stream [61-62]. Zn yields exceeding 90% were obtained in preliminary runs with a quench apparatus in a solar thermogravimeter reactor [62]. An annular argon flow suppressed diffusion to the outlet tube walls, while injection of a single Ar jet orthogonal to the pipe axis led to cooling rates of up to 1.2×10^5 K/s. As an alternative to a quench device, which is sensitive to the dilution ratio of Zn(g) in the gas flow, electrothermal methods can be used for in-situ separation of Zn(g) and O₂ at high temperatures [63]. Recent studies of the decomposition reaction kinetics include thermogravimetric (TG) analysis [64-65], investigation in a solar-driven thermogravimeter with a packed-bed of ZnO particles [66] and experimentation in a solar furnace with solid blocks of ZnO [49]. Reported activation energies are in the range 310–360 kJ/mol.

In the present study, ZnO decomposition experiments were performed in batch-mode and continuous-mode process in the indirectly irradiated solar reactor described in section 2.2. Validation of the reactor model presented in chapter 3 is accomplished for a continuous flow of Ar (without ZnO-feeding) and for the batch chemical process to examine the capability of this receiver-reactor concept to transfer solar process heat to a working fluid flow and to solid

⁴ Material from this chapter has been published in: T. Melchior, C. Perkins, A.W. Weimer and A. Steinfeld. A cavity-receiver containing a tubular absorber for high-temperature thermochemical processing using concentrated solar energy. *International Journal of Thermal Sciences* **47** (11): 1496-1503 (2008).

reactants at high temperatures. Practical problems associated with construction materials exposed to high-flux irradiation and temperatures exceeding 1900 K are discussed.

4.2 Experimental setup

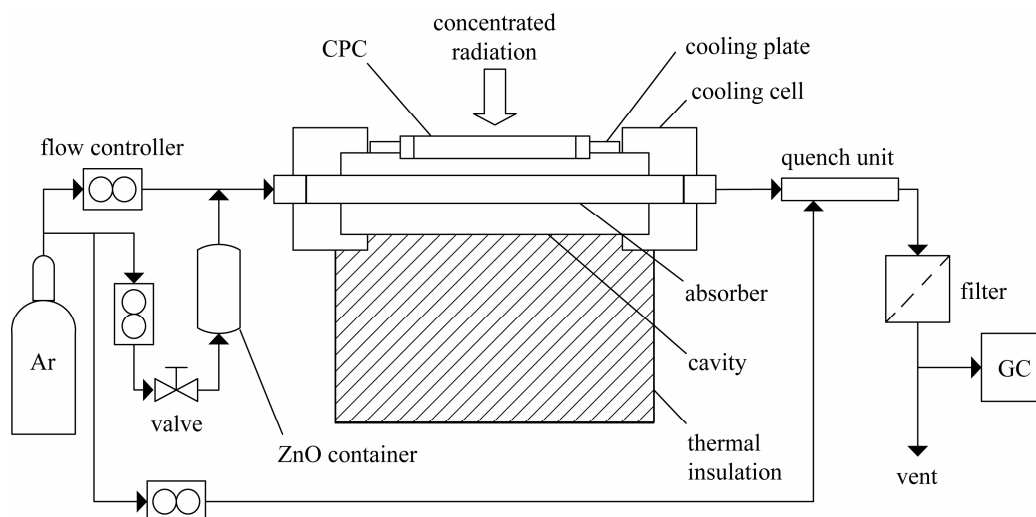


Figure 4.1: Scheme of the experimental setup of the solar reactor and peripheral components.

Figure 4.1 shows schematically the experimental setup of the reactor prototype with peripherals. All experiments were conducted using the Al_2O_3 absorber. During a typical experimental run, the absorber was heated to the desired temperature, maintained isothermally for 10 min, and cooled to ambient temperature. The heating rate was relatively slow, about 40 K/min, since preliminary runs have shown that ceramic casting components, such as the Al_2O_3 tube, poorly withstand severe thermal shocks. This is in contrast to direct-absorption reactor concepts, where the reactants are directly exposed to high-flux solar irradiation and can be heated at rates exceeding 1000 K/s [21]. In continuous-mode experiments, ZnO particles (Sigma-Aldrich 255750, purity 99.99%) were fed into the main Ar stream after the desired temperature was reached by short pulses of a second Ar stream, which was injected into the ZnO container by a manually operated valve. The amount of ZnO fed to the reactor was determined from the weight difference of the ZnO tank before and after experiments. In batch-mode experiments, pre-sintered ZnO plates with an average surface area per unit length of $A_{\text{ZnO}} = 0.0446 \text{ m}^2/\text{m}$ were placed inside the absorber tube. The ZnO container and the second Ar pipe were removed from the setup. The products were carried by Ar flow to a quench unit incorporated at the reactor exit. Quenching is accomplished by a so-called “fluid-wall” concept [67]. The quench unit consists of two concentric tubes, with the outer one being

water-cooled and the inner one having a porous wall for the injection of an inert gas. The effluents from the reactor are flowed through the inner region of the porous tube, while the cold inert gas is forced radially through it and into the main flow channel. This method has been used in solar methane dissociation to prevent carbon particle deposition on tube walls [68], and was studied in CFD simulations for preventing oxidation in solar-thermal ZnO reactors [67]. Inlet mass flow rates were controlled by electronic flow controllers (Bronkhorst HI-TEC). The off-gas was analyzed on-line by gas chromatography (two-channel Varian Micro GC, equipped with Molsieve-5A and Poraplot-U columns). Phase composition of solids collected from absorber, quench unit and filter was measured by X-ray diffraction (XRD). Temperatures were measured with type-B and type-K thermocouples at four locations indicated in Fig. 2.1: at the outer surface of the absorber ($T_{a,out}$), at 3 mm behind the inner cavity surface ($T_{c,3mm}$), at the center of the absorber ($T_{a,center}$), and at the outer cavity surface ($T_{c,out}$). The thermocouple measuring $T_{a,out}$ was shielded from radiation by a thin open-ended alumina tube. Its tip was attached to the absorber surface with zirconia cement. Thermocouples were installed at the middle of the tube length.

4.3 Numerical results and experimental validation

Validation of the reactor model in terms of measured temperatures was performed for continuous-mode experiments using an Ar flow but without chemical reaction ($q_{chemistry} = 0$). Validation of the kinetic rate law (Eq. (3.22)), taken from Ref. [49], in terms of the measured reaction rates was performed for batch-mode experiments using a pre-fed batch of ZnO. Power levels are given per unit length of reactor as defined for the 2D-simulations.

A set of 7 representative runs using an Ar mass flow rate of 1 l_n/min and without chemical reaction were carried out for the continuous-mode experimental validation of the model. Figure 4.2 shows the numerically calculated (curves) and experimentally measured (markers) temperatures at the inner absorber surface $T_{a,in}$, the inner cavity surface $T_{c,in}$, the outer cavity surface $T_{c,out}$, and 3 mm behind the inner cavity surface $T_{c,3mm}$, as a function of the incoming solar power per unit length Q'_{solar} in the range from 5.4 kW/m to 28.3 kW/m. Not shown are the calculated and measured temperatures on the outer absorber surface as they practically coincide with the inner absorber temperature, with the largest temperature difference $T_{a,out} - T_{a,in} = 12$ K for $Q'_{solar} = 28.3$ kW/m. The experimental values of the inner absorber surface temperature $T_{a,in}$ were derived from the temperatures measured at the center

of the absorber $T_{a,center}$ using the radiosity method (see appendix). As expected, all temperatures increased with the power input. The maximum $T_{a,in}$ was 2490 K, which exceeded Al_2O_3 m.p. (local melting was observed), while $T_{c,in}$ was about 500 K lower and $T_{c,out}$ never exceeded 1000 K. The maximum temperature difference between inner and outer cavity wall was about 1120 K, which lead to the formation of local cracks in the YO_2 -stabilized ZrO_2 . The mean relative difference between measured and calculated values was 4.61% with a standard deviation $\pm 4.87\%$, due mainly to discrepancies between real material properties and those extracted from literature for the model.

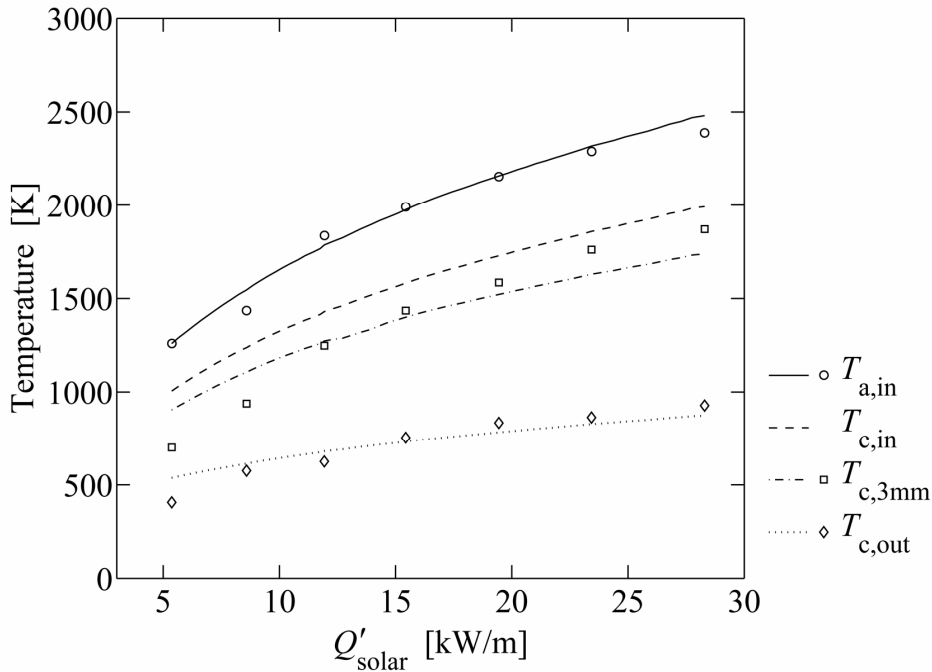


Figure 4.2: Numerically calculated (curves) and experimentally measured (markers) temperatures at the inner absorber surface $T_{a,in}$, the inner cavity surface $T_{c,in}$, the outer cavity surface $T_{c,out}$, and 3 mm behind the inner cavity surface $T_{c,3mm}$, as a function of the incoming solar power per unit length Q'_{solar} .

Six experimental runs were carried out in batch-mode between 1780 and 1975 K. The average reaction rate was determined using the weight loss during experiment of the ZnO plate positioned inside the absorber. No reaction was observed at below 1750 K. The reaction rates obtained from these experiments are shown in Fig. 4.3, along with the theoretically calculated rates (curve) used the kinetic rate law of Eq. (3.22). Error bars result from the inaccuracies in the measurement devices (balance ± 0.0015 g, dimensions ± 0.05 mm, temperature $\pm 2\%$ of the reading). An 8-fold increase in the reaction rate was obtained in the range considered, with a peak rate of $2.446 \text{ g m}^{-2} \text{ s}^{-1}$ at 1975 K. Note that in these experimental runs, Zn(g) and O_2 exiting the reactor underwent recombination, as indicated by

gas chromatography of the gaseous products and X-ray diffraction of the solid products. The mass balance showed that 69% to 99% of the dissociated ZnO was recovered at the exit of the absorber tube just before the quench unit. The inner absorber surface was covered by ZnO needles. On the filter, 1% to 5% of the recombined ZnO were collected. The remaining products are assumed to have deposited in the connection tubes and quench unit.

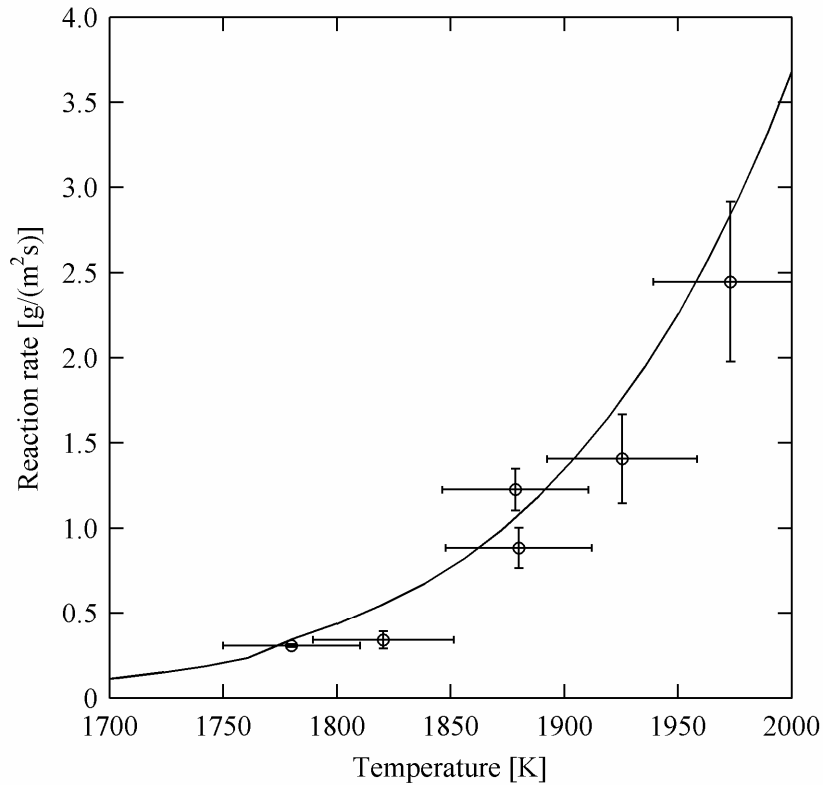


Figure 4.3: Experimentally measured (markers) and theoretically calculated (curve) ZnO decomposition rates.

4.4 Numerical simulation of the continuous chemical process

Numerical simulations of the reactor were performed with continuous feeding of reactants ($\dot{n}_{0,\text{ZnO}} = 3.07 \times 10^{-3}$ mol/s) and removal of products. Calculated temperature variations as a function of Q'_{solar} in the range 5.4 – 40.0 kW/m (equivalent to a mean radiative flux at the CPC exit in the range 382 – 2830 kW/m²) are plotted in Fig. 4.4 for steady-state conditions. Overall, temperatures are lower than those obtained without chemistry (Fig. 4.2) due to the additional heat sink resulting from heating the reactants ($Q_{\text{reactants}}$) and from the endothermic chemical reaction ($Q_{\text{chemistry}}$), as observed especially at above 1800 K for higher reaction

extents X_{ZnO} (see also Fig. 4.5). For $Q'_{\text{solar}} = 28.3 \text{ kW/m}$, $T_{\text{a,in}}$ reaches 2120 K, about 370 K lower than in the case without chemistry. For $Q'_{\text{solar}} = 40.0 \text{ kW/m}$, $T_{\text{a,out}} = 2400 \text{ K}$, $T_{\text{a,in}} = 2300 \text{ K}$, $T_{\text{c,in}} = 1970 \text{ K}$, and $T_{\text{c,out}} = 860 \text{ K}$, and near reaction completion is obtained (see also Fig. 4.5).

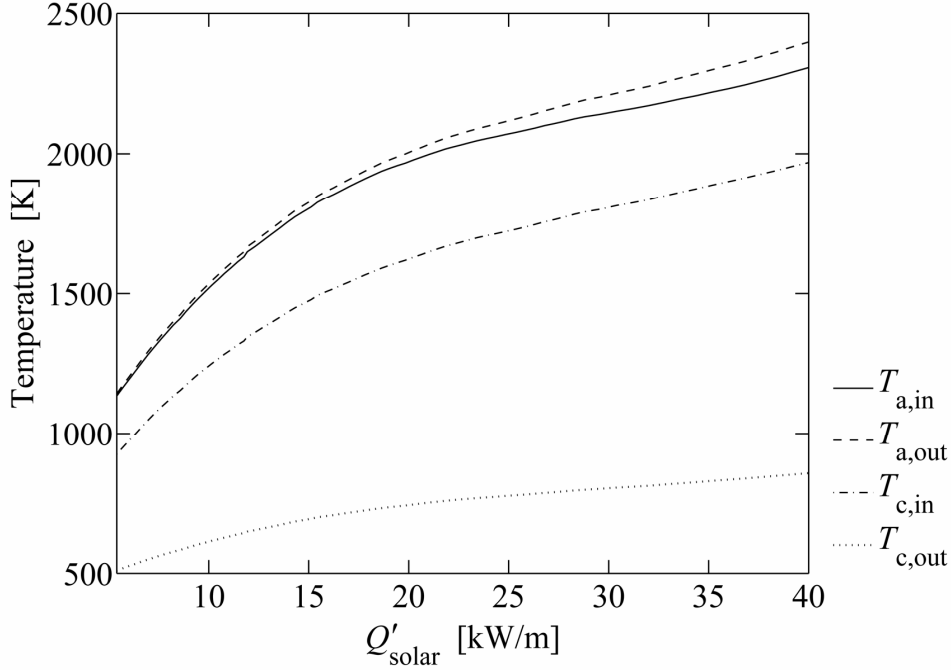


Figure 4.4: Numerically calculated steady-state temperatures of the inner/outer absorber ($T_{\text{a,in}}$ and $T_{\text{a,out}}$) and inner/outer cavity surfaces ($T_{\text{c,in}}$ and $T_{\text{c,out}}$) as a function of the input solar power per unit length Q'_{solar} .

The solar-to-chemical energy conversion efficiency η is defined as the portion of the input solar power absorbed by the chemical reactants, both in the form of sensible heat and chemical process heat,

$$\eta = \frac{X_{\text{ZnO}} \cdot Q_{\text{reactants}} + Q_{\text{chemistry}}}{Q_{\text{solar}}} \quad (4.1)$$

Figure 4.5 shows η and X_{ZnO} as a function of the inner absorber surface temperature, assuming no recombination of the products exiting the solar reactor. At $T_{\text{a,in}} = 2300 \text{ K}$, X_{ZnO} approaches nearly completion, resulting in a maximum η of 28.5%. This predicted maximum efficiency is significantly higher than the one reported for the direct-absorption reactor operated at 2000 K and a solar power input of 9.1 kW, yielding a decomposition rate of 12 g/min, but an increase of the temperature to 2300 K could significantly augment the kinetics and, consequently, boost its efficiency [24].

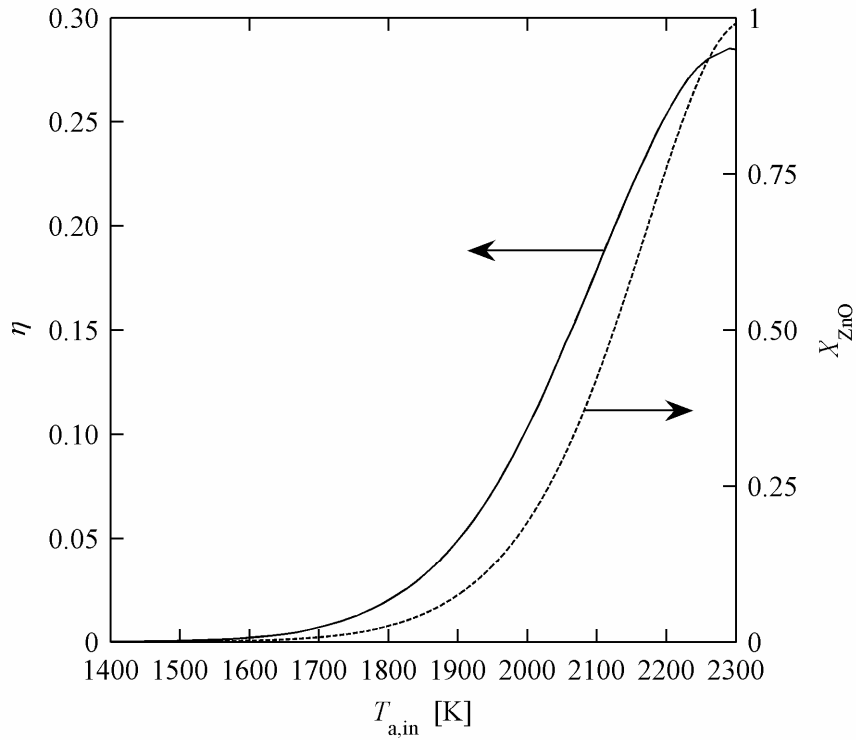


Figure 4.5: Solar-to-chemical energy conversion efficiency and chemical reaction extent as a function of the inner absorber surface temperature.

Finally, Fig. 4.6 shows the overall energy balance calculated for $Q'_{\text{solar}} = 16, 28, \text{ and } 40$ kW/m. The power is indicated in percent of the solar power input. Re-radiation and conduction losses are predominant, with the latter decreasing from 36% to 24% over the power range considered. For $Q'_{\text{solar}} = 16$ kW/m, $Q_{\text{chemistry}} = 0.027Q_{\text{solar}}$ because of the relatively low reactor temperatures and, consequently, poor chemical conversion. Obviously, increasing Q'_{solar} leads to higher temperatures and thereby higher conversions, but at the expense of higher re-radiation losses. The energy fraction consumed by chemistry peaks at 22.5% for $Q'_{\text{solar}} = 36.8$ kW/m (not shown in the graph), corresponding to a reactor temperature of 2245 K (ZnO melting point). Further temperature increase implies a decrease of the reaction enthalpy from 450 to 380 kJ/mol. For $Q'_{\text{solar}} = 40$ kW/m, the reactor temperature reaches 2300 K and $\eta = 28.5\%$. $Q_{\text{chemistry}}$ and $Q_{\text{reactants}}$ represent 19.3 and 9.2% of Q_{solar} , respectively.

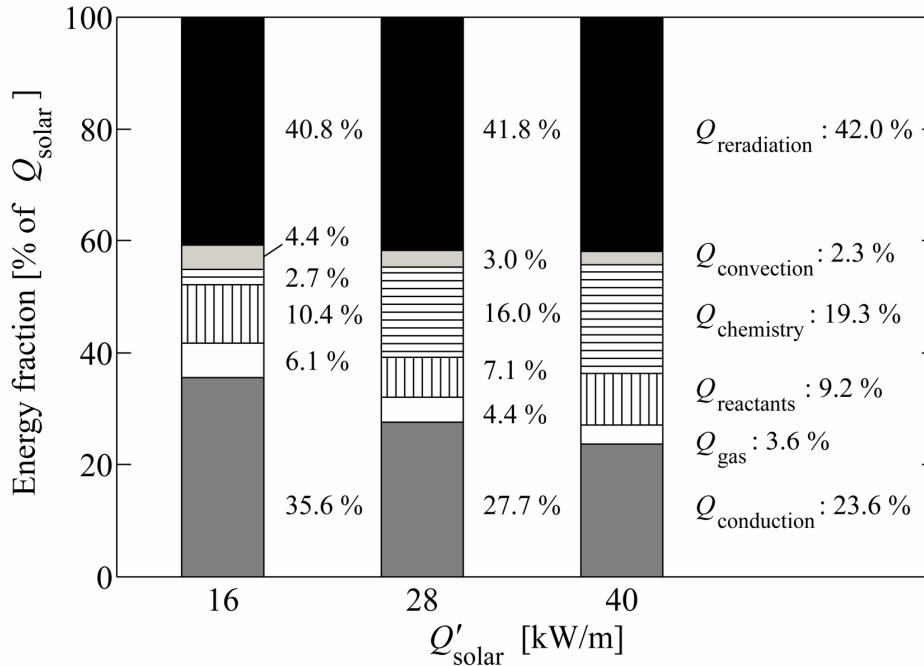


Figure 4.6: Energy balance at input solar power levels of 16, 28 and 40 kW/m (per unit length of reactor), obtained by continuous-mode thermochemical process simulation.

4.5 Continuous chemical process experiments

Fifteen experimental runs were carried out at absorber temperatures in the range 1873–2023 K. Gas flow rates ranged from 1 to 4 l_n/min for carrier gas, and 0 to 4 l_n/min for quench gas. O₂ formation was not detected by online gas analysis during experiments. Particles collected from the filter downstream of the reactor consisted of pure ZnO, as revealed by XRD analysis. Figure 4.7 shows the particle number density distribution curves of feedstock particles fed to the reactor (solid line) and product particles collected on the filter (dashed line), as measured by laser scattering (HORIBA LA-950). As both curves practically coincide, it can be assumed that ZnO decomposition did not occur. A mean particle diameter of 0.15 μm was found for the two probes. Further evidence is given by scanning electron microscopy (SEM, Zeiss Gemini Supra 55 VP) pictures of feedstock and product particles shown in Fig. 4.8. Identical morphologies are found for fed and filtered particles, reinforcing the assumption of inexistent chemical reaction. This is in contradiction with numerical simulation results from section 4.4. However, it should be noted that uniform gas and particle temperature was assumed in the 2D-model. Reaction kinetics are fast enough for the reaction to proceed. In experiments, however, heat transfer was probably inefficient at the prevailing conditions where residence times were below 0.4 s in the reactor with relatively small

dimensions. For comparison, net conversions of up to 18% were found in an aerosol down flow reactor consisting of an electrical resistance furnace that contains an alumina tube with a diameter of 9.0275 cm and a reaction zone length of 45.72 cm [57]. Note that these dimensions would exceed lab-scale solar reactor limits with regard to operation in the HFSS. Further operational problems were related to the ZnO(s) feeding system, which needs to be improved. Less than 10% of the fed material was found in the filter downstream of the reactor. The major part had deposited in connection tubes leading to the reactor entrance, mainly in the T-junction between reactor, ZnO tank and main gas pipeline.

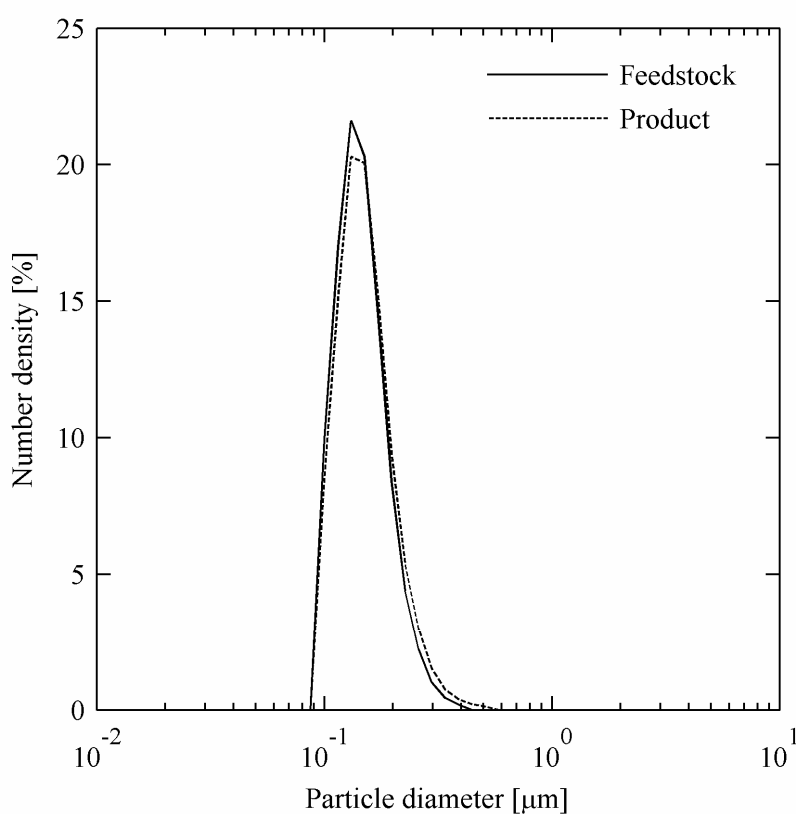


Figure 4.7: Number density distribution of feedstock particles (solid line) and particles collected in the filter (dashed line).

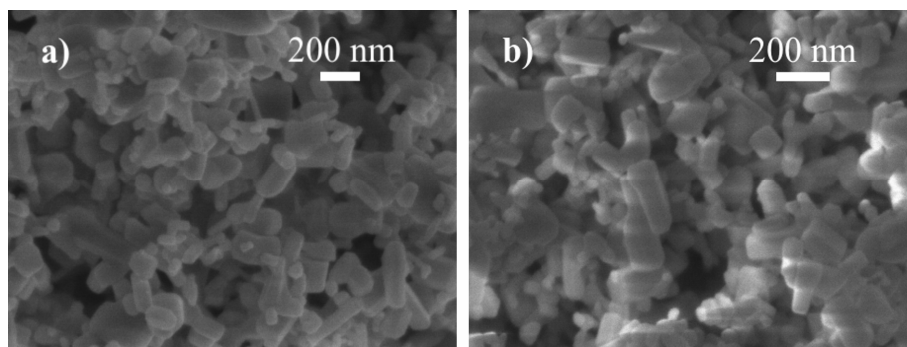


Figure 4.8: SEM pictures of (a) feedstock particles and (b) particles collected in the filter.

4.6 Summary and conclusions

A cylindrical cavity-receiver containing a tubular absorber for effecting high-temperature thermochemical reactions using concentrated solar energy was designed, fabricated and tested. The reactor was modeled using a 2D steady-state formulation coupling radiation, conduction, and convection heat transfer to the chemical kinetics, and solved using Monte-Carlo and finite difference techniques. The numerically computed temperatures and ZnO decomposition rates were in reasonable good agreement with the experimentally measured values obtained from tests performed in a high-flux solar simulator. Reaction rates were measured in batch-mode experiments. Major heat losses were re-radiation through the aperture and conduction through the reactor walls. Simulation of a continuous flow process for ZnO dissociation predicts nearly completion of the reaction extent and maximum solar-to-chemical energy conversion efficiency of 28.5% at a reactor temperature of 2300 K for an input solar power per unit length of absorber of 40 kW/m. However, continuous chemical process experiments proved unsuccessful. Experimental validation of a continuous process will therefore be carried out in the following chapter, with steam-gasification of biochar selected as the model thermochemical process.

5 Model validation – Solar-driven biochar gasification⁵

5.1 Introduction

In this chapter, the numerical model described in chapter 3 is validated with the biochar gasification process. Solar steam-gasification of biomass makes use of concentrated solar energy to convert solid biomass feedstocks into high-quality synthesis gas (syngas) – mainly H₂ and CO – applicable for power generation in efficient combined cycles and fuel cells, or for Fischer-Tropsch processing of liquid biofuels [5,69]. Conventional autothermal gasification requires a significant portion of the introduced feedstock to be combusted with pure O₂ - usually produced by the energy-intensive air separation - to supply high-temperature process heat for the highly endothermic gasification reaction. For example, the energy required to gasify bituminous coal of LHV 34 MJ/kg is supplied by burning 35 % of the injected coal mass [53]. In contrast, the solar-driven gasification eliminates the need for a pure stream of oxygen. Consequently, the gaseous products are not contaminated by the byproducts of feedstock combustion. Furthermore, the calorific value of the biomass feedstock is solar-upgraded by an amount equal to the enthalpy change of the reaction, resulting in syngas with a negative CO₂ intensity. Ultimately, solar thermochemical gasification of carbonaceous feedstocks is a means of chemically storing intermittent solar energy in a dispatchable form. Solar pyrolysis and gasification of coke, coal, cellulose, and other carbonaceous materials was studied in directly irradiated fluidized-bed [70-71], vortex-flow [72-73], molten-salt pool [74], and packed-bed [53] solar reactors. Further, numerous studies have investigated the pyrolysis and gasification of biomass-derived char in non-solar reactors, e.g. in thermogravimeters [75-77], or fixed-bed microreactors [78-79].

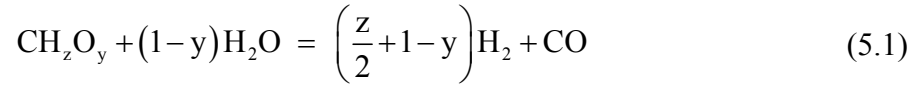
In the present work, the steam-gasification of biochar is performed using the aforementioned reactor concept (section 2.2). Particles of beech charcoal are used as the biomass feedstock in a continuous steam-particle flow through the tubular absorber. The chemical thermodynamics and reaction kinetics are analyzed. The previously formulated heat transfer model (chapter 3) is applied to couple radiation/convection/conduction heat transfer to the reaction kinetics and validated by comparing numerically computed and experimentally measured temperatures and reaction rates. This model is further employed to examine the

⁵ Material from this chapter has been submitted for publication: T. Melchior, C. Perkins, P. Lichty, A.W. Weimer and A. Steinfeld. Solar-driven biochar gasification in a particle-flow reactor. *Chemical Engineering and Processing* **48** (8): 1279-1287 (2009).

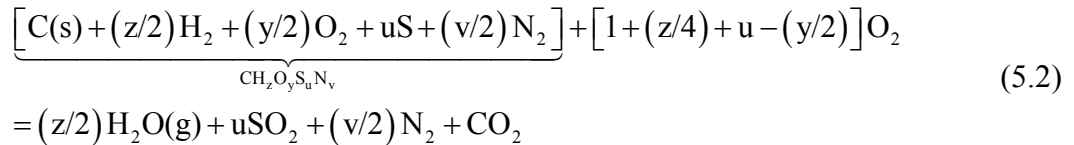
thermal performance of a scaled-up reactor for 100 kW and 1 MW solar radiative power input.

5.2 Thermodynamics and kinetics analyses

The overall process can be represented by the simplified net reaction:



where z and y are the elemental molar ratios of H/C and O/C in charcoal, respectively. Sulfur/nitrogen containing compounds and other impurities have been omitted from Eq. (5.1). The thermodynamic equilibrium composition of a system composed of a stoichiometric mixture of beech charcoal and water, $\text{C}_1\text{H}_{0.418}\text{O}_{0.117}\text{S}_{0.0003}\text{N}_{0.006} + 0.883 \text{H}_2\text{O}$, at 1 bar and over a wide temperature range of interest is shown in Fig. 5.1. The HSC Outokumpu code [80] was used; species whose mole fraction is less than 10^{-3} (e.g., HCN or H_2S) have been omitted from the figure. At above 1400 K, the system at equilibrium consists of a gaseous mixture of 52 % H_2 and 48 % CO. Also indicated in Fig. 5.1 is the enthalpy change of the reaction as a function of temperature, when the reactants are fed at ambient temperature and the products are obtained in equilibrium at the reaction temperature. At 1400 K, $\Delta H = 179.9 \text{ kJ/mol C}$. Note that since charcoal has no reference enthalpy, all enthalpy changes were calculated by assigning to charcoal the reference enthalpy of its elemental composition $[\text{C}(\text{s}) + (z/2)\text{H}_2 + (y/2)\text{O}_2 + u\text{S} + (v/2)\text{N}_2]$ at 300 K (u and v are the elemental molar ratios of S/C and N/C in charcoal, respectively), and further adjusting for the small offset between the heating value of charcoal (437.9 kJ/mol C, calculated from elemental composition [81](Netz, 1982)) and the enthalpy change of the combustion reaction at 300 K given by:



The reaction rate was determined by thermogravimetry [53]. Applying the shrinking spherical particle model for an unreacted spherical core [52], the rate law is expressed with Eq. (3.28):

$$\frac{dX_c}{dt} = k'(1 - X_c)^{2/3}, \text{ where } X_c = 1 - \dot{n}_c / \dot{n}_{0,c} \text{ denotes the carbon conversion and } k' \text{ denotes}$$

the rate constant assumed to obey the Arrhenius law, $k' = k_0 \exp(-E_a/R_u T)$, with an

apparent activation energy $E_a = 43154 \text{ J/mol}$ and a pre-exponential factor $k_0 = 124.6 \text{ s}^{-1}$, the latter being adjusted for the experimental validation of the reactor model.

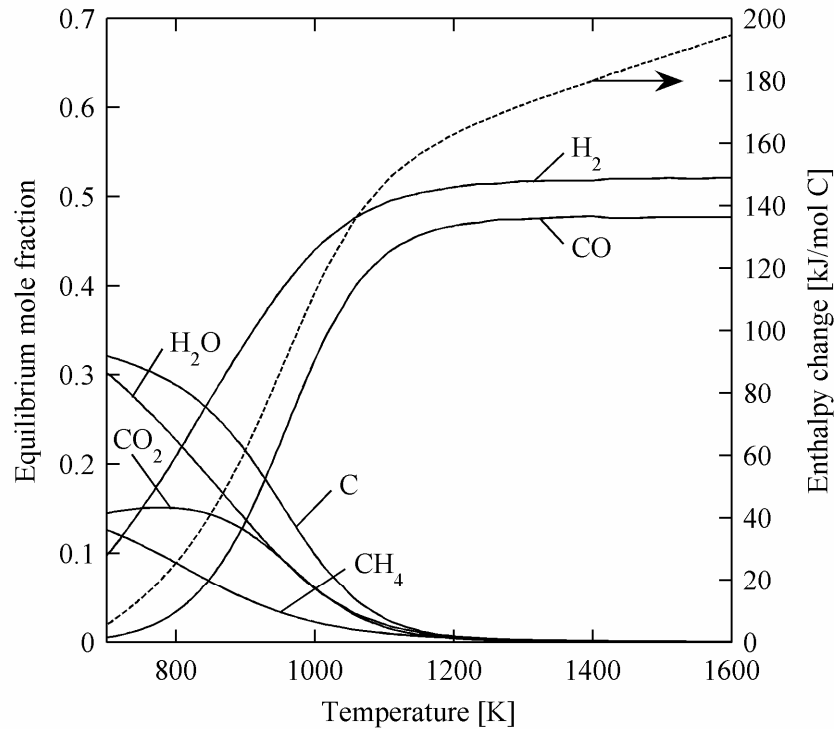


Figure 5.1: Equilibrium composition of the system $\text{C}_1\text{H}_{0.418}\text{O}_{0.117}\text{S}_{0.0003}\text{N}_{0.006} + 0.883 \text{ H}_2\text{O}$ as a function of temperature. Product species with mole fractions less than 10^{-3} have been omitted. Also indicated is the enthalpy change of reaction (dashed line) when the reactants are fed at ambient temperature and the products are obtained in equilibrium at the reaction temperature.

5.3 Experimental setup

The experimental setup, encompassing the solar reactor and its peripheral components, is shown schematically in Fig. 5.2. All experiments were conducted with beech charcoal particles (Fluka 03866, ash content 5 %), of BET specific surface area $180 \text{ m}^2/\text{g}$, as determined by N_2 adsorption at 77 K (Micromeritics TriStar 3000). The particle size distribution functions, as measured by laser scattering (HORIBA LA-950), are shown in Fig. 5.3. Plotted are the number density and the respective volume density of the beech charcoal feedstock, which has a mean particle size of $7.2 \text{ }\mu\text{m}$. Elemental composition

($C_{1.418}H_{0.117}S_{0.0003}N_{0.006}$) was determined with Leco CHN-900 (C-, H-, N-detection), Leco RO-478 (O-detection) and Leco CHNS-932 (S-detection) instruments.

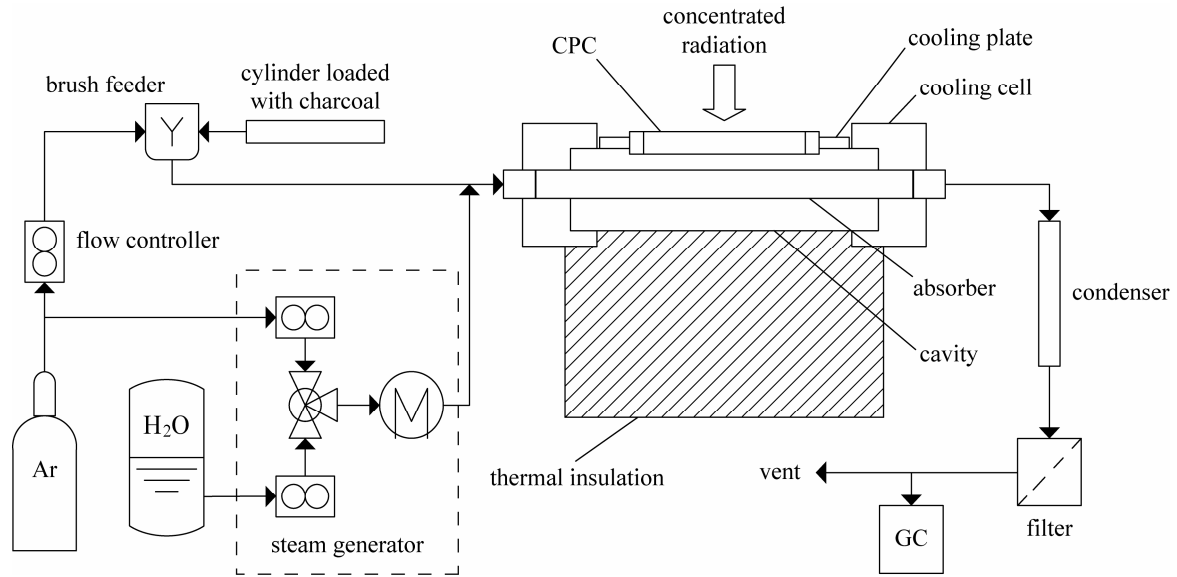


Figure 5.2: Scheme of the experimental setup of the solar reactor and peripheral components.

Charcoal particles were fed at a rate of 0.29–0.42 g/min by a piston and rotating brush into the conveying Ar stream, premixed with water vapor, and preheated to 473 K before entering the solar reactor. Inlet gas flows were controlled using electronic flow meters (Bronkhorst HI-TEC) and set to a steam mass flow rate of 0.79 g/min and Ar volumetric flow rate of 4.5 l_n/min, resulting in fluid velocities above the saltation velocity u_{salt} of 0.055 m/s, as calculated from [82]:

$$\frac{\dot{m}_{\text{charcoal}}}{\dot{m}_{\text{Ar}}} = \frac{1}{10^{1.44d_p+1.96}} \left[\frac{u_{\text{salt}}}{(g \cdot 2r_{a,\text{in}})^{1/2}} \right]^{1.1d_p+2.5} \quad (5.3)$$

where d_p is the particle diameter in mm. Product gases exiting the reactor were cooled to condense excess steam, and finally analyzed on-line by gas chromatography (two-channel Varian Micro GC, equipped with Molsieve-5A and Poraplot-U columns) before venting to the atmosphere. Non-reacted particles were collected downstream of the condenser with a glass-fiber filter (Whatman GF/A, 150-mm-dia.). Overall mass balances could not be established as condensed steam and non-reacted particles deposited in the condenser, filter and connecting tubes. Temperatures were measured with type-B and type-K thermocouples at three locations indicated in Fig. 2.1: at the outer surface of the absorber ($T_{a,\text{out}}$), at 3mm behind the inner cavity surface ($T_{c,3\text{mm}}$), and at the outer cavity surface ($T_{c,\text{out}}$). Thermocouples were located at

the middle of the tube length. The thermocouple measuring $T_{a,out}$ was shielded from radiation by a thin open-ended alumina tube while its tip was fixed onto the SiC-absorber surface with SiC-paste.

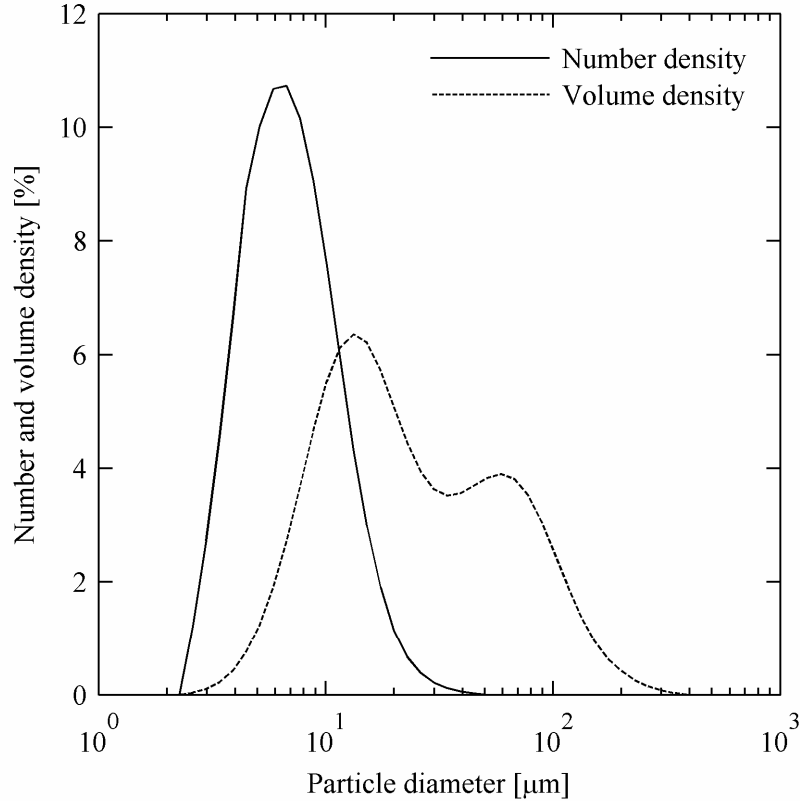


Figure 5.3: Particle size distribution function of the beech charcoal feedstock. Plotted are the number density (population density) and the volume density.

Concentrated radiative power input, absorber temperature, and product gas composition during a representative experimental run are shown in Fig. 5.4. The reactor was initially heated to the desired temperature under Ar flow by increasing stepwise the incoming radiative power Q_{solar} from the HFSS. The heating rate was relatively slow at about 40 K/min to avoid severe thermal shocks, in contrast to direct-irradiated reactors where heating rates exceeding 1000 K/s have been observed [54]. When the desired absorber temperature was reached, steam and charcoal feeding were switched on and the progress of the reaction was monitored by the on-line measurement of the product gas composition, consisting of mainly H_2 , CO , CO_2 and CH_4 . After steady-state in gas composition was attained for at least 6 minutes, Q_{solar} was increased to take the absorber temperature to the next level. The experiment was terminated by switching off the HFSS and the feeding of reactants.

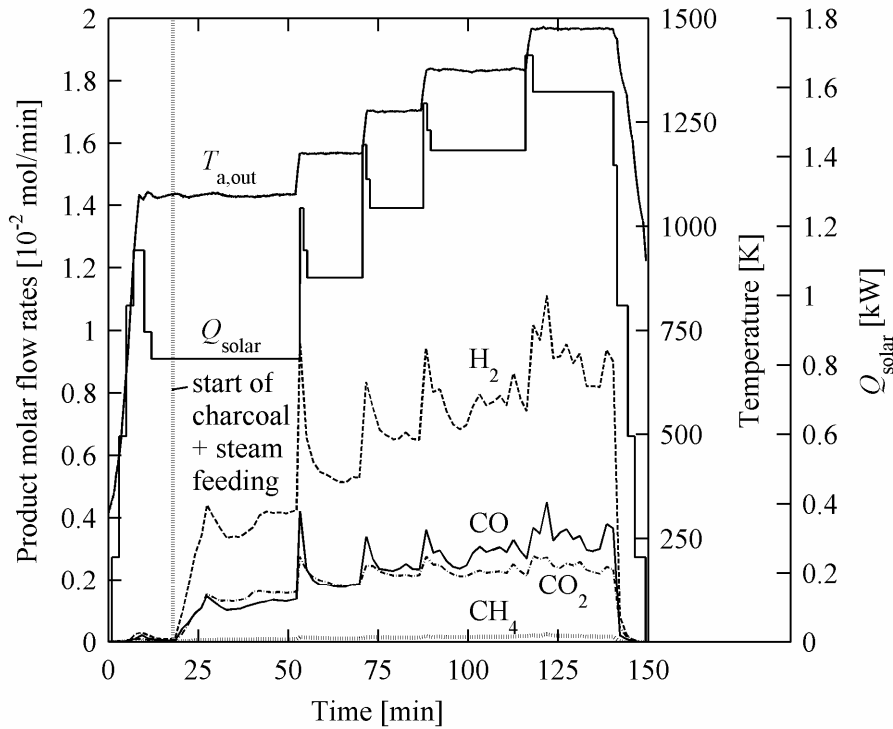


Figure 5.4: Power input, Q_{solar} , outer absorber temperature, $T_{\text{a,out}}$, and product gas composition during a representative experimental run with steam and charcoal feeding rates of 0.79 and 0.36 g/min, respectively.

5.4 Experimental validation of solar reactor model

A total of 19 experimental runs were carried out for the experimental validation of the reactor model (chapter 3). The radiative power input varied in the range 0.76 – 1.68 kW, resulting in absorber temperatures ranging from 1074 to 1523 K. Note that the maximum operation temperature to the SiSiC absorber tube is 1623 K [32]. Main product gases were H_2 , CO and CO_2 . Relatively smaller amounts of CH_4 were detected, which were most likely produced from pyrolysis reactions. The syngas composition can be adjusted to meet the requirements for their further processing, e.g Fischer-Tropsch synthesis, by methane reforming, water-gas shift reaction and/or CO_2 removal [83]. The measured (markers) and equilibrium (curves) molar ratios $\text{H}_2:\text{CO}$ and $\text{CO}_2:\text{CO}$, indicating the quality of the syngas, are shown in Fig. 5.5 as a function of $T_{\text{a,out}}$. The equilibrium values were calculated for the fed molar ratio $\text{H}_2\text{O}:\text{C} = 1.88$. The measured values, slightly decreasing over the considered temperature range, are

considerably higher than the equilibrium ratios, most likely due to the water-gas shift reaction occurring as the products cool at the exit of the reactor.

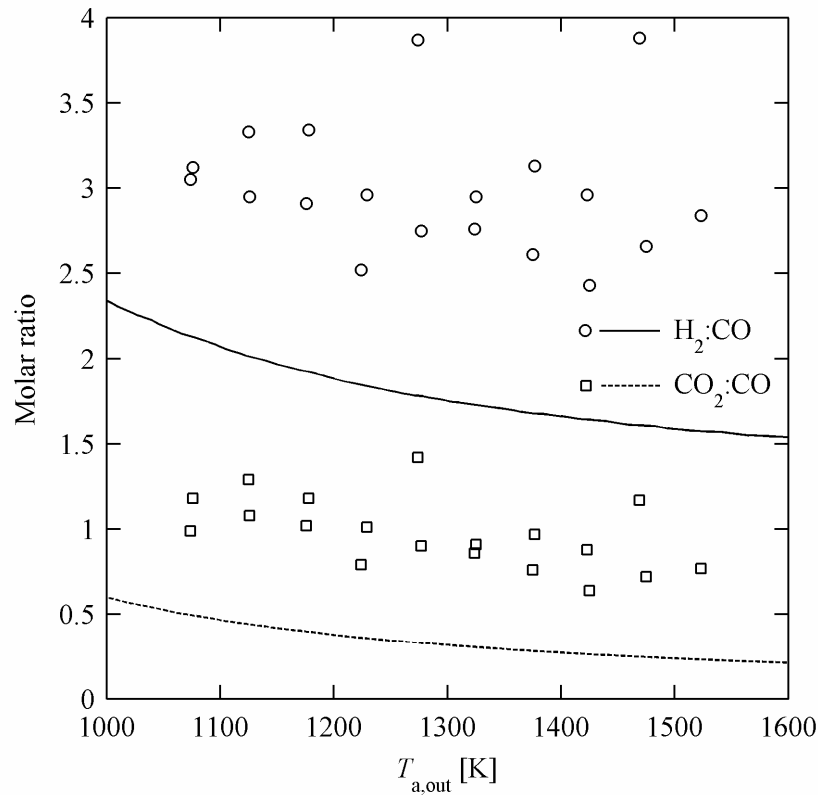


Figure 5.5: Measured (markers) and equilibrium (curves) molar ratios $H_2:CO$ and $CO_2:CO$.

In the numerical simulations, the charcoal feeding rate and the $H_2O:C$ molar ratio were set to the experimental average values: $\dot{m}_{charcoal} = 0.35$ g/min ($\dot{n}_{0,C} = 3.89 \times 10^{-4}$ mol/s), $H_2O:C = 1.88$. Figure 5.6 shows the numerically calculated (curves) and experimentally measured (markers) temperatures at the outer absorber surface $T_{a,out}$, the inner cavity surface $T_{c,in}$, the outer cavity surface $T_{c,out}$, and 3 mm behind the inner cavity surface $T_{c,3mm}$, as a function of the incoming power Q_{solar} . Not shown are the calculated temperatures on the inner absorber surface as they practically coincide with the outer absorber temperature, with the largest temperature difference $T_{a,out} - T_{a,in} = 3$ K for $Q_{solar} = 3$ kW. The absorber temperature increased from 969 to 1889 K over the considered power range, while $T_{c,in}$ was about 200 K lower and $T_{c,out}$ rised with a considerably lower slope from 502 to 896 K. In general, the agreement between calculated and measured temperatures is reasonably good. However, the model slightly overpredicts the absorber temperatures by 23 – 114 K, presumably because of

negligence of conduction losses in the axial direction and discrepancies between real material properties and those extracted from literature for the model. The mean relative difference is 4.2% with a standard deviation of $\pm 2.4\%$.

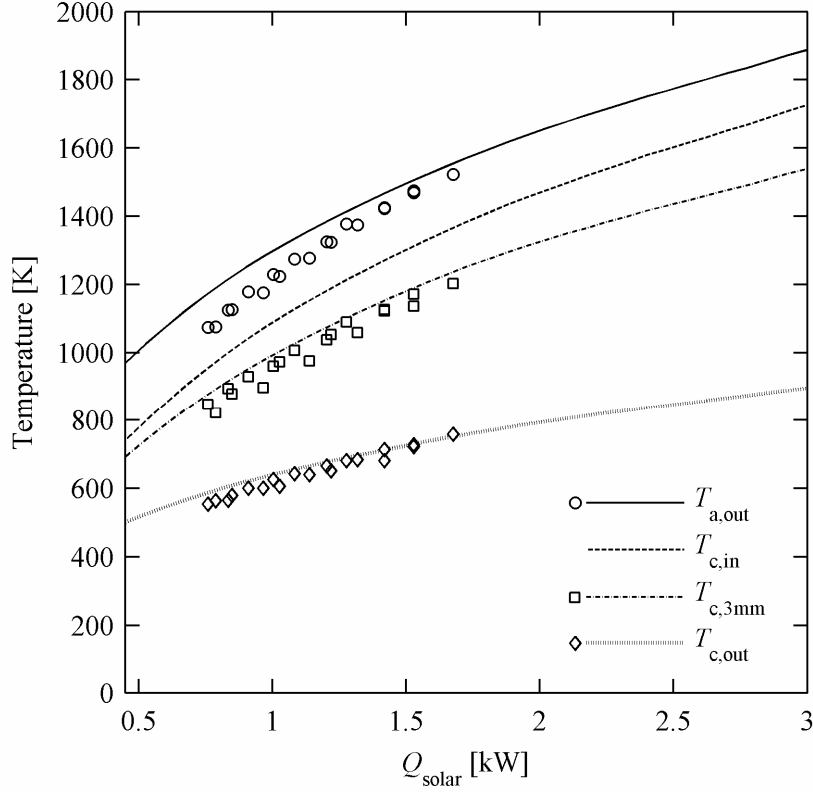


Figure 5.6: Numerically calculated (curves) and experimentally measured (markers) temperatures at the outer absorber surface, $T_{a,out}$, the inner cavity surface, $T_{c,in}$, the outer cavity surface, $T_{c,out}$, and 3 mm behind the inner cavity surface, $T_{c,3mm}$, as a function of the incoming power Q_{solar} .

Carbon conversions obtained from experiments (markers) and simulations (curve) are shown in Fig. 5.7 as a function of $T_{a,out}$. Error bars result from inaccuracies in the measurement and feeding devices (temperature $\pm 2\%$ of reading, gas flow controllers $\pm 0.8\%$ of reading plus $\pm 0.2\%$ of full scale, water flow controller $\pm 1\%$ of full scale, outlet gas concentrations ± 0.005 vol%, charcoal feeding rate ± 0.05 g/min). In the experiments, X_C is calculated from the carbon mass balance using the product gas flows \dot{n}_{CO} , \dot{n}_{CO_2} and \dot{n}_{CH_4} :

$$X_C = \frac{\dot{n}_{CO} + \dot{n}_{CO_2} + \dot{n}_{CH_4}}{\dot{n}_{0,C}} \quad (5.4)$$

In the simulations, X_C is calculated using the kinetic rate law of Eq. (3.28). X_C increased from 8% at $T_{a,out} = 1000$ K to 31% at $T_{a,out} = 1600$ K. A maximum of 26% is found experimentally

at $T_{a,out} = 1425$ K at a residence time of 0.08 s, which is a significantly lower conversion than that of 87% obtained for continuous vortex-flow reactor at residence times over 1 s and particles directly irradiated [72]. For the given charcoal, steam, and Ar flow rates, a reaction zone length l of 1.43 m would be required to reach complete conversion ($X_C = 100\%$) after 0.62 s residence time at absorber temperatures of 1600 K. The agreement between calculated values and the experimental ones is within $16.8\% \pm 13.8\%$ (mean difference \pm standard deviation).

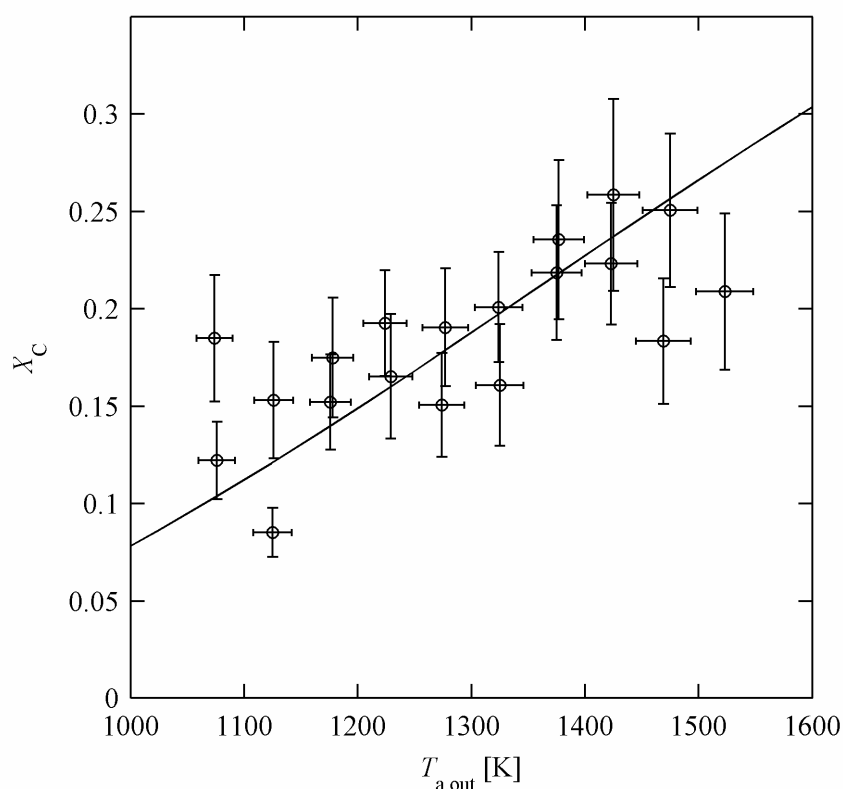


Figure 5.7: Experimentally measured (markers) and theoretically calculated (curve) carbon conversions.

Figure 5.8 shows the overall energy balance calculated for $Q_{solar} = 1$ kW. Re-radiation and conduction losses are predominant, representing 39.4% and 43.4% of Q_{solar} , respectively. In contrast, natural convective heat loss is relatively small, 7.4% of Q_{solar} . The power fraction needed to heat the Ar carrier gas is 5.7% of Q_{solar} , but this heat sink would be eliminated in an industrial application. The heating of the reactants consumes 3.3% of Q_{solar} , but could in principle be recovered by exchanging sensible heat of the hot products exiting the reactor. The portion of energy consumed by the chemical reaction is less than 1% of Q_{solar} , due to the low feeding rate of charcoal and the relatively low carbon conversions. The solar-to-chemical

energy conversion efficiency η , is defined as the portion of the input radiative power absorbed by the chemical reactants, both in the form of sensible heat and chemical process heat,

$$\eta = \frac{X_C \cdot \sum_x^{\text{species}} \int_{473 \text{ K}}^{T_{a,\text{in}}} \dot{n}_x c_{p,x}(T) dT + X_C \cdot \dot{n}_{0,C} \cdot \Delta H_R |_{T_{a,\text{in}}}}{Q_{\text{solar}}} \quad (5.5)$$

$$= \frac{X_C \cdot Q_{\text{reactants}} + Q_{\text{chemistry}}}{Q_{\text{solar}}}$$

Peak measured η was only 1.53%, as no attempts were undertaken to optimize the design of the prototype reactor. Besides the requirement of a longer tubular absorber for higher X_C , increasing the number of absorbers contained in the cavity should augment η as re-radiation by each absorber is incident on the neighbour absorbers.

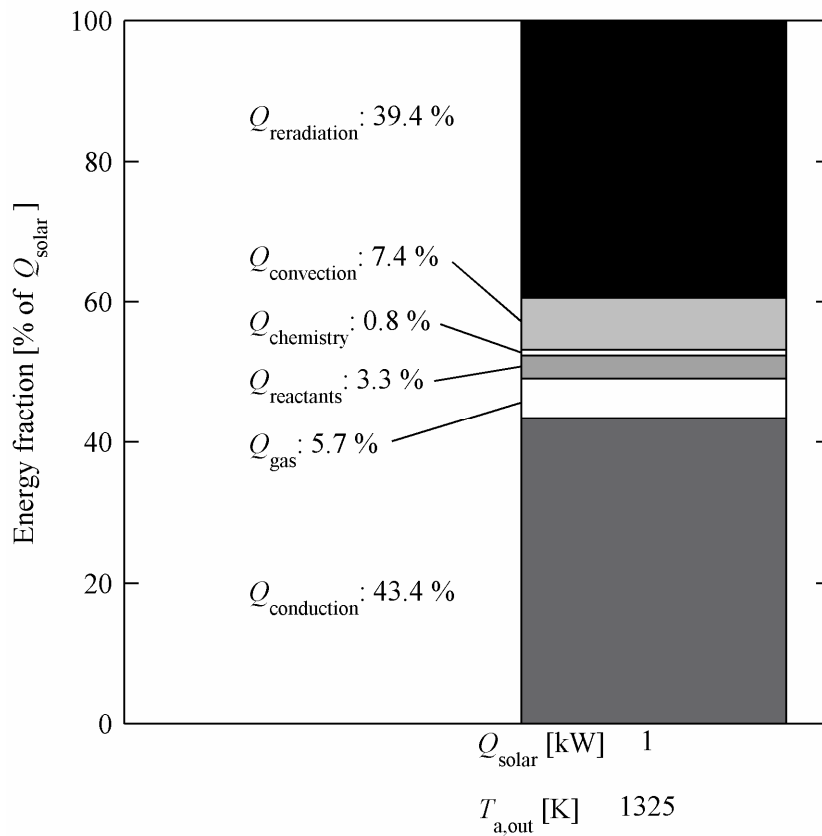


Figure 5.8: Energy balance at input solar power level of 1 kW.

5.5 Reactor scale-up

The reactor model is employed to examine the thermal performance of a scaled-up reactor consisting of a cavity-receiver containing an array of multiple tubular reactors, as depicted in Fig. 5.9. In contrast to the lab-scale reactor, the single-tube absorber is now substituted for an eight-tube absorber. Table 5.1 lists the dimensions and operational conditions of the solar reactor for two solar power input levels: I) Q_{solar} in the range 50 – 150 kW, and II) Q_{solar} in the range 500 – 1500 kW. The radius of a single absorber tube $r_{\text{a,out}}$ was set to 5 and 15 cm, respectively. The radii ratio $r_{\text{a,out}}/r_{\text{c,in}}$ as well as the aperture surface to inner cavity surface area ratio $A_{\text{ap}}/A_{\text{c,in}}$ were kept constant at 0.2 and 0.1465, respectively, for both configurations. The reaction zone length was set equal to the cavity diameter. Charcoal feeding rates ranged from 100 – 500 g/min for case I, and 1000 – 7000 g/min for case II. No Ar is used; charcoal particles are entrained in pure steam flow. The same molar ratio $\text{H}_2\text{O}:\text{C}$ of 1.88 as in lab-scale experiments is assumed.

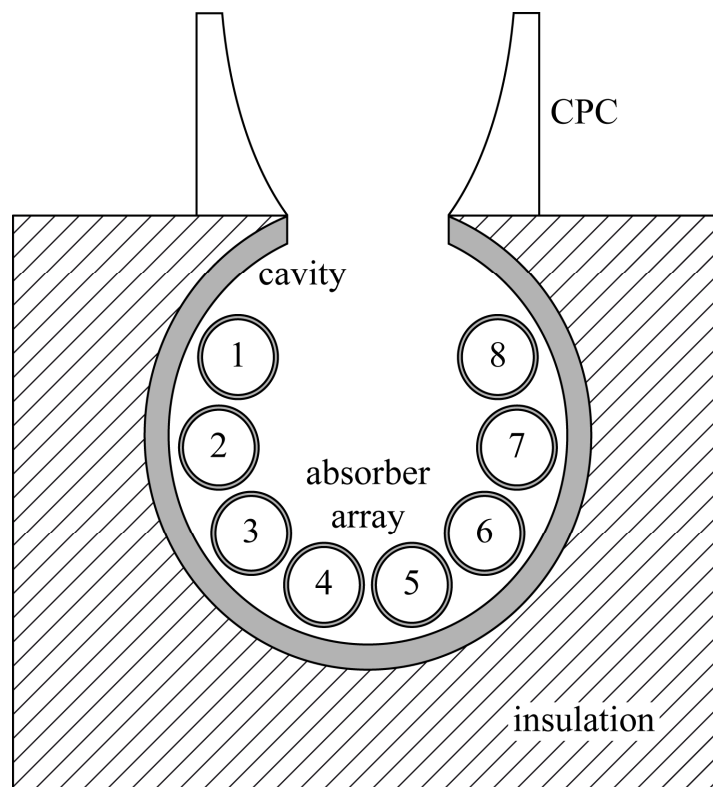


Figure 5.9: Scheme of the scaled-up reactor consisting of a cavity-receiver containing an array of 8 tubular absorbers.

Table 5.1: Dimensional and operational conditions of the solar reactor for two solar power input ranges.

Case	I	II
Solar power input Q_{solar} [kW]	50 – 150	500 – 1500
Aperture width w_{ap} [m]	0.20	0.60
Cavity radius $r_{\text{c,in}}$ [m]	0.25	0.75
Absorber tube radius $r_{\text{a,out}}$ [m]	0.05	0.15
Absorber tube wall thickness [m]	0.007	0.01
Reaction zone length l [m]	0.50	1.50
Average insulation thickness [m]	0.19	0.25
Radii ratio $r_{\text{a,out}}/r_{\text{c,in}}$	0.20	0.20
Surface area ratio $A_{\text{ap}}/A_{\text{c,in}}$	0.1465	0.1465
Charcoal feeding rates $\dot{m}_{\text{charcoal}}$ [g/min]	100 – 500	1000 – 7000
H ₂ O:C molar ratio	1.88	1.88

Average absorber array temperature T_{array} as a function of charcoal feeding rate $\dot{m}_{\text{charcoal}}$ is shown in Fig. 5.10 for both cases I and II. The parameter is $Q_{\text{solar}} = 50, 150,$ and 150 kW for case I, and $Q_{\text{solar}} = 500, 1000,$ and 1500 kW for case II. T_{array} decreases with $\dot{m}_{\text{charcoal}}$ because of the heat consumed to heat the reactants. Temperatures are not uniformly distributed in the absorber array; as absorber tubes 1 and 8 (Fig. 5.9) that are closest to the aperture exhibit the highest temperatures, whereas lowest temperatures are obtained for absorber tubes 4 and 5 located at the rear of the cavity. Maximum temperature differences are 488 and 618 K for cases I and II, respectively.

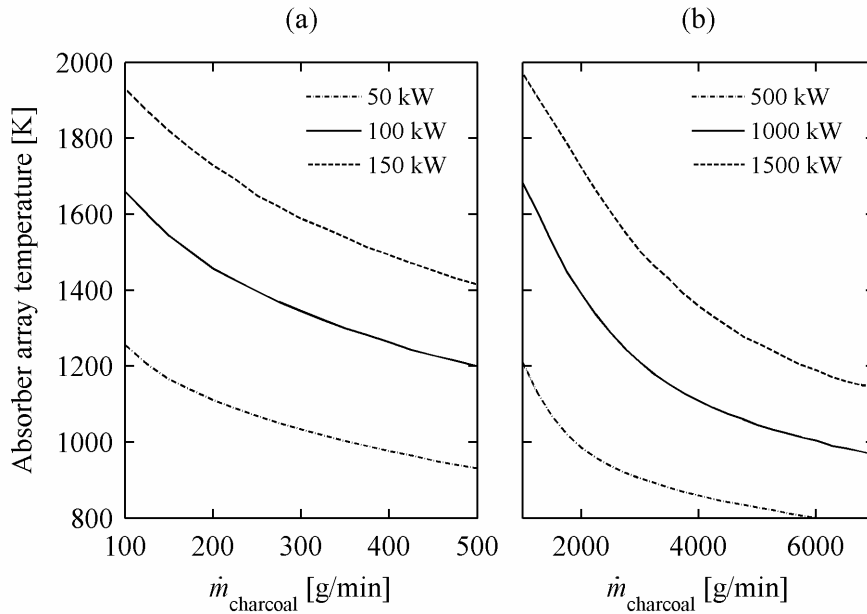


Figure 5.10: Average absorber array temperature as a function of the charcoal feeding rate for a) case I; and b) case II. The parameter is $Q_{\text{solar}} = 50, 100,$ and 150 kW for case I, and $Q_{\text{solar}} = 500, 1000,$ and 1500 kW for case II.

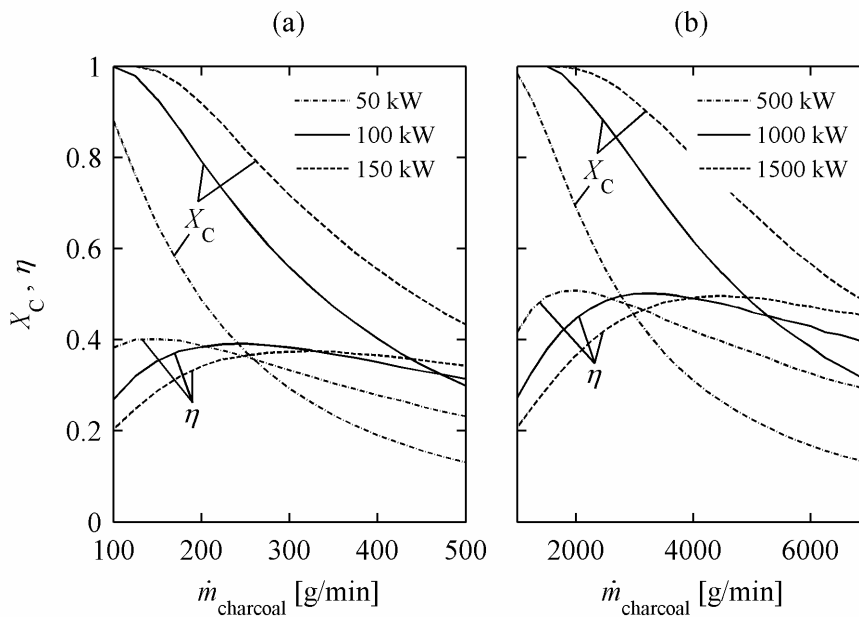


Figure 5.11: Carbon conversion, X_C , and energy conversion efficiency, η , as a function of the charcoal feeding rate for a) case I; and b) case II. The parameter is $Q_{\text{solar}} = 50, 100,$ and 150 kW for case I, and $Q_{\text{solar}} = 500, 1000,$ and 1500 kW for case II.

The carbon conversion, X_C , and the energy conversion efficiency, η , are shown in Fig. 5.11 as a function of the charcoal feeding rate for both cases I and II. The parameter is $Q_{\text{solar}} = 50, 150, \text{ and } 150 \text{ kW}$ for case I, and $Q_{\text{solar}} = 500, 1000, \text{ and } 1500 \text{ kW}$ for case II. As expected, increasing $\dot{m}_{\text{charcoal}}$ leads to lower X_C due to reduced temperature, as observed in Fig. 5.10. At relatively low feeding rates, η increases as the available heat is used efficiently to drive the chemical reaction. However, at higher $\dot{m}_{\text{charcoal}}$, a larger portion of energy is used for heating unreacted feedstock, manifested by low X_C , resulting in a decrease of η . In case I, peak energy efficiencies $\eta = 40.1, 39.1 \text{ and } 37.5\%$ are reached for $Q_{\text{solar}} = 50, 100, \text{ and } 150 \text{ kW}$ with $\dot{m}_{\text{charcoal}} = 150, 250, \text{ and } 325 \text{ g/min}$, respectively. The corresponding carbon conversions are $X_C = 65, 67, \text{ and } 67\%$, respectively. In case II, peak energy efficiencies $\eta = 50.8, 50.1, \text{ and } 49.6\%$ are reached for $Q_{\text{solar}} = 500, 1000, \text{ and } 1500 \text{ kW}$ with $\dot{m}_{\text{charcoal}} = 2000, 3250, \text{ and } 4500 \text{ g/min}$, respectively. The corresponding carbon conversions are $X_C = 69, 74, \text{ and } 74\%$, respectively.

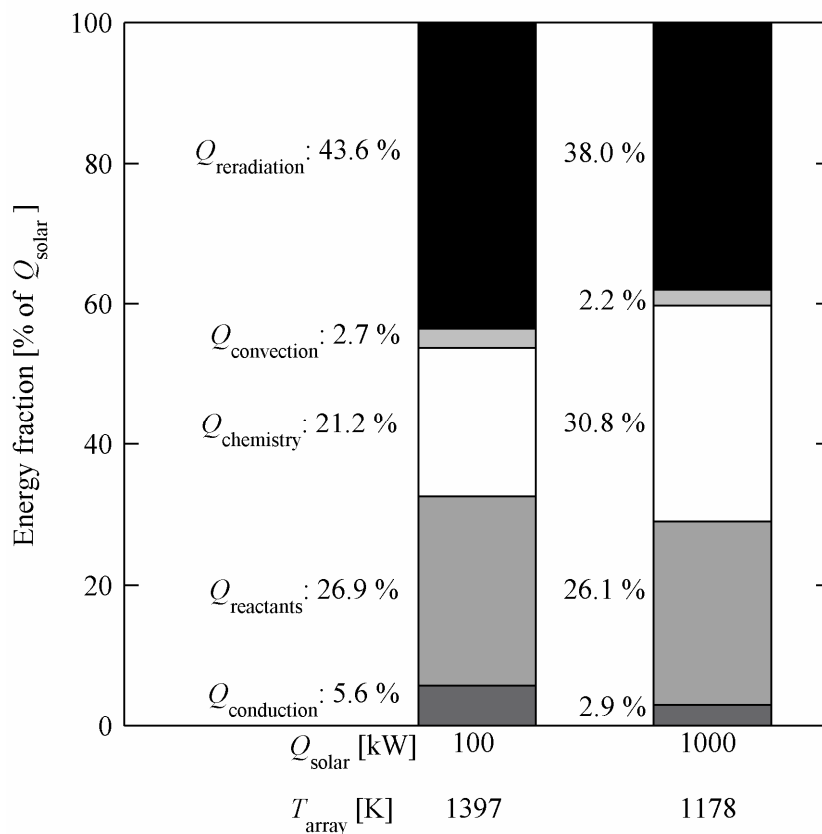


Figure 5.12: Energy balance (in percentage of the solar power input) for case I at input solar power of 100 kW and absorber array temperature of 1397 K, and for case II at input solar power of 1000 kW and absorber array temperature of 1178 K.

Figure 5.12 shows the energy balance for cases I and II with $Q_{\text{solar}} = 100$ and 1000 kW, respectively. According to Fig. 5.11, the optimal $\dot{m}_{\text{charcoal}} = 250$ and 3250 g/min for maximum energy efficiencies are selected for cases I and II, respectively. The corresponding absorber array temperatures are 1397 and 1178 K, respectively, and the corresponding carbon conversions are 66.6 and 74.2% , respectively. In contrast to the lab-scale reactor, only re-radiation losses are predominant at a level of 43.6 and 38.0% of Q_{solar} for cases I and II, respectively, while conduction losses are significantly reduced due to the larger cavity volume-to-surface ratio. As a consequence, η is boosted remarkably and reaches 39.1% by scaling up the reactor from 3 kW (lab-scale prototype) to 100 kW (case I), and further reaches 50.1% by scaling up to 1000 kW (case II). At the locus of maximum η , the fraction consumed by the chemical reaction amounts to 21.2 and 30.8% of Q_{solar} , while the fraction consumed by heating the reactants amounts to 26.9 and 26.1% of Q_{solar} , for cases I and II, respectively.

5.6 Summary and conclusions

The steam-gasification of biochar was experimentally studied using concentrated radiation as the energy source of high-temperature process heat. Validation of the 2D reactor model formulated in chapter 3 was accomplished with 19 experimental runs in terms of temperatures and carbon conversion. Two up-scaled reactor versions for solar power input ranges $50 - 150$ kW and $500 - 1500$ kW, featuring an eight-tube absorber array, were analyzed with the model. As conduction heat losses are reduced significantly due to the favorable volume-to-surface ratio, optimal charcoal feeding rates of 250 and 3250 g/min leads to peak solar-to-chemical energy conversion efficiencies of 39.1 and 50.1% for 100 and 1000 kW solar power input, respectively.

Part II
Zn hydrolysis

6 H₂ production by steam-quenching of Zn vapor in a hot-wall aerosol flow reactor⁶

6.1 Introduction

This chapter focuses on the second step Zn+H₂O reaction of the Zn/ZnO water-splitting cycle, which is thermodynamically favorable at below 1490 K. Previous laboratory studies with steam bubbling through molten zinc in the 723 – 773 K range indicated inhibition of the reaction rate by the formation of a ZnO(s) layer around the steam bubbles [84]. Steam-hydrolysis of zinc powder in batch-mode at above 673 K resulted in a short and fast surface-controlled reaction followed by a slow diffusion-controlled reaction [85]. Zn(g) oxidation with H₂-H₂O mixtures at 773 – 1173 K occurred mainly on the silica tube walls by chemical vapor deposition [86]. Studies on the condensation of Zn(g) in the presence of O₂ by fractional crystallization in a temperature-gradient tube furnace indicated that the oxidation of Zn is a heterogeneous process and, in the absence of nucleation sites, Zn(g) and O₂ can coexist in a meta-stable state [87].

The use of Zn-nanoparticles for the hydrolysis reaction offers some intriguing advantages. Firstly, Zn nanoparticles may undergo complete or nearly complete oxidation to ZnO in short residence times because of the large surface-to-volume ratio. Secondly, their inherent high specific surface area (SSA) augments the reaction kinetics, heat transfer, and mass transfer. Finally, their entrainment in a gas flow allows for continuous feeding of reactants and removal of products. Such Zn nanoparticles can be produced by evaporation-condensation processes in which a Zn(g)-laden gas flow is rapidly quenched to reach oversaturation and thus condensation, either by expansion or by dilution with an inert gas [88]. By this process Weiss et al. [89] and Wegner et al. [90] produced H₂ at up to 70% conversion with respect to limited reactant Zn, but only pure Zn nanoparticles were collected in the filter as ZnO films and filamentary particles were only formed at the reactor walls. Ernst et al. [91] achieved up to 90% H₂ conversion at reactor temperatures in the range 900 – 1273 K, but at the expense of low particle yields downstream. At lower reactor temperatures, in the range 573 – 900 K, they obtained up to 25% particle yield at appreciable ZnO contents (50 wt%) but lower (60%) H₂ conversions. Abu Hamed et al. [92] conducted experiments in a reactor

⁶ Material from this chapter has been published in: T. Melchior, N. Piatkowski and A. Steinfeld. H₂ production by steam-quenching of Zn vapor in a hot-wall aerosol flow reactor. *Chemical Engineering Science* **64** (5): 1095-1101 (2009).

similar to the one used by Weiss et al.[89] at furnace temperatures of 1023 and 1073 K. Conversions ranged from 87% to 96% with residence time varying from 1.7 to 2.1 min. As in previous studies, hydrolysis took place mostly on the reactor walls. Hydrolysis of zinc powder aerosol at reactor wall temperatures between 653 and 813 K was investigated by Funke et al. [93]. Zinc particles with an average size of 158 nm were fed to the reactor by a fluidized bed feeder. Hydrogen conversion increased with temperature reaching 27% at 813 K and a gas residence time of about 0.6 s. Product powder collected downstream in the filter showed conversion of 11% while particles accumulated on the reactor walls were completely oxidized.

The present work examines the simultaneous formation and in-situ hydrolysis of Zn nanoparticles by steam-quenching of Zn(g) in an aerosol flow reactor. Nanoparticle formation requires high cooling rates attained by high quench flow rates and steep temperature gradients [94]. Smaller particles also offer higher SSA and, therefore, augment the reaction rate. In contrast, high temperatures and low gas flow rates, i.e. long residence times, are favorable with regard to the reaction kinetics. Thus, a trade-off between these apparently conflicting aspects becomes crucial for the reactor design and optimization. A systematic parametric study is carried out to investigate the effect of the Zn(g) mass flow rate, quench rate, and reaction zone temperature on the chemical conversion, particle yield, and product particle characteristics. The reactor apparatus is improved to enable quenching rates exceeding 10^4 K/s and up to 10^6 K/s, which significantly affect the particle formation dynamics and, consequently, the reaction kinetics.

6.2 Experimental

A schematic of the hot-wall aerosol flow reactor is depicted in Fig. 6.1. The evaporation zone consists of a 55 mm i.d. quartz tube inside a cylindrical furnace (Carbolite VST 12/300) of 30 cm heated length. An alumina crucible, initially loaded with 3 g of Zn granules (Riedel-de-Haen, 99.99% purity), rests on a balance for on-line monitoring the Zn evaporation rate. Zn vapor is carried by a N₂ flow (99.999% purity) into a 5 mm i.d., 25 cm length quench unit where it is mixed with a preheated H₂O-N₂ flow entering through two lateral 2.5 mm i.d. inlets that are inclined by 70° with respect to the main flow direction [95]. The quench unit is made of stainless steel, except for the Inconel front cap containing the quench gas inlets. This cap is further surrounded by a ceramic disc that closes the annulus between the quench unit and the quartz tube, thus preventing Zn deposition in the void. At the quench zone outlet, the

diameter is expanded from 5 mm to 45 mm in a stainless steel cone of 7.3 cm length. Further connected to the cone is a 45 mm i.d., 50 cm length stainless steel tube, which is wrapped by a heating tape and serves as the temperature-controlled reaction zone. Downstream of the reaction zone, a glass-fiber filter (Whatman GF/A, 150 mm-dia.) is installed at the reactor outlet for product particle collection. After removal of excess water from the effluent gas mixture by a condenser, the outlet flow rate is monitored by an electronic flow meter (Voegtlin). Flow resistances caused by particle deposition on the filter and the reactor walls are overcome with a vacuum pump (Vacuubrand RE 8), adjusted to maintain atmospheric pressure in the reactor. Inlet mass flow rates are adjusted by electronic flow controllers (Bronkhorst).

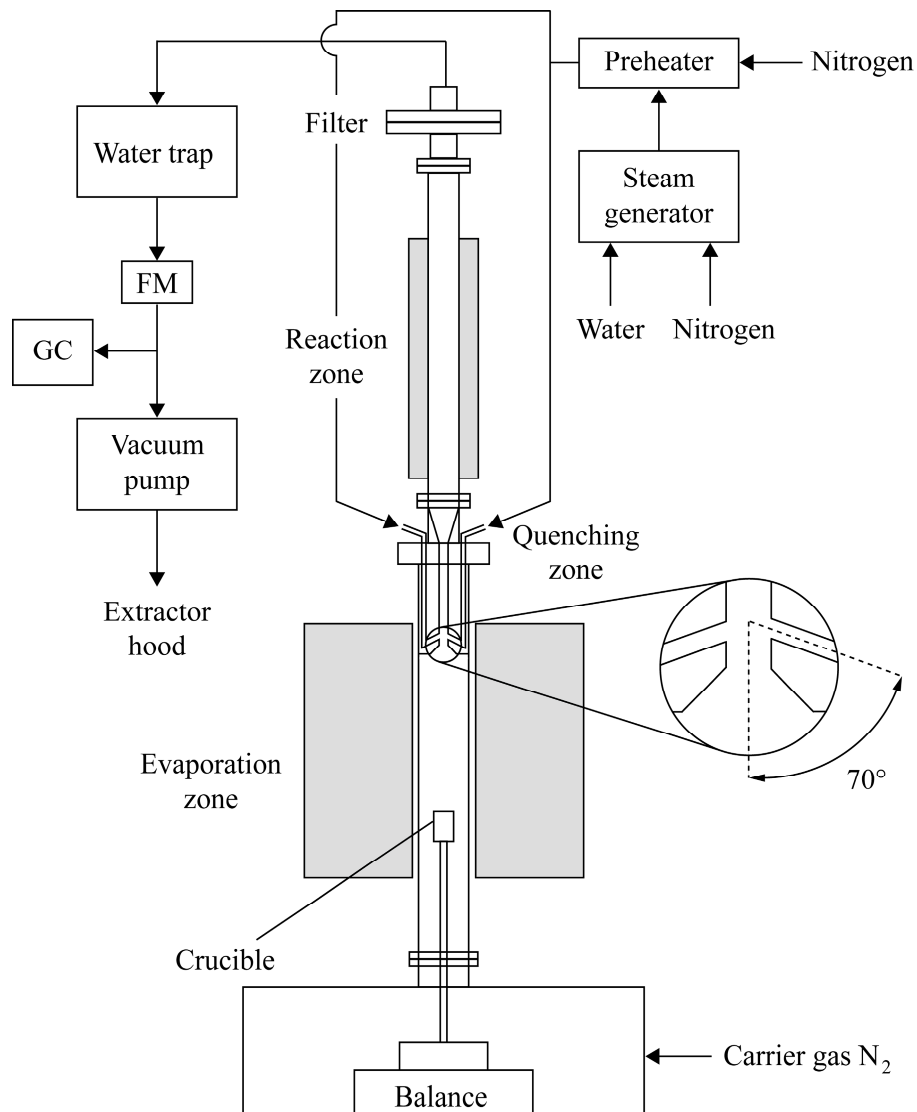


Figure 6.1: Scheme of aerosol flow reactor and periphery for H₂ and ZnO synthesis by steam-hydrolysis of Zn.

Prior to the start of each experiment, the setup was purged with N₂ while the steam-generator, preheater, and reaction zone, were brought to their set temperatures. The evaporation zone furnace and the steam injection were then switched on. After Zn evaporation was completed, the experiment was continued with the same operational settings for additional 10 min before switching off. Experiments were carried out for quench gas flow rates \dot{V}_q in the range 1 – 25 l_n/min, evaporation zone temperatures T_{EZ} in the range 1123 – 1273 K, Zn evaporation rates in the range $1.4 - 9.5 \times 10^{-4}$ mol/min, and reaction zone temperatures T_{RZ} in the range 573 – 873 K. The baseline parametric settings were $T_{EZ} = 1223$ K, $T_{RZ} = 673$ K, $\dot{V}_q = 20$ l_n/min, steam flow rate = 20 g/h, and carrier N₂ flow = 2 l_n/min. Steam and quench gas entered the quench zone at 473 K. The evaporation zone was heated to the desired steady-state temperature at a rate of 20 K/min; its temperature was controlled by the electric furnace. Temperature profiles along the reactor were established in advance for various N₂ flows without Zn/H₂O by moving a 1 mm-diam. type-K thermocouple along the centerline. This thermocouple was removed during the experimental runs with Zn and H₂O to avoid interference with the flow path or with the reaction kinetics. Residence times in the quench unit were calculated from local fluid velocities derived from the measured temperature profiles along the centerline. Cooling rates were calculated from the temperature gradients and residence times in the quenching zone. Temperature gradient in radial direction was neglected as the diameter of the quench unit was relatively small (5 mm i.d.). Maximum temperature differences between centerline and walls at the reaction zone (45 mm i.d.) were 36 and 56 K for $\dot{V}_q = 5$ and 25 l_n/min, respectively. H₂ concentration in the off-gas was measured by gas chromatography (GC, Agilent G2890A micro GC). Solid products were analyzed by X-ray powder diffraction (XRD, Bruker AXS D8, Cu K_α radiation). Crystallite sizes of Zn, d_{Zn} , and ZnO, d_{ZnO} , and phase composition were obtained using the Rietveld method and the fundamental parameter approach [96]. The particle Brunauer-Emmet-Teller (BET) SSA was measured by N₂ adsorption at 77 K (Micromeritics TriStar 3000). Assuming monodisperse spheres, the BET-equivalent particle diameter was calculated as $d_{BET} = 6/(\rho \cdot SSA)$, where $\rho = x_{ZnO}\rho_{ZnO} + (1 - x_{ZnO})\rho_{Zn}$ with $\rho_{Zn} = 7140$ kg/m³, $\rho_{ZnO} = 5606$ kg/m³, and x_{ZnO} the mass fraction of ZnO. The morphology of the particles was examined by scanning electron microscopy (SEM, Zeiss Gemini Supra 55 VP).

The reactor performance was characterized by three indicators: (1) the overall chemical conversion with respect to the limiting reactant Zn, defined as

$$X = \frac{\text{moles of H}_{2,\text{GC}}}{\text{moles of H}_{2,\text{max}}} \quad (6.1)$$

where $\text{H}_{2,\text{GC}}$ refers to the amount of H_2 measured by GC, and $\text{H}_{2,\text{max}}$ to the theoretical maximum amount of H_2 generated assuming complete hydrolysis of the evaporated Zn; (2) the effective particle yield, defined as

$$Y = \frac{\text{moles of Zn}_f}{\text{moles of Zn}_{\text{evap}}} \quad (6.2)$$

where Zn_f denotes the total amount of Zn moles in the Zn/ZnO mixture collected in the filter, and Zn_{evap} is the amount of Zn evaporated; and (3) the ZnO mole fraction in the particles collected at various location,

$$Z = \frac{\text{moles of ZnO}}{\text{moles of Zn} + \text{moles of ZnO}} \quad (6.3)$$

6.3 Results and discussion

6.3.1 Reactor temperature profiles

Figure 6.2 shows the temperature profiles along the axis of the reactor for the baseline parameter settings at two different quench gas flow rates, $\dot{V}_q = 5$ and $25 \text{ l}_n/\text{min}$. The quench gas was injected right behind the evaporation zone leading to a temperature drop in the quench zone from 1223 K to about 600 K. For the quench flow rates considered ranging from 1 to $25 \text{ l}_n/\text{min}$, the corresponding cooling rates over the quench zone ranged from $2 \times 10^4 \text{ K/s}$ to $1 \times 10^5 \text{ K/s}$. In the first 3 cm of the quench zone, the cooling rate exceeded 10^6 K/s for $\dot{V}_q = 25 \text{ l}_n/\text{min}$. Also indicated in Fig. 6.2 is the Zn vapor saturation temperature, T_{sat} , calculated from the Zn partial pressure in the measured flow rate and the saturation vapor pressure [51]:

$$\log_{10} p_{\text{Zn,sat}} = -20.31 - \frac{4636}{T} + 10.07 \log_{10} T - 3.81 \cdot 10^{-3} T + 4.89 \cdot 10^{-7} T^2 \quad (6.4)$$

with p_{Zn} given in mmHg. It shows that Zn vapor is supersaturated and leads to the formation of Zn particles by nucleation and condensation, eventually followed by their in-situ hydrolysis with steam contained in the quenching gas. This arrangement differs from a previous aerosol

reactor concept [91], where steam was injected behind the cooling zone, i.e. after particle formation occurred and where cooling rates were below 10^3 K/s. Centerline temperature fluctuations in the expansion cone indicated local vortex development, while the temperature profile in the reaction zone was rather constant.

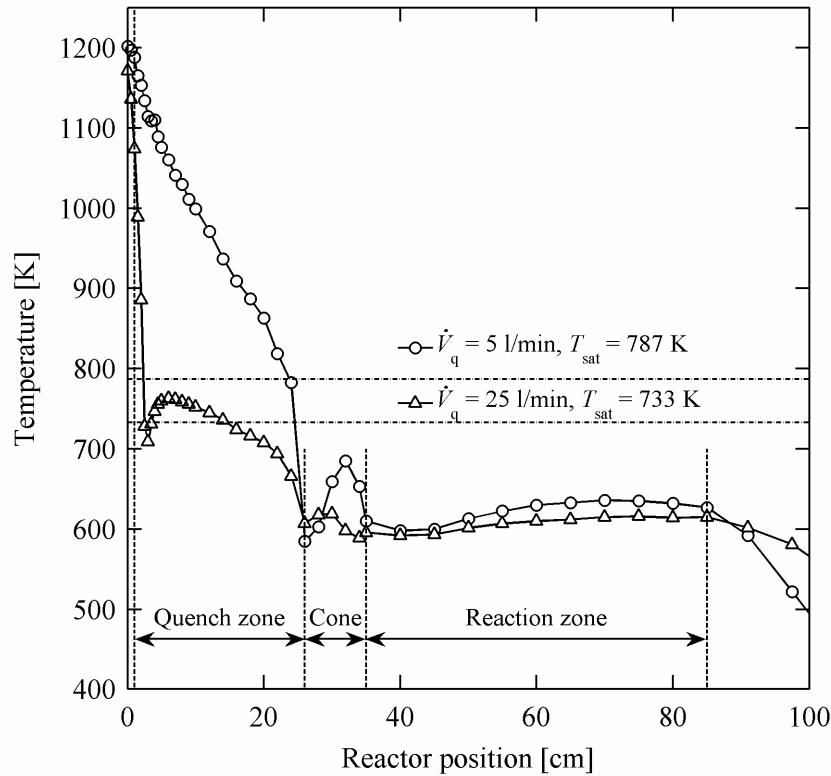


Figure 6.2: Temperature profiles along the quench unit, cone, and reaction zone for $\dot{V}_q = 5$ and 25 l_n/min at $T_{EZ} = 1223$ and $T_{RZ} = 673$ K.

6.3.2 Zn evaporation and H₂ production

The molar Zn evaporation rate, measured on-line by the balance, and the H₂ production rate, measured by GC, are shown in Fig. 6.3 as a function of time, for an experimental run at baseline parametric settings except T_{EZ} . Also indicated is the evaporation zone temperature, T_{EZ} . The close correlation between the Zn and H₂ rate curves confirmed the occurrence of the hydrolysis reaction. They increased rapidly in the early stage of the experimental run, as the evaporation zone was heated. Zn rate peaked at 5×10^{-4} mol/min when T_{EZ} slightly overshoot before stabilizing at 1148 K after 10 min. Over the course of the experiment, a slow decrease in evaporation rate was observed, presumably due to mass transfer limitation as the Zn melt in

the crucible is used up. H_2 rate reached a constant value of about 3×10^{-4} mol/min and appeared seemingly unaffected by the Zn evaporation rate decrease, which may be the result of the hydrolysis of Zn wall deposits, concurrently with that of Zn aerosol. When the Zn evaporation was terminated, H_2 rate dropped but still continued for a few minutes at lower level, most likely caused by slow diffusion-controlled reaction of Zn deposited on the walls.

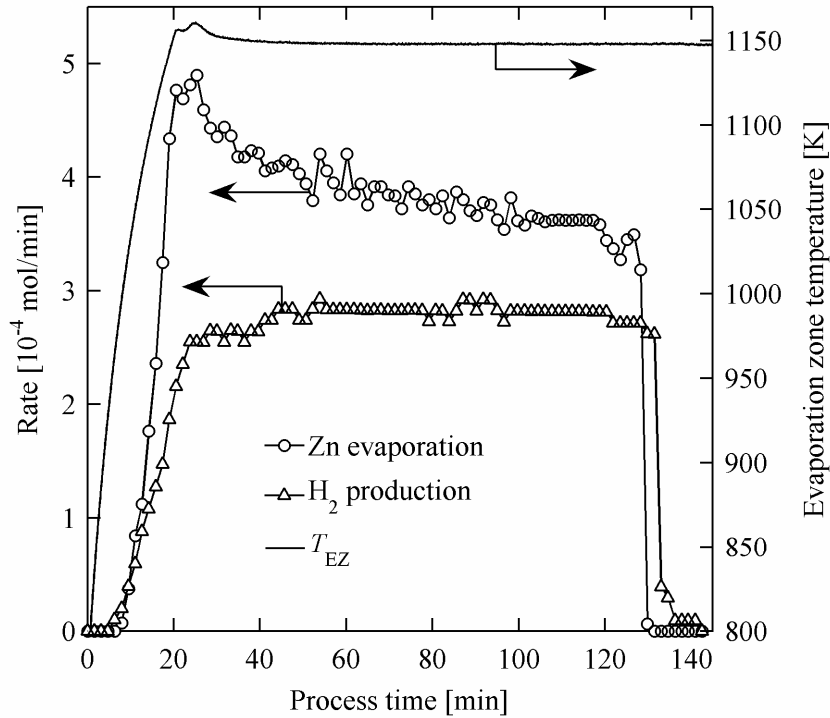


Figure 6.3: Molar rates of Zn evaporation (circles) and H_2 production (triangles), and evaporation zone temperature as a function of time, for the baseline parametric settings except T_{EZ} .

6.3.3 Influence of quenching gas flow rate

Two sets of experiments at $T_{EZ} = 1148$ K and 1223 K, corresponding to Zn evaporation rates of 3 and 7.3×10^{-4} mol/min, respectively, were carried out to investigate the influence of quenching gas flow rate \dot{V}_q on the reactor performance. The resulting overall chemical conversion X (circles) and effective particle yield Y (triangles), as well as the ZnO mole fraction of particles collected in the filter Z (squares) are shown in Fig. 6.4. Increasing \dot{V}_q from 1 to 7.5 l_n/min - corresponding to increasing cooling rates from 2 to 6×10^4 K/s - led to a decrease of X from 95% to about 65%, while a further increase to 25 l_n/min appeared to have

no significant effect on X . Since Y and Z had relatively low values, with maximums of 41 and 22%, respectively, at $\dot{V}_q = 20$ l_n/min and $T_{EZ} = 1148$ K, the major contribution to H₂ production derived from hydrolysis of Zn deposits on the reactor walls. For $\dot{V}_q < 7.5$ l_n/min, less than 3% resulted from the collected samples on the filter. A maximum aerosol contribution of 9% was found for $\dot{V}_q = 20$ l_n/min.

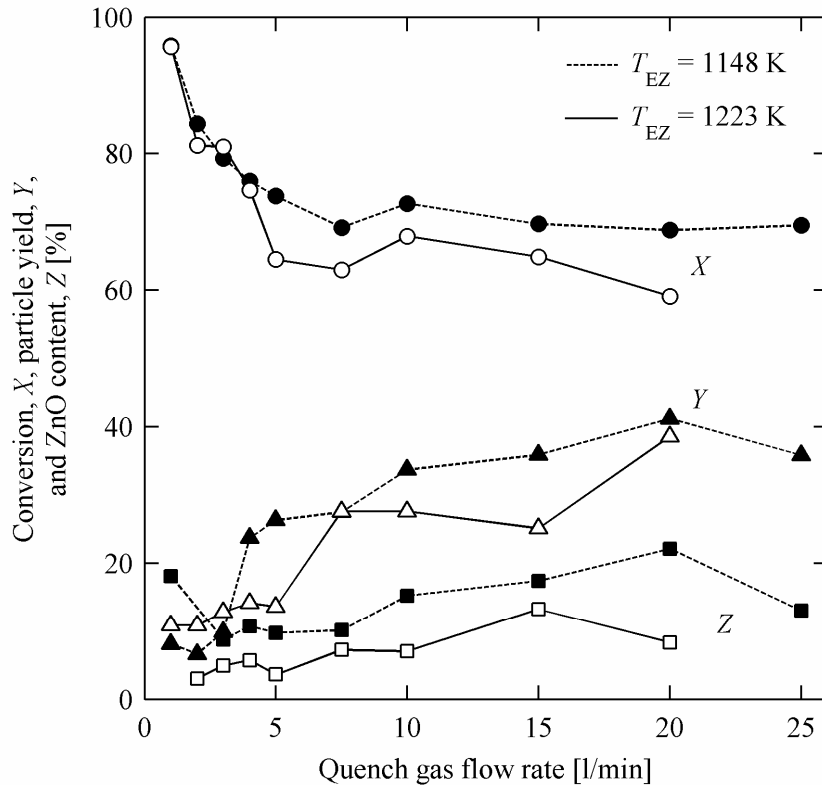


Figure 6.4: Overall chemical conversion, X (circles), effective product particle yield, Y (triangles), and ZnO mole fraction of particles collected in the filter, Z (squares), as a function of quench gas flow rate \dot{V}_q at evaporation temperatures T_{EZ} of 1148 K (dashed line, black markers) and 1223 K (solid line, white markers), with T_{RZ} constant at 673 K.

Deposits were found mainly in the quench zone, especially at low quench flow rates. This is consistent with the particle yield evolution in Fig. 6.4, which increased with \dot{V}_q , leading to lower Zn(g) concentration and shorter residence time in the quench unit, but also to earlier particle formation as T_{sat} is reached faster than at low quench flow rates (as indicated in Fig. 6.2). The lower temperature in the quench unit for high \dot{V}_q may further reduce Zn(g)

diffusion and deposition on the reactor walls [91]. Re-entrainment of previously deposited particles may be possible at high flow rates.

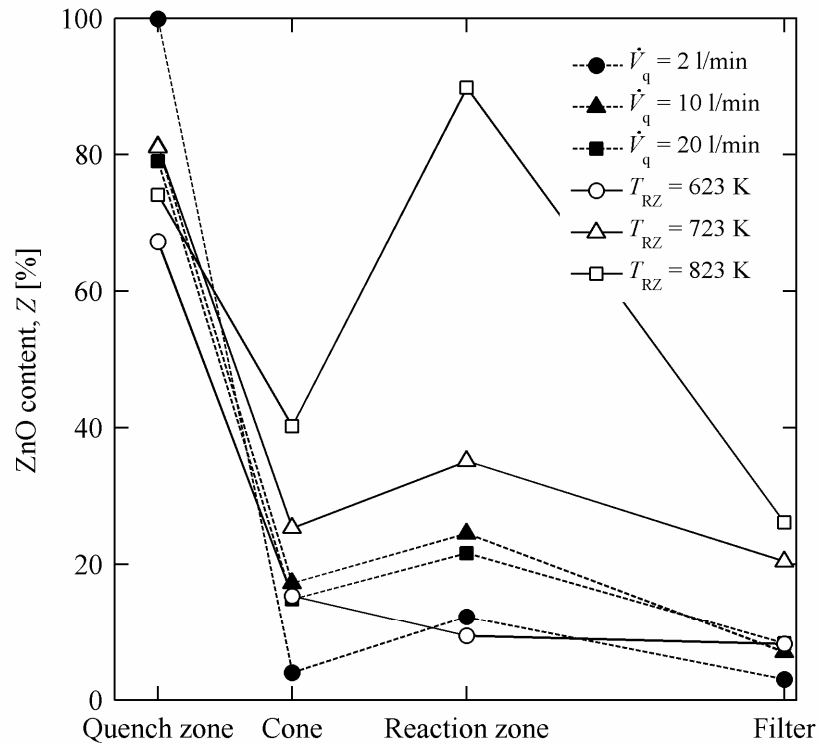


Figure 6.5: ZnO mole fraction of solid products deposited along the flow streamline. Parameters are: $\dot{V}_q = 2, 10,$ and 20 l/min (black markers, $T_{RZ} = 673$ K), and $T_{RZ} = 623, 723,$ and 823 K (white markers, $\dot{V}_q = 20$ l/min).

The reactor wall deposits were analyzed by XRD and the corresponding mole fractions of ZnO along the flow streamline are shown in Fig. 6.5 for a set of three experimental runs at $\dot{V}_q = 2, 10$ and 20 l/min (black markers) with $T_{EZ} = 1223$ K and $T_{RZ} = 673$ K, and for a set of three experimental runs at $T_{RZ} = 623, 723,$ and 823 K (white markers), with $T_{EZ} = 1223$ K and $\dot{V}_q = 20$ l/min. Z was high in the quench unit, corroborating that H_2 mainly originated from hydrolysis of deposits. Pure ZnO ($Z = 100\%$) was found at $\dot{V}_q = 2$ l/min, while $Z = 61 - 92\%$ was obtained at higher flow rates. Thus, higher temperatures in the quench unit at low \dot{V}_q (see Fig. 6.2) favored depositions there with high ZnO mole fraction (see Fig. 6.5, black markers) and, consequently, high chemical conversion (see Fig. 6.4). In these experiments, T_{RZ} had no significant influence on changes in X as it is constant at 673 K.

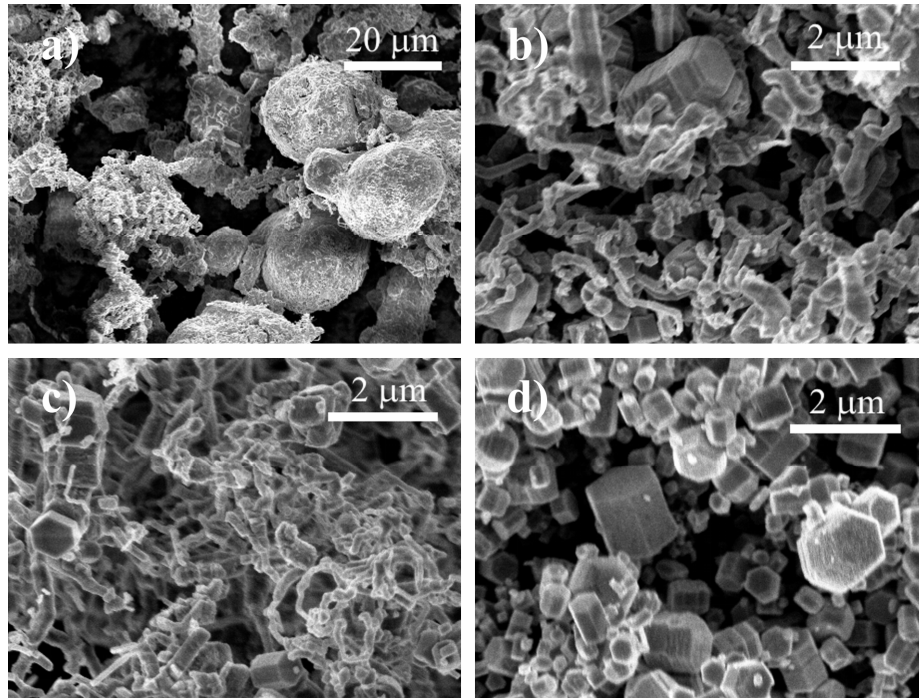


Figure 6.6: SEM pictures of solid products for an experiment at baseline parametric settings collected from: (a) quench unit, (b) reaction zone, and (c) filter ($\dot{V}_q = 20 \text{ l}_n/\text{min}$). Image (d) shows particles collected in the filter in an experiment with $\dot{V}_q = 2 \text{ l}_n/\text{min}$.

SEM pictures of solid products deposited along the reactor are shown in Fig. 6.6(a)-(c) for an experiment conducted at baseline parametric settings. In the quench unit, relatively large spherical-type particles were found with $d_p \approx 20 \mu\text{m}$. Similar morphologies were found previously in the quench zone of a ZnO dissociation-reactor [61], where their formation was explained by both condensation and coalescence of Zn at short residence times in the gas phase. Their rough and edged surface structure most likely resulted from Zn(l)/Zn(s) oxidation. Besides these spheres, layer-like deposits were found, typical for pure ZnO built up by chemical vapor deposition [89], as well as filamentary and rod-like structures. The latter dominate the SEM images of deposits collected from the reaction zone (Fig. 6.6b) and the filter (Fig. 6.6c). These filamentary and rod-like particles formed at short residence time ($\sim 0.9 \text{ s}$ at $\dot{V}_q = 20 \text{ l}_n/\text{min}$) by vapor-solid (VS) mechanism and instantaneous Zn oxidation by hydrolysis [87,91,97]. The Zn crystallite size, as measured by XRD, was rather constant along the reactor at a mean $d_{\text{Zn}} = 108$ and 87 nm for $T_{\text{EZ}} = 1223 \text{ K}$ and 1148 K , respectively, and larger than the ZnO crystallite size d_{ZnO} . In the quench zone, high deposition rates followed by growth on the surface lead to d_{ZnO} of about 65 nm , whereas in the cone, reaction zone, and filter d_{ZnO} was quite stable at 25 nm . Reducing \dot{V}_q from 20 to $2 \text{ l}_n/\text{min}$ changed significantly

the morphology of product particles to crystals with hexagonal geometry, as depicted in Fig. 6.6(d) for filter deposits ($d_p \approx 0.1\text{--}1.5 \mu\text{m}$). Such particles are typical for temperatures below the Zn bulk melting point (693 K) [61,87,91], with enough residence time (~ 7 s) to be formed by nucleation and condensation in the aerosol. Few crystals were also present at high quench flow rates (Fig. 6.6c), although smaller in size due to shorter growth time. Assuming that these large Zn crystals served as sites for the hydrolysis reaction, the increase of ZnO mole fraction for filtered particles with \dot{V}_q (Fig. 6.4) was most likely due to the change of particle formation mechanism. Filamentary particles featured ZnO molar fractions of up to 22%, while only small fractions of 3 – 11% were detected for the large crystalline particles.

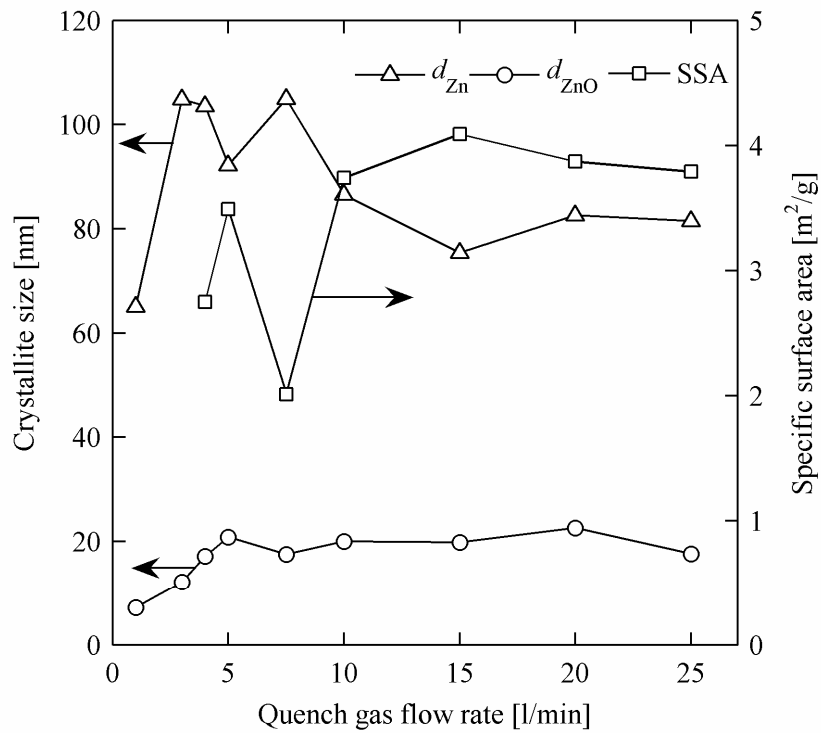


Figure 6.7: Specific surface area SSA (squares) and crystallite sizes of Zn (triangles) and ZnO (circles) of particles collected in the filter as a function of quench gas flow rate \dot{V}_q .

The d_{Zn} , d_{ZnO} , and SSA are plotted in Fig. 6.7 as a function of \dot{V}_q for samples collected from the filter at $T_{EZ} = 1148$ K. The trend in d_{Zn} and SSA is not clear, especially at low quench flow rates ($\dot{V}_q \leq 7.5$ l_n/min) where hexagonal particle formation prevails, indicating coupled effects of various parameters. Growing crystallite size would be expected for

decreasing quench flow rate due to longer residence time and higher Zn(g) concentration [94]. On the other hand, increase in depositions in the quench unit at lower \dot{V}_q causes lower local Zn(g) concentrations which favor the production of smaller particles. Further, the location of supersaturation within the quench unit, which is critical for the nucleation and growth process, is considerably affected by vapor concentration, quench gas flow rate, and temperature [61]. Thus, various explanations can be found for the spread of data in Fig. 6.7, including particle transport by diffusion and thermophoresis [98]. However, it was not possible to completely elucidate these coupled effects. It is observed that the SSA ranges from 2 m²/g ($d_{\text{BET}} = 430$ nm) to 3.5 m²/g ($d_{\text{BET}} = 247$ nm) at $\dot{V}_q \leq 7.5$ l_n/min, and follows a similar trend as d_{Zn} , with d_{ZnO} slightly increasing from 7 to 20 nm, indicative of particle dynamics controlled primarily by Zn nucleation-condensation rather than by Zn hydrolysis [91], in agreement with SEM observations (Fig. 6.6(d), hexagonal structures). The difference between d_{BET} and d_{Zn} , in the range 65–105 nm, indicates polycrystallinity and particle agglomeration [91]. For $\dot{V}_q > 7.5$ l_n/min, where particle formation shifts to mainly filamentary structures (Fig. 6.6c), the d_{Zn} , d_{ZnO} , and SSA are rather constant at 80 nm, 20 nm and 3.9 m²/g (corresponding to $d_{\text{BET}} = 230$ nm), respectively. Here, the increase in \dot{V}_q , resulting in a reduction of residence time from ~1.8 s to ~0.8 s, seems to have only limited effect on particle production and hydrolysis reaction. Similar observations were made for experiments with $T_{\text{EZ}} = 1223$ K, albeit the overall crystallite and particle sizes were bigger.

6.3.4 Influence of Zn evaporation rate

Figure 6.4 shows X , Y and Z (for particles collected in the filter) at $T_{\text{EZ}} = 1148$ and 1223 K. To further explore the effect of T_{EZ} , a set of nine experimental runs was carried out at baseline parametric settings and for T_{EZ} varying from 1123 to 1273 K, which results in Zn evaporation rates from 1.4×10^{-4} mol/min to 9.5×10^{-4} mol/min. As expected, low evaporation rates lead to the formation of smaller particles [94], with $d_{\text{Zn}} = 70$ nm and SSA = 3.9 m²/g (corresponding to $d_{\text{BET}} = 230$ nm). In contrast, increasing the Zn(g) partial pressure lead to the formation of larger particles with $d_{\text{Zn}} = 120$ nm and lower SSA of 1 m²/g ($d_{\text{BET}} = 870$ nm). Again, d_{ZnO} was rather constant at 21 nm. However, observations from Fig. 6.4 with regard to X and Y did not confirm as the chemical conversion and particle yield did not change significantly with T_{EZ} . An average X , Y , and Z of 62%, 40%, and 15%, respectively, were found over the whole range of evaporation rates.

6.3.5 Influence of reaction zone temperature

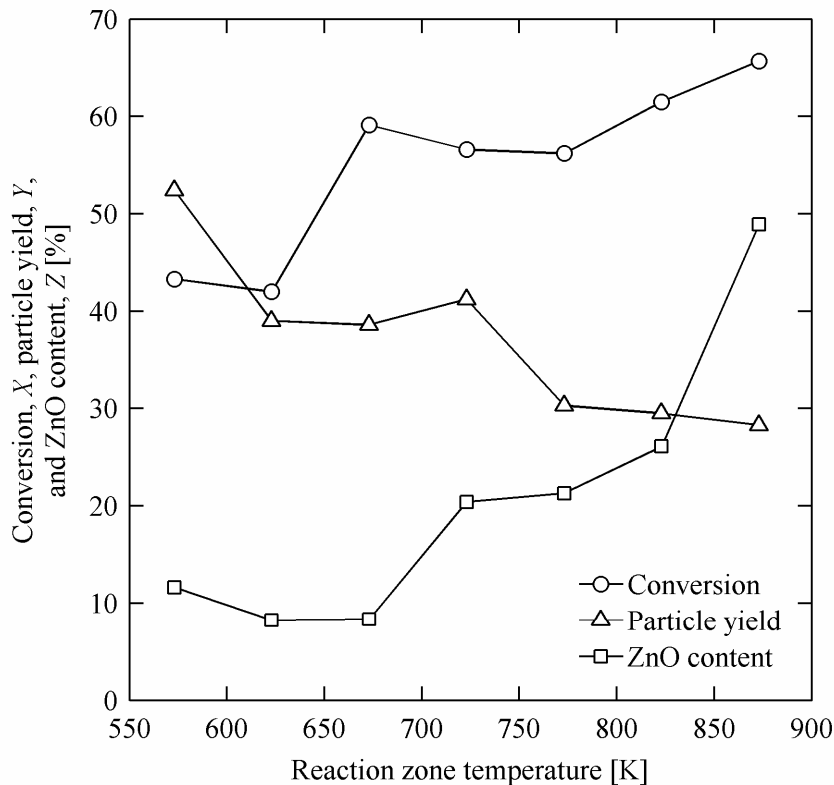


Figure 6.8: Overall H₂ conversion, X (circles), effective product particle yield, Y (triangles), and ZnO mole fraction for particles collected in the filter, Z (squares), as a function of the reaction zone temperature T_{RZ} at baseline parametric settings.

Figure 6.8 shows X , Y , and Z for particles collected in the filter as a function of the reaction zone temperature T_{RZ} , ranging from 573 to 873 K. X increased from 42% to 66% over the considered temperature range, in agreement with previous observations [91,93]. A similar trend was observed for Z , with a strong increase from 8% to 49% as T_{RZ} exceeds the Zn m.p. (693 K). This can be also seen in Fig. 6.5 (white markers), where Z is nearly constant in the quench unit at 76%, but it increased with temperature from a low of 9% to 90% for particles collected in the reaction zone. Although Y decreased with T_{RZ} from 52 to 28%, the H₂ generation that can be attributed to hydrolysis of gas-borne particles increased. From the overall 43% of Zn converted to H₂ at $T_{RZ} = 573$ K, only 6% was derived from the filtered particles, whereas the remaining 37% was derived from hydrolysis of Zn deposits on the reactor walls. At $T_{RZ} = 873$ K, 22% are attributed to filtered particles and the remaining 44% to wall deposits. Evidently, higher temperatures augment the hydrolysis kinetics at the reactor

walls (Fig. 6.5). This, in combination with increased Zn(g) diffusion, leads to a decrease in Zn vapor concentration and, consequently, lower particle yield.

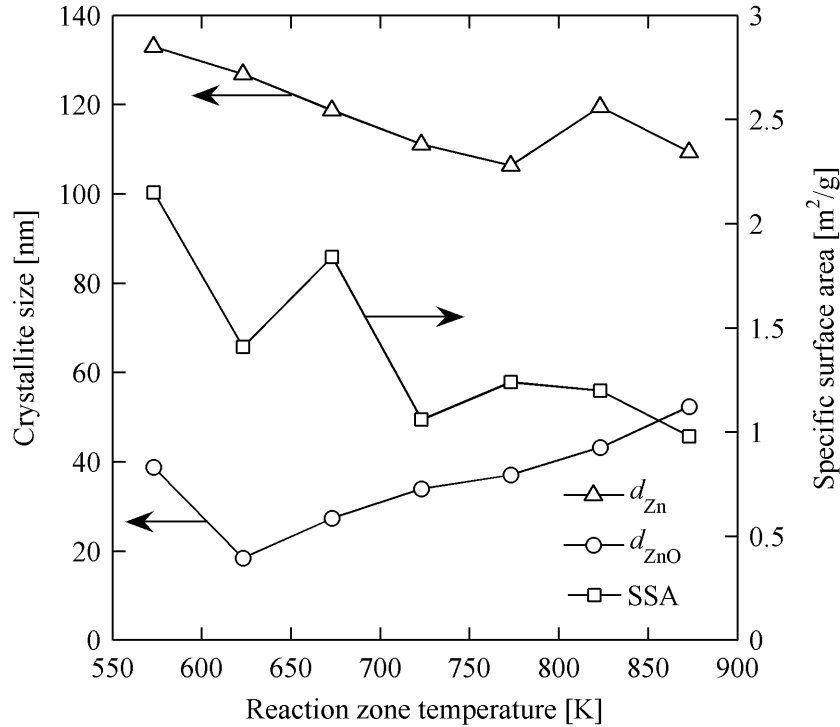


Figure 6.9: Specific surface area SSA (squares) and crystallite sizes of Zn (triangles) and ZnO (circles) of particles collected in the filter as a function of reaction zone temperature T_{RZ} at baseline parametric settings.

XRD analysis of deposits in the quench unit revealed mean d_{Zn} and d_{ZnO} of 120 and 64 nm, respectively, unaffected by T_{RZ} . In contrast, growing of deposits and enhanced reaction at elevated temperatures on the reaction zone are manifest as d_{Zn} and d_{ZnO} increase from 92 to 116 nm, and 30 to 50 nm, respectively. The SSA, d_{Zn} , and d_{ZnO} of product particles on the filter are shown in Fig. 6.9 as a function of temperature. These particles feature similar morphologies to those in Fig. 6.6(c) (filaments) as the quench gas flow rate is set to 20 l_n/min (baseline). The decrease of d_{Zn} from 133 to 106 nm, in combination with the increase of d_{ZnO} from 18 to 52 nm, indicates particle growth rather by surface reaction than by vapor condensation. Additionally, extended particle agglomeration occurs, probably by coagulation, as the SSA decreases from 2.15 to 0.98 m^2/g . Hence, d_{BET} does not follow the same trend as d_{Zn} , as seen in quench flow parameter experiments (Fig. 6.7), but increases from 400 to 970 nm over the considered temperature range. Coagulation further reduces particle deposition on

the tube walls, as smaller particles exhibit higher deposition rates by diffusion and thermophoresis [98]. This is in contradiction with the decrease of Y with T_{RZ} (Fig. 6.8). However, it is believed that the aforementioned loss of Zn(g) to the reactor wall outweighs this effect.

6.4 Summary and conclusions

Combined H₂ and Zn/ZnO nanoparticle production by steam-quenching of a Zn(g)-laden gas stream was achieved in a hot-wall tubular aerosol flow reactor. The influence of quenching gas flow rate, Zn evaporation rate, and wall temperature on the chemical conversion, particle yield, and ZnO content was investigated. Decreasing the quench flow rate from 25 to 1 l_n/min (which corresponds to decreasing cooling rates from 1×10^6 to 2×10^4 K/s) led to a maximum chemical conversion of 95%, mainly due to wall deposits and increased temperature in the quench unit. Particle yield was consequently low. At low quench flow rates, long residence times favored the formation of sharp-edged hexagonal particles with low ZnO content, controlled by Zn nucleation-condensation mechanism. At high quench flow rates above 7.5 l_n/min (cooling rates $> 6 \times 10^4$ K/s), particle yield increased, featuring filamentary and rod-like morphologies formed by vapor-solid growth mechanism. Here, surface reaction and coagulation dominated particle dynamics as observed in experimental runs with varying reaction zone temperatures downstream of the quench unit at a quench flow rate of 20 l_n/min. As the reaction zone temperature was increased from 573 to 873 K, overall chemical conversion increased from 42% to 66% while particle yield decreased from 52% to 28%, as confirmed by the higher ZnO content of wall deposits and enhanced Zn vapor deposition.

At 873 K, the maximum H₂ yield derived exclusively from hydrolysis of gas-borne particles collected in the filter was 22% H₂. This performance indicator will have to be significantly increased for a large-scale industrial implementation. Further improvements are concerned with the elimination of wall deposits - via the injection of an annular quenching flow [62] or by the use of a fluid-wall tube [67] - as these affect the continuous-mode of operation.

7 Reaction zone modeling

7.1 Introduction

Agglomerate powders as found in high quench flow rate experiments usually result from coagulation controlled processes [99]. The inherent assumption of instantaneous coalescence in the classical coagulation theory fails when the fusion is slow. An early model accounting for the effect of sintering on the aggregate structure and particle collision rate was presented by Ulrich and Riehl [100]. Koch and Friedlander [101] modeled the evolution of the primary particle size, taking into account the influence of coagulation on sintering. However, the effect of aggregate structure on particle collision rate was not included, and the model was limited to the free molecule regime. A detailed two-dimensional sectional model was developed by Xiong and Pratsinis [102], describing the evolution of both aggregate volume and surface area distributions during simultaneous chemical reaction and coagulation from the free molecular to the continuum regime. The sintering law was included in the general dynamic aerosol equation. Synthesis of titania, silica [103] and boron particles [104] was investigated. Kruijs et al. [105] incorporated the effect of particle structure by implementing the collision radius for fractal-like aggregates [106]. Although this monodisperse model is not as accurate as sectional [102,107] or bimodal models [108], it has been successfully applied to synthesis of silicon [105], titania [109-111] and copper metal particles [112].

Zn nanoparticle production was simulated with a 1D monodisperse model accounting for particle nucleation, condensation, coagulation and vapor and particle wall losses by diffusion and thermophoresis at non-isothermal conditions [113]. The model was used to analyze the evaporation-condensation process in the cooling zone of a reactor similar to the present one [91]. Hydrolysis reaction was not included in the model. In this chapter, the reaction zone of the Zn-hydrolysis reactor is simulated. The case of high quench flow rate is considered, where filamentary particles were formed (Fig. 6.6c). Coagulation and sintering of aggregate particles is modeled based on the 1D monodisperse model by Kruijs et al [105]. The model further accounts for hydrolysis surface reaction, and vapor and particle wall deposition by diffusion.

7.2 Model

The hydrolysis rate of submicron Zn particles was measured by thermogravimetric analysis and quantified by a core-shell model [114]. Kinetics for the fast surface reaction were determined:

$$\dot{r}_s = k_s \cdot y_{\text{H}_2\text{O}}^{0.5} \cdot \exp\left(-\frac{E_a}{R_u T}\right) \quad (7.1)$$

with $k_s = 2 \times 10^{-5} \text{ mol cm}^{-2} \text{ s}^{-1}$ and $E_a = 42800 \text{ J/mol}$. The reaction is half-order with respect to water vapor mole fraction $y_{\text{H}_2\text{O}}$. In TG experiments, the fast surface reaction was followed by a parabolic conversion profile dependent on Zn ion diffusion through a ZnO layer. In the present model, only surface reaction is considered. At the prevailing residence times of less than 1 s, diffusion limited reaction is negligible.

The model domain is the reaction zone of length $l = 50 \text{ cm}$ and inner diameter $d_t = 4.5 \text{ cm}$ (Fig. 6.1). At the entrance of the reaction zone ($x = 0$), a mixture of nitrogen (inert carrier gas), Zn/ZnO particles, steam, Zn vapor and hydrogen enters the tube. Incoming particles are assumed to be spherical. Irregular aggregates are then formed by coagulation and partial sintering. Zn vapor may react with steam on the surface of Zn/ZnO particles coating them with ZnO, and deposit on the reactor walls. Thus, the depletion of Zn vapor along the reactor axis can be expressed as:

$$\frac{dC_{\text{Zn(g)}}}{dx} = -\frac{\dot{r}_s A_{\text{aerosol}}}{u} - \frac{4K_m (C_{\text{Zn(g)}} - C_{\text{Zn(g),w}})}{d_t u} \quad (7.2)$$

where $C_{\text{Zn(g)}}$ is the concentration of Zn vapor per unit mass of N_2 carrier gas (mol/kg). The reaction rate of Eq. (7.1) was modified to include dependency on Zn vapor mole fraction, $y_{\text{Zn(g)}}$:

$$\dot{r}_s = k_s \cdot y_{\text{H}_2\text{O}}^{0.5} \cdot y_{\text{Zn(g)}}^{0.5} \cdot \exp\left(-\frac{E_a}{R_u T}\right) \quad (7.3)$$

Just as for steam, the order was set to 0.5 in a first estimate as 1 mole of Zn reacts with 1 mole of steam. u is the average gas velocity calculated from the total gas flow, including nitrogen, steam, hydrogen and Zn vapor, at the reaction zone temperature T_{RZ} . A_{aerosol} is the total aerosol surface area concentration (m^2/kg).

The second term on the right hand side (RHS) of Eq. (7.2) accounts for Zn vapor wall losses by diffusion [115] where $C_{\text{Zn(g),w}}$ is the vapor concentration at the reactor wall and the monomer mass transfer coefficient is [40]:

$$K_m = Sh_{d_t} \frac{D}{d_t} \quad (7.4)$$

If $(Re_{d_t} Sc / (l/d_t)) < 8$, where Re and Sc are the Reynolds and Schmidt number, respectively, the Sherwood number is a constant:

$$Sh_{d_t} = 3.66 \quad (7.5)$$

Otherwise, the correlation is of the form:

$$Sh_{d_t} = 1.86 \left(\frac{Re_{d_t} Sc}{l/d_t} \right)^{1/3} \quad (7.6)$$

The monomer diffusivity D , is calculated according to the Chapman-Enskog equation [116]:

$$D = \frac{3}{8} \frac{k_B T}{P \pi \left(\frac{d_m + d_{N_2}}{2} \right)^2} \left(\pi k_B T \frac{1 + (M_{Zn}/M_{N_2})}{M_{Zn}/N_A} \right)^{1/2} \quad (7.7)$$

where the total pressure $P = 10^5$ Pa, and the diameter of a nitrogen carrier gas atom $d_{N_2} = 3.75 \times 10^{-10}$ m [116]. N_A is the Avogadro number. The Zn monomer (molecule) diameter is calculated from the Zn monomer volume $v_{Zn} = 1.52 \times 10^{-29}$ m:

$$d_m = \left(\frac{6v_{Zn}}{\pi} \right)^{1/3} \quad (7.8)$$

Assuming that all aggregates contain the same number of equally sized primary particles, the balance for the number concentration of particles, N (#/kg), is:

$$\frac{dN}{dx} = - \frac{0.5 \beta_{coag} N^2 \rho_{N_2}}{u} - \frac{4K_p (N - N_w)}{d_t u} \quad (7.9)$$

The first term on the RHS of Eq. (7.9) accounts for the loss of particles by coagulation. Further assuming that the collision rates for Brownian motion (β_B) and laminar shear (β_{sh}) are additive [117], the collision frequency function β_{coag} is:

$$\beta_{coag} = \beta_B + \beta_{sh} \quad (7.10)$$

The effect of the fractal-like agglomerate structure is incorporated in β_{coag} by the collision diameter [106]:

$$d_{col} = d_{prim} \left(\frac{v_{agg}}{v_{prim}} \right)^{1/D_f} = d_{prim} n_{prim}^{1/D_f} \quad (7.11)$$

where D_f is the mass fractal dimension, v_{agg} is the volume of an aggregate, calculated from the total aerosol volume V (m^3/kg), and number concentration N :

$$v_{\text{agg}} = \frac{V}{N} \quad (7.12)$$

and d_{prim} is the primary particle size:

$$d_{\text{prim}} = \frac{6v_{\text{agg}}}{a_{\text{agg}}} \quad (7.13)$$

with the surface area of an aggregate particle a_{agg} :

$$a_{\text{agg}} = \frac{A_{\text{aerosol}}}{N} \quad (7.14)$$

The number of primary particles n_{prim} per agglomerate is:

$$n_{\text{prim}} = \frac{v_{\text{agg}}}{v_{\text{prim}}} \quad (7.15)$$

where v_{prim} is the volume of a primary particle:

$$v_{\text{prim}} = \frac{\pi d_{\text{prim}}^3}{6} \quad (7.16)$$

The expression of the collision frequency is given by Fuchs' interpolation from the free molecular to the continuum regime [118], where the solid sphere diameter is replaced by the collision radius [105]:

$$\beta_B = 8\pi D_p d_{\text{col}} \left[\frac{d_{\text{col}}}{d_{\text{col}} + \sqrt{2}g_{\text{trans}}} + \frac{4\sqrt{2}D_p}{cd_{\text{col}}} \right]^{-1} \quad (7.17)$$

The particle diffusion coefficient D_p is given by:

$$D_p = \frac{k_B T C_c}{3\pi\mu_{\text{N}_2} d_{\text{col}}} \quad (7.18)$$

with the Cunningham correction factor:

$$C_c = \frac{5 + 4Kn + 6Kn^2 + 18Kn^3}{5 - Kn + (8 + \pi)Kn^2} \quad (7.19)$$

The Knudsen number is defined as:

$$Kn = \frac{2\lambda_{\text{gas}}}{d_{\text{col}}} \quad (7.20)$$

with the gas mean free path:

$$\lambda_{\text{gas}} = \frac{2\mu_{\text{N}_2}}{P} \sqrt{\frac{\pi R_u T}{8M_{\text{N}_2}}} \quad (7.21)$$

The transition parameter g_{trans} , particle mean free path λ_p , and particle velocity c are given by:

$$g_{\text{trans}} = \frac{1}{3d_{\text{col}}\lambda_p} \left[(d_{\text{col}} + \lambda_p)^3 - (d_{\text{col}}^2 + \lambda_p^2)^{3/2} \right] - d_{\text{col}} \quad (7.22)$$

$$\lambda_p = \frac{8D_p}{\pi c} \quad (7.23)$$

$$c = \sqrt{\frac{8k_B T}{\pi\rho_p v_{\text{agg}}}} \quad (7.24)$$

where ρ_p is the particle density:

$$\rho_p = x_{\text{ZnO}}\rho_{\text{ZnO}} + (1 - x_{\text{ZnO}})\rho_{\text{Zn}} \quad (7.25)$$

with $\rho_{\text{ZnO}} = 5606 \text{ kg/m}^3$, $\rho_{\text{Zn}} = 7140 \text{ kg/m}^3$, and x_{ZnO} is the mass fraction of ZnO in particles calculated from molar ZnO content Z_p (Eq. (7.34)). For shear-induced coagulation, the collision frequency among particles is [117]:

$$\beta_{\text{sh}} = \frac{4}{3} d_{\text{col}}^3 G \quad (7.26)$$

where the shear rate G in laminar flow is the velocity gradient in radial direction du/dr .

The second term on the RHS of Eq. (7.9) accounts for particle losses to the reactor walls. The particle mass transfer coefficient, in analogy to Eq. (7.4), is [113]:

$$K_p = Sh_{d_t} \frac{D_p}{d_t} \quad (7.27)$$

The total aggregates volume concentration V increases by surface chemical reaction and decreases by particle deposition on the walls:

$$\frac{dV}{dx} = \frac{\dot{r}_s A_{\text{aerosol}} N_A v_{\text{ZnO}}}{u} - \frac{4K_p (N - N_w) V}{d_t u} \quad (7.28)$$

with the ZnO monomer volume $v_{\text{ZnO}} = 2.41 \times 10^{-29} \text{ m}^3$.

The balance for the total aggregate surface area concentration is given by:

$$\frac{dA_{\text{aerosol}}}{dx} = -\frac{1}{\tau_{\text{sin}}} (A_{\text{aerosol}} - Na_{\text{sp}}) + \frac{4\dot{r}_s A_{\text{aerosol}} N_A v_{\text{ZnO}}}{d_{\text{prim}} u} - \frac{4K_p (N - N_w) A_{\text{aerosol}}}{d_t u} \quad (7.29)$$

It decreases by coalescence, calculated with the first term on the RHS, where a_{sp} is the surface area of the agglomerate volume-equivalent sphere:

$$a_{sp} = \left(6\sqrt{\pi}v_{agg}\right)^{2/3} \quad (7.30)$$

The characteristic sintering time for ZnO is [97]:

$$\tau_{sin} = \frac{0.013k_B T d_{prim}^4}{16bD_{GB}\gamma v_{ZnO}} \quad (7.31)$$

Only grain-boundary diffusion is used, as it is supposed to mainly control the sintering mechanism at the given conditions [97]. b is the grain-boundary width, D_{GB} is the grain-boundary diffusion coefficient ($bD_{GB} = 1.59 \times 10^{-12} \exp[-235140/(R_u T)] \text{ m}^3 \text{ s}$), and $\gamma = 0.735 \text{ J m}^{-2}$ is the ZnO surface tension. The characteristic sintering time for ZnO is used as the outer layer of the particles is supposed to consist of ZnO. Using the characteristic time for viscous sintering of Zn instead would lead to faster sintering and smaller specific surface areas.

The second term on the RHS of Eq. (7.29) is the increase of surface area by chemical reaction. It is calculated according to the relation derived by Jeong and Choi [108] for aggregate surface growth:

$$\left. \frac{dA_{aerosol}}{dx} \right|_{sg} = \frac{4}{d_{prim}} \left. \frac{dV}{dx} \right|_{sg} \quad (7.32)$$

The evolution of ZnO contained in particles per unit mass of carrier gas (mol/kg) is expressed as:

$$\frac{dC_{ZnO}}{dx} = \frac{\dot{r}_s A_{aerosol}}{u} - \frac{Z_p}{N_A v_{ZnO}} \frac{4K_p (N - N_w) V}{d_t u} \frac{V}{N} \quad (7.33)$$

with the ZnO mole fraction in particles Z_p :

$$Z_p = \frac{C_{ZnO}}{C_{ZnO} + C_{Zn(s)}} \quad (7.34)$$

Solid zinc in particles is lost along the reactor axis by particle deposition:

$$\frac{dC_{Zn(s)}}{dx} = - \frac{(1 - Z_p) 4K_p (N - N_w) V}{N_A v_{ZnO} d_t u} \frac{V}{N} \quad (7.35)$$

Reactor walls are regarded as perfect sinks for particles and vapor, thus $N_w = 0$ and $C_{Zn(g),w} = 0$. Zn vapor depositing on the wall is assumed to react instantly with steam to form ZnO(s). The same accounts for Zn vapor depletion by reaction on aerosols (Eq. (7.2)). As 1

mole of Zn reacts with 1 mole of steam to produce 1 mole of ZnO and 1 mole of hydrogen, the steam and hydrogen concentrations are calculated by the following equations:

$$C_{\text{H}_2\text{O}} = C_{\text{H}_2\text{O},0} - (C_{\text{Zn(g)},0} - C_{\text{Zn(g)}}) \quad (7.36)$$

$$C_{\text{H}_2} = C_{\text{H}_2,0} + (C_{\text{Zn(g)},0} - C_{\text{Zn(g)}}) \quad (7.37)$$

Finally, the process time is obtained from:

$$t = \frac{x}{u} \quad (7.38)$$

The set of Eqs. (7.2), (7.9), (7.28), (7.29), (7.33), (7.35) and (7.38) was solved with the fourth-order Runge-Kutta method.

7.3 Results and discussion

The results of the simulation are compared to experimental findings from chapter 6. Experiments where the influence of the reaction zone temperature (section 6.3.5) was studied are of interest for the present investigation. In these experimental runs, the total N_2 gas flow rate was constant at 22 l_n/min. Steam flow rate was set to 20 g/h ($\dot{n}_{\text{H}_2\text{O,feed}} = 3.08 \times 10^{-4}$ mol/s). Several assumptions have to be taken with regard to flow rates and concentrations at the reaction zone inlet. From experiments, the Zn evaporation molar flow rate is known: $\dot{n}_{\text{Zn,evap}} = 1.22 \times 10^{-5}$ mol/s. It was observed that a certain amount of zinc deposits in the quench zone. In high quench flow rate experiments, the lowest overall conversion of 42% was found at a reaction zone temperature of 573 K (Fig. 6.8). Particle yield and ZnO molar content of particles in the filter were at 52 and 12%, respectively. From the known ZnO content of particles collected from the various reactor zones (Fig. 6.5), it was calculated that about 44% of the evaporated zinc must have deposited in the quench unit in order to obtain the total hydrogen yield of 42%. Hence, the incoming Zn flow rate to the reaction zone was set in simulations to 66% of $\dot{n}_{\text{Zn,evap}}$. It is further unknown how much of this Zn enters the reaction zone in solid form (particles) and as vapor. This is described by the initial particle fraction parameter $Y_{p,0}$, which is the ratio of incoming solid zinc to total incoming zinc (solid + vapor). Additionally, particles are assumed to have converted by $Z_{p,0} = 5\%$ to ZnO, which is the lowest ZnO content found for particles collected in the cone right behind the quench zone and just in front of the reaction zone. Thus, the incoming flow rates of solid Zn and ZnO (in particles), and Zn vapor are calculated as:

$$\dot{n}_{\text{Zn(s)},0} = 0.66 \cdot Y_{\text{p},0} (1 - Z_{\text{p},0}) \dot{n}_{\text{Zn,evap}} \quad (7.39)$$

$$\dot{n}_{\text{ZnO},0} = 0.66 \cdot Y_{\text{p},0} \cdot Z_{\text{p},0} \cdot \dot{n}_{\text{Zn,evap}} \quad (7.40)$$

$$\dot{n}_{\text{Zn(g)},0} = 0.66 (1 - Y_{\text{p},0}) \dot{n}_{\text{Zn,evap}} \quad (7.41)$$

The corresponding concentrations are found by dividing the molar flow rates by the N₂ mass flow rate (4.58×10^{-4} kg/s). Figure 6.5 (white markers) further shows that the ZnO content of particles collected from the quench unit was rather constant at about 76%. This determines the inlet flow rate of hydrogen. Taking also into account the small particle conversion $Z_{\text{p},0}$ of 5%, it is given by:

$$\dot{n}_{\text{H}_2,0} = (0.44 \cdot 0.76 + 0.66 \cdot Y_{\text{p},0} \cdot Z_{\text{p},0}) \dot{n}_{\text{Zn,evap}} \quad (7.42)$$

As 1 mole of H₂ is produced from 1 mole of steam, the inlet flow rate of steam is:

$$\dot{n}_{\text{H}_2\text{O},0} = \dot{n}_{\text{H}_2\text{O,feed}} - \dot{n}_{\text{H}_2,0} \quad (7.42)$$

In the experimental investigation, deposits collected from the quench unit, reaction zone and filter were analyzed by XRD and SEM. However, no information on particle characteristics by in-situ measurements in the flow during the experiments is available. Abu Hamed et al. [92] performed in-situ measurements with a scanning differential mobility sizer in a hot wall flow reactor, where Zn particles were formed by evaporation-condensation process and partially oxidized by steam. A bimodal distribution was detected with one mode centered just below 10 nm and the other at or above 70 nm. The former was attributed to freshly formed particles by homogeneous nucleation. In the simulation, the initial primary particle size d_{prim} is set to 10 nm as a baseline setting. Other baseline parametric settings are $Y_{\text{p},0} = 0.25$, reaction zone temperature $T_{\text{RZ}} = 873$ K, and a fractal dimension D_f of 1.8, which is common for cluster-cluster aggregation in the free molecule as well as the continuum regime [119]. Parametric studies were carried out for $Y_{\text{p},0} = 0.25, 0.50$ and 0.75 , and primary particle diameters of 1, 10 and 100 nm. Fractal dimensions of 1.8, corresponding to rather open clusters, 2.5 and 3.0, corresponding to compact clusters, were used. Furthermore, the effect of sintering time was investigated. Note that the pre-exponential factor in Eq. (7.3) was set to $k_s = 2 \times 10^{-3} \text{ mol cm}^{-2} \text{ s}^{-1}$ in simulations. This was necessary to resolve the mass/heat transfer differences between TG and reactor setup and the fact that a dependency on Zn vapor mole fraction was introduced. Note that Zn used in present experiments differed in purity from the Zn used in TG experiments. Reactivity of Zn strongly depends on composition, morphology and impurities as observed in batch-mode experiments [85].

7.3.1 Effect of initial particle fraction and initial primary particle diameter

Numerically calculated overall chemical conversions and particle ZnO content are depicted in Fig. 7.1 for simulations at baseline parameter settings in the temperature range 550 to 900 K with initial particle fractions $Y_{p,0}$ of 0.25 ($N_0 = 6.60 \times 10^{16} \text{ kg}^{-1}$), 0.50 ($N_0 = 1.32 \times 10^{17} \text{ kg}^{-1}$) and 0.75 ($N_0 = 1.98 \times 10^{17} \text{ kg}^{-1}$). In addition experimentally measured values are given (markers). Chemical conversion X , calculated by dividing the hydrogen outlet flow by the Zn evaporation rate, is increasing over the considered temperature range from 58, 51 and 45% to 64, 58, and 49% for $Y_{p,0} = 0.25, 0.50$ and 0.75 , respectively. The same trend is observed for particle ZnO content Z_p . At 550 K, only low particle ZnO content of 6.5 % is found for the three different initial particle fractions, due to slow reaction kinetics. Increasing the reaction zone temperature leads to an increase of Z_p to 35, 27 and 19% at 900 K for $Y_{p,0} = 0.25, 0.50$ and 0.75 , respectively. Obviously, X and Z_p decrease with $Y_{p,0}$. This is due to the fact that at higher $Y_{p,0}$ less zinc vapor is available for surface reaction. Overall, the agreement between numerically computed conversion and particle ZnO content values and the experimentally measured ones is reasonably good. Numerical values obtained for $Y_{p,0} = 0.25$ are closest to experimental data points, except at low temperatures where values with $Y_{p,0} = 0.75$ are closer. This indicates that the initial particle fraction may not be constant in experiments, and that the reaction zone temperature may influence the quench zone. Figure 7.1 further shows that the ZnO particle content strongly increases at high temperatures (50 % at 873 K), which is not observed in numerical simulations. Here, the slope of the corresponding curves is leveling off towards higher temperatures as a result of Zn vapor availability. At high temperatures, the Zn vapor is totally used up by surface reaction and wall deposition, whereas at low temperatures, a certain amount of vapor is still left at the end of the reaction zone. This is a further indication that the reaction zone temperature may influence the quench zone. At high temperatures, less than 44% of the evaporated zinc may have deposited in the quench unit.

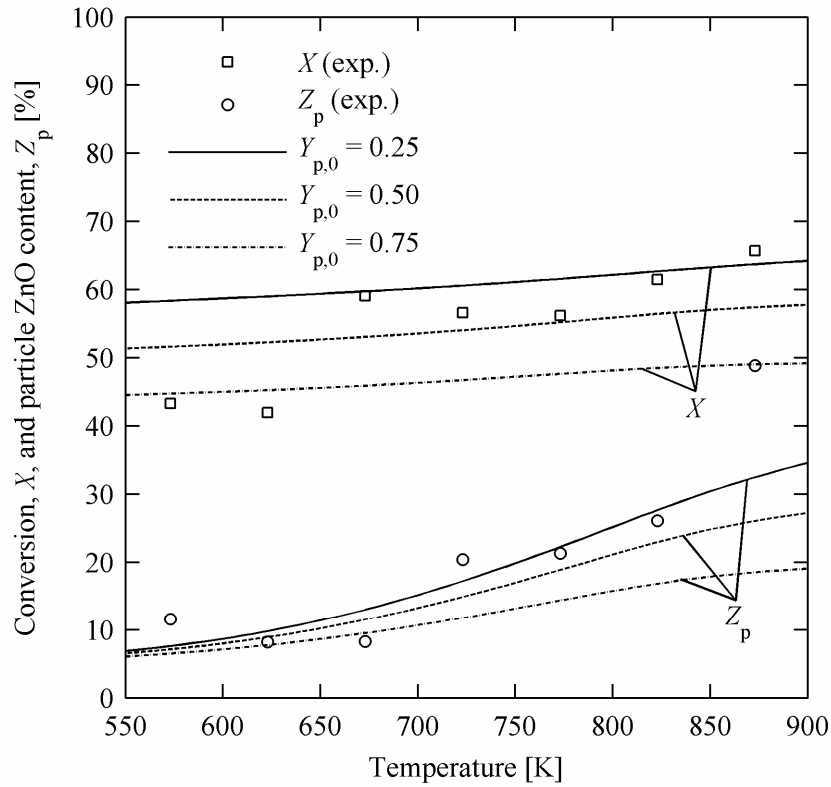


Figure 7.1: Numerically calculated (curves) and experimentally measured (markers) chemical conversion X and particle ZnO content Z_p as a function of reaction zone temperature for $Y_{p,0} = 0.25, 0.50$ and 0.75 .

Although the agreements in X and Z_p are relatively good, a significant difference was observed for specific surface areas. In experiments, BET equivalent diameters of particles collected from the filter were in the range 400 to 970 nm. In simulations, primary particle size remained nearly constant at 10 nm for low temperatures and only increased to 15 nm at high temperatures, which is obviously due to low sintering rates. The effect of initial primary particle size on particle evolution is therefore investigated. The evolution of the total aggregate particle number concentration is shown in Fig. 7.2 for reaction zone temperatures of 573 and 873 K, and for initial primary particle diameters $d_{\text{prim},0}$ of 1, 10 and 100 nm. The corresponding initial number concentrations N_0 are 6.6×10^{19} , 6.6×10^{16} and $6.6 \times 10^{13} \text{ kg}^{-1}$.

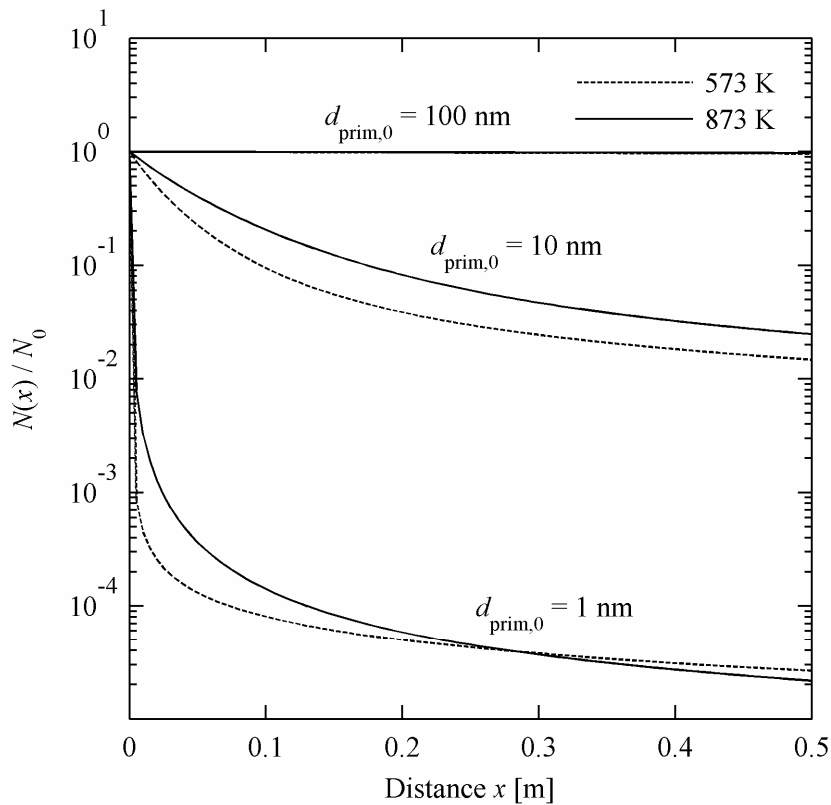


Figure 7.2: Evolution of relative number concentration of aggregates for initial primary particle sizes of 1, 10 and 100 nm, and for reaction zone temperatures of 573 and 873 K.

The decay in the number concentration increases for decreasing particle size. This is primarily due to the different initial concentrations. Coagulation is a strong function of inlet particle concentration and process residence time [98]. Higher concentrations lead to higher collision rates, as seen for particles with initial primary particle size of 1 nm. For large particles with $d_{\text{prim},0} = 100$ nm, the number concentration only slightly decreases from 6.60×10^{13} to 6.38×10^{13} . In case of small initial primary diameters, the decay is enhanced by the formation of aggregates with large collision diameter (see also Fig. 7.4). Figure 7.2 further shows that the decay is stronger at low temperature. This is to some extent due to the sintering rate. Although sintering is slow, it still results in the formation of slightly more compact particles with smaller collisional cross section. Towards the end of the reaction zone, the decay in number concentration for particles with initial primary diameter of 1 nm is slightly stronger at the high temperature of 873 K, which is a result of enhanced wall deposition by diffusion. Overall, coagulation by Brownian motion accounts for more than 99% of the total decay in all cases. Thus, shear-induced coagulation is negligible compared to Brownian coagulation. This

is confirmed by the low values (below 2×10^{-3}) of the Peclet number $Pe = 3\pi\mu_{N_2} d_p^3 G / 8k_B T$, which is a measure of the importance of shear relative to Brownian coagulation [99]. Wall deposition of particles may increase by thermophoresis, as seen in previous studies [98,113]. Especially for large particles, thermophoresis is the dominant mechanism for particle transport to the tube wall [98]. This was however not included in the present isothermal model. In addition, it is believed that rather isothermal conditions prevail in the reaction zone, reducing thermophoresis to a minimum.

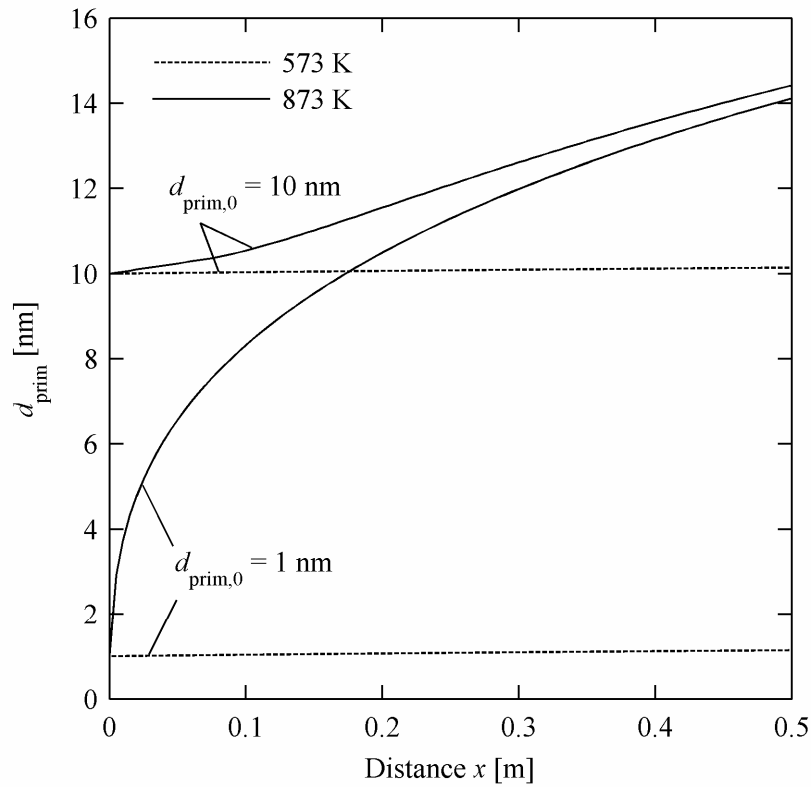


Figure 7.3: Evolution of the primary particle size for initial primary particle diameters of 1 and 10 nm, and reaction zone temperatures of 573 and 873 K.

The evolution of the primary particle size d_{prim} is shown in Fig. 7.3 for reaction zone temperatures of 573 and 873 K, and $d_{\text{prim},0} = 1$ and 10 nm. Not shown are the results for $d_{\text{prim},0} = 100$ nm, as d_{prim} was practically constant at 100 nm. As the temperature increases, the primary particle diameter increases as well. At 573 K, sintering is extremely slow resulting in nearly constant d_{prim} . At 873 K, the curves for $d_{\text{prim},0} = 1$ and 10 nm nearly converge with final values at end of reaction zone of about 14 nm.

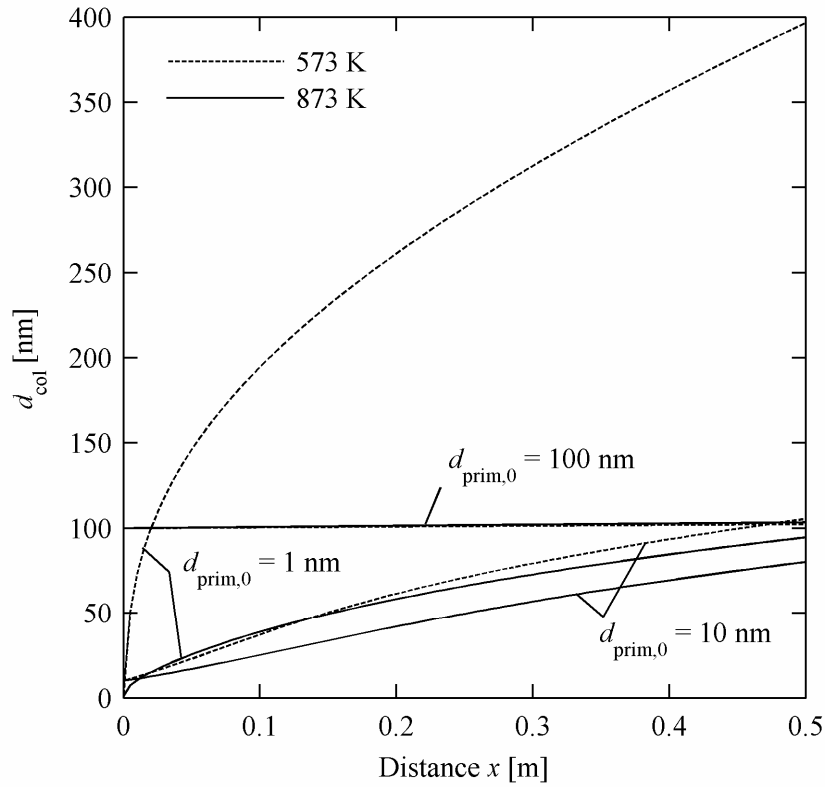


Figure 7.4: Evolution of the agglomerate collision diameter for initial primary particle sizes of 1, 10 and 100 nm, and for reaction zone temperatures of 573 and 873 K.

Figure 7.4 shows the evolution of the agglomerate collision diameter. As particles only partially coalesce, the collision diameter exceeds the primary particle diameter, especially at low temperatures. Coagulation and low sintering rates lead to a high degree of aggregation, which is also reflected by the number of primary particles per aggregate, whose evolution is depicted in Fig. 7.5. For $d_{\text{prim},0} = 1$ nm, collision diameters of 397 and 95 nm are obtained at $x = 0.5$ m for $T_{\text{RZ}} = 573$ and 873 K, respectively. The corresponding number of primary particles per aggregate is $n_{\text{prim}} = 3.76 \times 10^4$ at 573 K and $n_{\text{prim}} = 31$ at 873 K. In the case of $d_{\text{prim},0} = 10$ nm, $d_{\text{col}} = 106$ nm at 573 K with $n_{\text{prim}} = 68$, and $d_{\text{col}} = 80$ nm at 873 K with $n_{\text{prim}} = 22$. As only very low coagulation rate is observed for $d_{\text{prim},0} = 100$ nm, the collision diameter and number of primary particles per aggregate remain nearly constant at 100 nm and 1.

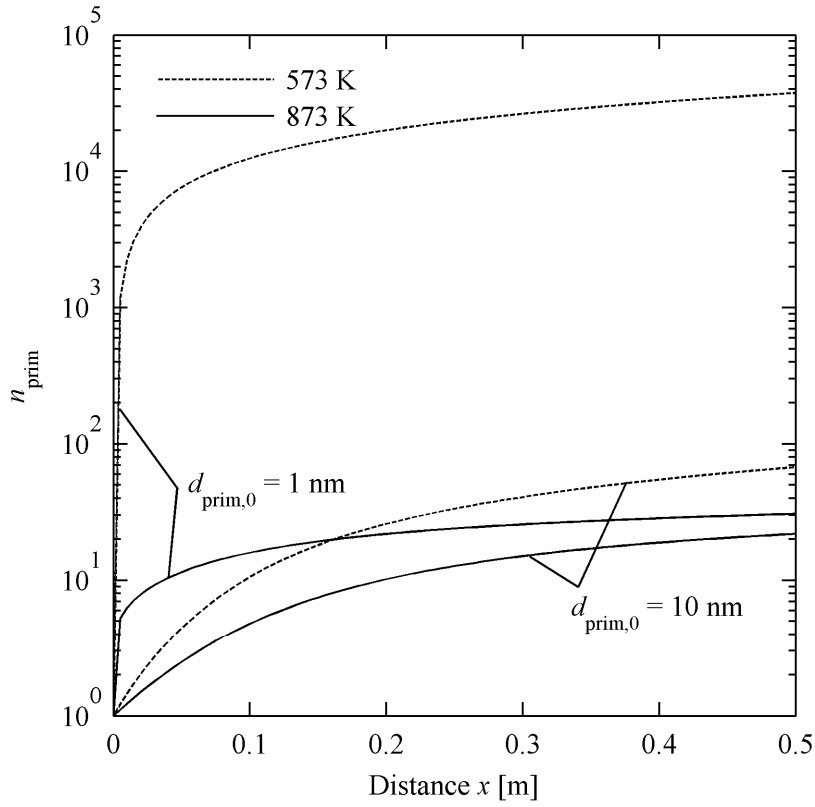


Figure 7.5: Evolution of the primary particle size for initial primary particle diameters of 1 and 10 nm, and reaction zone temperatures of 573 and 873 K.

7.3.2 Effect of fractal dimension and sintering time

The evolutions of primary particle diameter d_{prim} , collision diameter d_{col} , and number of primary particles per aggregate n_{prim} are shown in Fig. 7.6 for fractal dimensions D_f of 1.8, 2.5 and 3.0 at baseline parametric settings ($d_{\text{prim},0} = 10$ nm, $T_{\text{RZ}} = 873$ K, $Y_{\text{p},0} = 0.25$). An increase in fractal dimension, corresponding to the formations of more compact clusters, results in smaller collision diameters d_{col} , which decreases from 80 nm for $D_f = 1.8$ to 40 nm for $D_f = 2.5$ and 30 nm for $D_f = 3.0$ at $x = 0.5$ m. Hence, the number of primary particles per aggregate decreases with D_f due to slower coagulation. As seen in a previous study [105], the primary particle size is insensitive to variation of the fractal dimension.

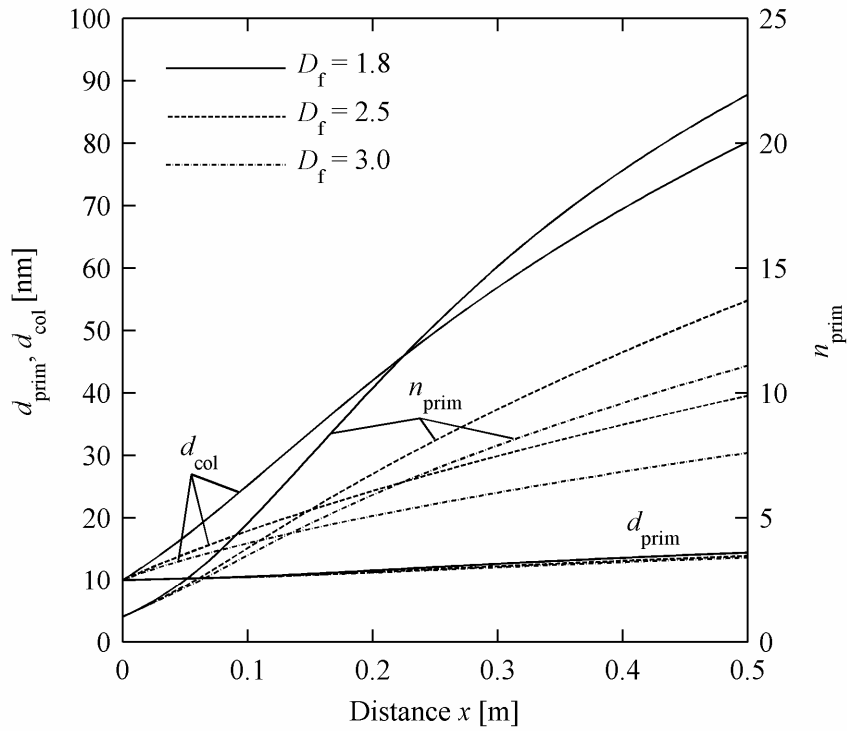


Figure 7.6: Evolution of primary particle size, number of primary particles per aggregate and collision diameter for $D_f = 1.8, 2.5$ and 3.0 at baseline parametric settings.

The effect of the sintering rate was investigated by increasing the rate by factors of 10 and 100. The corresponding evolutions of d_{prim} , d_{col} and n_{prim} are shown in Fig. 7.7. As expected, the collision diameter and the number of primary particles decrease for increase in sintering rate. Their final values are 80, 58 and 47 nm, and 22, 7 and 4 for factors 1, 10 and 100, respectively. The primary particle diameter is only slightly increasing from 14 to 19 and 26 nm.

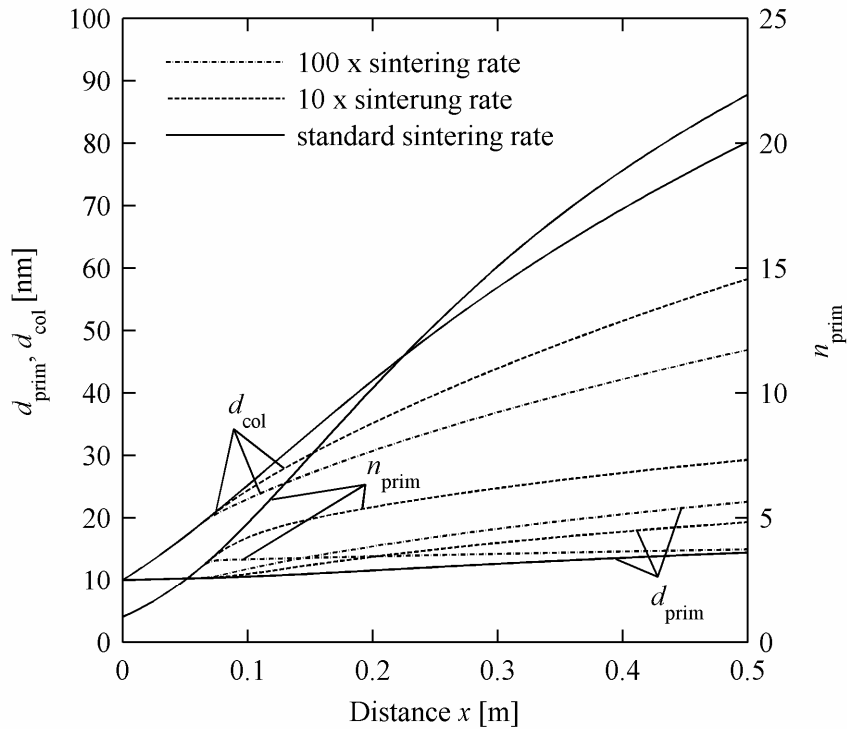


Figure 7.7: Evolution of primary particle size, number of primary particles per aggregate and collision diameter for standard sintering rate, a tenfold and a hundredfold increase in sintering rate at baseline parametric setting.

7.4 Summary and conclusions

A 1D monodisperse model which describes simultaneous aggregation, sintering, surface reaction, and Zn vapor and particle wall deposition by diffusion was used to simulate particle dynamics and chemical reaction in the reaction zone of the Zn hydrolysis reactor. Particles formed in the quench zone and entering the reaction zone were assumed to be perfectly coalesced with an initial ZnO content of 5%. Agreement between experimentally measured and numerically computed chemical conversions and particle ZnO contents were reasonably good. However, such good agreements were obtained at the expense of the discrepancy in specific surface area and primary particle size. Sintering of ZnO is very slow, resulting in only small changes of primary particle size. Increasing the initial primary particle size from 1 to 100 nm leads to a reduction in the decay of the number concentration along the reactor axis due to slower coagulation rates because of lower particle concentrations. Thus, small initial diameters of 1 nm lead to the formation of large agglomerates with collision diameter of up to

400 nm containing about 3.76×10^4 primary particles. Particles of 100 nm diameter hardly form agglomerates due to slow coagulation rates. Brownian coagulation is the dominant mechanism, while shear-induced coagulation is negligible. Particle deposition rates are small compared to coagulation rates, as only diffusion and no thermophoresis was considered. Increasing the sintering rate by a factor of 100 only leads to a slight increase of the primary particle diameter.

It should be noticed that the particle characteristics were determined in measurements after experiments from deposits collected in the reactor. In-situ measurements, revealing characteristics of gas borne particles in the flow, were not performed. The deposits may have undergone morphological changes as a great number of these particles remained immobilized for a long period in experiments lasting about 80 min. Further the possibility of re-entrained particles collected in the filter should be taken into consideration. On the other hand, the assumption of perfectly coalesced, spherical particles at the quench zone exit may not be correct. At high temperatures, coalescence of freshly formed Zn particles is probably very fast, resulting in spherical primary particles. As the temperature drops, decrease in sintering rate and formation of ZnO by chemical reaction on the particles may however lead to formation of agglomerates already in the quench unit. Meanwhile the change in particle size with reaction zone temperature is attributed to particle growth mechanisms taking place in the reaction zone, as the quench zone is believed to be influenced only to a low extent by the reaction zone temperature.

8 Summary and outlook

This work examined several aspects of hydrogen production by solar thermochemical processes. Investigations included experimentation and modeling of solar, endothermic processes such as high-temperature ZnO dissociation and production of syngas by steam-gasification of biomass-derived char, as well as non-solar, exothermic hydrolysis of Zn particles.

A solar chemical reactor using concentrated thermal radiation as the energy source of high-temperature process heat was designed, fabricated and tested. It consists of a cylindrical cavity-receiver containing a tubular absorber that serves as reaction chamber. A 2D steady-state reactor model was formulated using the Monte Carlo and finite difference techniques to solve the energy conservation equation coupling radiation, conduction, and convection heat transfer to chemical kinetics. Tests were performed in ETH's High-Flux Solar Simulator. In ZnO dissociation experiments, an Al₂O₃ absorber was used withstanding high temperatures above 2000 K. Numerically computed results were in reasonable good agreement with the experimentally measured reaction rates, performed in batch-mode experiments with pre-sintered ZnO plates in the range 1780–1975 K, and experimentally measured temperatures for runs under pure Ar flow without chemical reaction. Nearly completion of the reaction extent is predicted in simulations of a continuous flow process for ZnO dissociation at a reactor temperature of 2300 K with a maximum solar-to-chemical conversion efficiency of 28.5% at an input solar power per unit length of reactor of 40 kW/m. This corresponds to a total input power of 6 kW for a 15 cm length reaction zone. Continuous chemical process experiments were carried out in the temperature range 1873–2023 K. These experiments proved unsuccessful as no oxygen was detected in the off-gas and as further confirmed by identical particle size distributions and morphologies of feedstock and product particles. Experimental validation of continuous chemical process simulation was accomplished in 19 experimental runs with steam gasification of biochar. A SiC absorber tube was used with a maximum applicable temperature of 1623 K. Input power and absorber temperatures were in the range 0.76–1.68 kW and 1074–1523 K, respectively. The agreement between computed temperatures and carbon conversions and the experimentally measured values was reasonably good. A maximum carbon conversion of 26% was obtained experimentally at a temperature of 1425 K. The energy conversion efficiency was very low with a maximum of 1.53%, due to

low reactant feeding rates and short residence times resulting in relatively low carbon conversions. Simulations revealed that major heat losses of the lab-scale reactor were re-radiation through the aperture and conduction through the reactor walls. In contrast, only re-radiation losses are predominant in up-scaled reactors due to the favourable volume-to-surface ratio. The model was applied to two reactor versions featuring an eight-tube absorber array subjected to high-flux solar irradiation in the ranges 50 – 150 kW and 500 – 1500 kW. Theoretical maximum solar-to-chemical energy conversion efficiencies of 39.1 and 50.1% were found for 100 and 1000 kW power input at optimal feeding rates of 250 and 3250 g/min, respectively.

Obviously, the small dimensions are a major drawback of the lab-scale reactor, allowing only for relatively short residence times. This may pose problems with regard to efficient heat transfer, as observed in continuous-mode ZnO dissociation experiments. Nevertheless, this process has been successfully demonstrated with an alumina tube heated in an electrical furnace by Perkins et al. [57]. However, their reaction zone featured a diameter of 9.0275 cm and a length of 45.72 cm. These dimensions clearly exceed possible lab-scale reactor dimensions for testing in the High-Flux Solar Simulator. A further problem is related to possible temperature gradients along the reactor axis. The absorber tube has a total length of 35.5 cm, with its central part of 15 cm, which is here referred to as the reaction zone, directly exposed to concentrated thermal radiation. Due to the low thermal conductivity of Al_2O_3 , steep temperature gradients may be present in axial direction towards entrance and exit of the absorber tube. Products exiting the hot reaction zone have to travel another 10.05 cm through the absorber tube before reaching the quench unit. The temperature gradient then leads to recombination of Zn and O_2 in the absorber as observed in batch-mode experiments, where ZnO needles grew on the inner absorber surface. This could be improved by incorporating the quench unit right behind the hot reaction zone. Thermal conductivity of SiC is one order of magnitude higher than that of alumina. Hence, a more uniform temperature distribution along the SiC absorber tube axis can be expected. This is confirmed by the slight over-predictions of absorber temperatures in the 2D simulation, which does not account for conductive heat losses in axial direction. To a certain extent, pre-heating of reactants before entering the hot reaction zone may thereby occur. The horizontal alignment of the reactor requires relatively high gas flow rates in order to avoid deposition of particles. This results in very short residence times, as seen in biochar gasification experiments. A flow down reactor concept, featuring a vertical alignment that requires lower gas flow rates, could increase residence time. Finally, an amelioration of the ZnO feeding can be achieved by the use of a

spinning wheel feeder [57,120]. The reactor model evidently can be improved by extension to 3D, and by inclusion of combined radiation, conduction, and convection heat transfer inside the reaction zone.

In the second part of the work, hydrogen production by hydrolysis of Zn in a hot-wall aerosol flow reactor was investigated. Zn is evaporated from a ceramic crucible and carried by a nitrogen flow into the quench zone. Rapid cooling by a steam-nitrogen mixture results in nanoparticle formation by homogeneous nucleation and condensation. In-situ chemical reaction releasing H₂ and forming ZnO is achieved in the quench zone and the following reaction zone. The main challenge in this process is the combination of nanoparticle formation and simultaneous hydrolysis. High quench flow rates and steep temperature gradients are necessary for nanoparticle formation, whereas low flow rates, i.e. long residence times, and high temperatures are advantageous for chemical reaction. The challenge consists in finding the best trade-off between these aspects. In experimental investigations, the influence of quenching gas flow rate, Zn evaporation rate, and wall temperature on the chemical conversion, particle yield and ZnO content was examined. Cooling rates were in the range 2×10^4 to 1×10^6 K/s achieved by quench flow rates ranging from 1 to 25 l_n/min. The former leads to the formation of sharp-edged hexagonal particles with low ZnO content, controlled by Zn nucleation-condensation mechanism at long residence times. In contrast, filamentary and rod-like particles are obtained at high quench flow rates. Their formation is mainly controlled by coagulation and surface reaction. A maximum overall chemical conversion of 95% is found at a low quench flow rate of 1 l_n/min, mainly due to wall deposits in the quench unit at the expense of low particle yield on the filter. Varying the reaction zone temperature from 573 to 873 K, at high quench flow rate of 20 l_n/min, leads to an increase of chemical conversion from 42% to 66%. Particle yield decreased from 52% to 28%. A maximum ZnO content of 50% was found for filtered particles at 873 K. Particle ZnO content and particle yield on the filter are the most important performance indicators in the process. They have to be significantly increased for a large-scale industrial implementation. Elimination of wall deposits is crucial. Injection of an annular quenching flow [62] or the use of a fluid-wall tube [67] could reduce deposition and increase particle yield. At high quench flow rates, steep temperature drop was measured in the first 3 cm of the 25 cm long quench unit. Reducing the quench zone length could further reduce wall deposition.

Chemical reaction and particle dynamics in the reaction zone were simulated with a 1D monodisperse model accounting for aggregation, surface reaction, sintering, and Zn vapor

and particle wall deposition by diffusion. Numerically computed and experimentally measured chemical conversions and particle ZnO contents were in reasonable good agreement. However, a significant discrepancy between measured and computed specific surface areas and primary particle sizes was obtained. In experiments, particles were not characterized by in-situ measurements, but only by analysis of deposits collected from the filter after experiments. Analysis with a scanning differential mobility sizer or by thermophoretic sampling may give insight to particle formation dynamics in the flow field. The model may be extended to include the quench zone. In the present model, perfectly coalesced particles are assumed to exit the quench zone, which may be incorrect. Modeling of the quench zone would include particle formation by homogeneous nucleation and heterogeneous chemical reaction on the surface of these particles. Mass transfer plays an important role as Zn condensation/evaporation as well as ZnO formation on the surface of particles have to be considered. Further insight may be gained by coupling the particle dynamics model to computational fluid dynamics.

Appendix

The temperature of the inner absorber surface is derived from the temperature measured at the center of the absorber by a shielded thermocouple. Application of the radiosity method to the enclosure of Fig. A.1 yields a system of equations in terms of the net radiative heat fluxes and temperatures [16]:

$$\sum_{j=1}^N \left(\frac{\delta_{ij}}{\varepsilon_j} - F_{i-j} \frac{1-\varepsilon_j}{\varepsilon_j} \right) q_j = \sum_{j=1}^N (\delta_{ij} - F_{i-j}) \sigma T_j^4, \quad (\text{A.1})$$

for $i = 1..3$.

where $i = 1, 2$, and 3 refer to the shield, inner absorber, and outer absorber surfaces, respectively. The corresponding view factors are $F_{1-1} = 0$, $F_{1-2} = 1$, $F_{2-1} = A_1/A_2 = r_1/r_2$, and $F_{2-2} = 1 - A_1/A_2 = 1 - r_1/r_2$. Solving the system of equations yields $Q_1 = 2\pi r_1 \sigma (T_1^4 - T_2^4) / \psi$, with $\psi = \frac{1}{\varepsilon_1} + \frac{r_1}{r_2} \left(\frac{1}{\varepsilon_2} - 1 \right)$. Since $Q_1 = -Q_2 = \frac{2\pi k}{\ln(r_3/r_2)} (T_2 - T_3)$, the implicit equation for T_2 is

$$T_2 = \left[T_1^4 + k\psi (T_3 - T_2) / r_1 \sigma \ln(r_3/r_2) \right]^{1/4} \quad (\text{A.2})$$

which is solved iteratively.

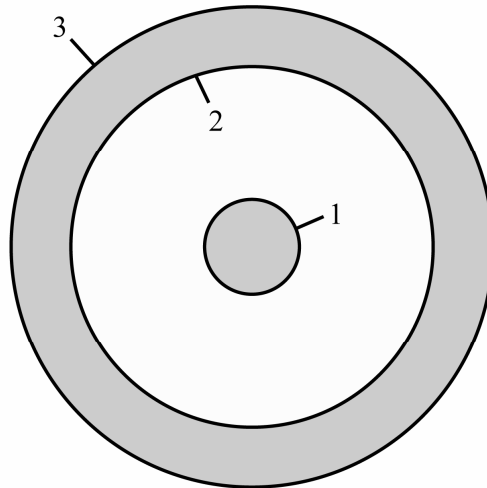


Figure A.1: Scheme of thermocouple (1: shield surface) placed concentric with the absorber (2: inner surface, 3: outer surface)

Bibliography

- [1] International Energy Outlook 2008. Energy Information Administration (2008).
- [2] A. Midilli and I. Dincer. Key strategies of hydrogen energy systems for sustainability. *International Journal of Hydrogen Energy* **32** (5): 511-524 (2007).
- [3] Climate Change 2007: Synthesis report. An Assessment of the Intergovernmental Panel on Climate Change IPCC, Valencia, Spain (2007).
- [4] I. Dincer and M.A. Rosen. A worldwide perspective on energy, environment and sustainable development. *International Journal of Energy Research* **22** (15): 1305-1321 (1998).
- [5] C. Perkins and A.W. Weimer. Solar-thermal production of renewable hydrogen. *A.I.Ch.E. Journal* **55** (2): 286-293 (2009).
- [6] A. Steinfeld. Solar thermochemical production of hydrogen – a review. *Solar Energy* **78** (5): 603-615 (2005).
- [7] P. v.Zedtwitz, J. Petrasch, D. Trommer and A. Steinfeld. Hydrogen production via the solar thermal decarbonization of fossil fuels. *Solar Energy* **80** (10): 1333-1337 (2006).
- [8] C. Perkins and A.W. Weimer. Likely near-term solar-thermal water-splitting technologies. *International Journal of Hydrogen Energy* **29** (15): 1587-1599 (2004).
- [9] A. Steinfeld. Solar hydrogen production via a two-step water-splitting thermochemical cycle based on Zn/ZnO redox reactions. *International Journal of Hydrogen Energy* **27** (6): 611-619 (2002).
- [10] A. Steinfeld, P. Kuhn, A. Reller, R. Palumbo, J. Murray and Y. Tamaura. Solar-processed metals as clean energy carriers and water-splitters. *International Journal of Hydrogen Energy* **23** (9): 767-774 (1998).
- [11] E. Bilgen, M. Ducarroir, M. Foex, F. Sibieude and F. Trombe. Use of solar energy for direct and two-step water decomposition cycles. *International Journal of Hydrogen Energy* **2** (3): 251-257 (1977).

- [12] R. Palumbo, J. Lédé, O. Boutin, E. Elorza Ricart, A. Steinfeld, S. Möller, A. Weidenkaff, E.A. Fletcher and J. Bielicki. The production of Zn from ZnO in a high-temperature solar decomposition quench process – I. The scientific framework of the process. *Chemical Engineering Science* **53** (14): 2503-2517 (1998).
- [13] S. Abanades, P. Charvin, G. Flamant and P. Neveu. Screening of water-splitting thermochemical cycles potentially attractive for hydrogen production by concentrated solar energy. *Energy* **31** (14): 2805-2822 (2006).
- [14] R. Felder and A. Meier. Well-to-wheel analysis of solar hydrogen production and utilization for passenger car transportation. *ASME Journal of Solar Energy Engineering* **130** (1): 011017 (2008).
- [15] A. Steinfeld and R. Palumbo. Solar Thermochemical Process Technology. In: R.A. Meyers (ed.). *Encyclopedia of Physical Science & Technology, Vol. 15*. pp. 237-256. Academic Press, San Diego (2001).
- [16] R. Siegel and J.R. Howell. *Thermal Radiation Heat Transfer*, 4th Ed. Taylor & Francis, New York – London (2002).
- [17] S.H. Lin and E.M. Sparrow. Radiant interchange among curved specularly reflecting surfaces – application to cylindrical and conical cavities. *ASME Journal of Heat Transfer* **87** (2): 299-307 (1965).
- [18] A. Steinfeld. Apparent absorptance for diffusely and specularly reflecting spherical cavities. *International Journal of Heat and Mass Transfer* **34** (7): 1895-1897 (1991).
- [19] A. Steinfeld and M. Schubnell. Optimum aperture size and operating temperature of a solar cavity-receiver. *Solar Energy* **50** (1): 19-25 (1993).
- [20] W.T. Welford and R. Winston. *High Collection Nonimaging Optics*. Academic Press, San Diego (1989).
- [21] P. Haueter, S. Moeller, R. Palumbo and A. Steinfeld. The production of zinc by thermal dissociation of zinc oxide – solar chemical reactor design. *Solar Energy* **67** (1-3): 161-167 (1999).

- [22] S. Möller and R. Palumbo. The development of a solar chemical reactor for the direct thermal dissociation of zinc oxide. *ASME Journal of Solar Energy Engineering* **123** (2): 83-90 (2001).
- [23] R. Müller, P. Haeberling and R.D. Palumbo. Further advances toward the development of a direct heating solar thermal chemical reactor for the thermal dissociation of ZnO(s). *Solar Energy* **80** (5): 500-511 (2006).
- [24] R. Müller, W. Lipiński and A. Steinfeld. Transient heat transfer in a directly-irradiated solar chemical reactor for the thermal dissociation of ZnO. *Applied Thermal Engineering* **28** (5-6): 524-531 (2008).
- [25] L.O. Schunk, P. Haeberling, S. Wepf, D. Wuillemin, A. Meier and A. Steinfeld. A receiver-reactor for the solar thermal dissociation of zinc oxide. *ASME Journal of Solar Energy Engineering* **130** (2): 021009 (2008).
- [26] C. Wieckert, A. Meier and A. Steinfeld. Indirectly irradiated solar receiver-reactors for high-temperature thermochemical processes. *ASME Journal of Solar Energy Engineering* **125** (1): 120-123 (2003).
- [27] A. Z'Graggen and A. Steinfeld. Radiative exchange within a two-cavity configuration with a spectrally selective window. *ASME Journal of Solar Energy Engineering* **126** (2): 819-822 (2004).
- [28] T. Melchior and A. Steinfeld. Radiative transfer within a cylindrical cavity with diffusely/specularly reflecting inner walls containing an array of tubular absorbers. *ASME Journal of Solar Energy Engineering* **130** (2): 021013 (2008).
- [29] D. Hirsch, P. v.Zedtwitz, T. Osinga, J. Kinamore and A. Steinfeld. A new 75 kW high-flux solar simulator for high-temperature thermal and thermochemical research. *ASME Journal of Solar Energy Engineering* **125** (1): 117-120 (2003).
- [30] Zircar Zirconia, Inc. Product Data Bulletin #A-D. www.zircarzirconia.com/doc/A-D_FBD.pdf (2006).
- [31] McDanel Advanced Ceramic Technologies. www.mcdanelceramics.com.

- [32] W. Haldenwanger Technische Keramik GmbH & Co.KG. HALSIC-R/-RX/-I/-S Silicon carbide special materials Catalogue. www.haldenwanger.de (2007).
- [33] M.F. Modest. Three-dimensional radiative exchange factors for nongray, nondiffuse surfaces. *Numerical Heat Transfer* **1** (3): 403-416 (1978).
- [34] Y.S. Touloukian and D.P. DeWitt. *Thermophysical Properties of Matter, Volume 15. Thermal Radiative Properties: Nonmetallic Solids*. IFI/Plenum, New York, Washington (1972).
- [35] Y.S. Touloukian, R.W. Powell, C.Y. Ho and P.G. Klemens. *Thermophysical Properties of Matter, Volume 2. Thermal Conductivity: Nonmetallic Solids*. IFI/Plenum, New York, Washington (1970).
- [36] T.H. Kuehn and R.J. Goldstein. Correlating equations for natural convection heat transfer between horizontal circular cylinders. *International Journal of Heat and Mass Transfer* **19** (10): 1127-1134 (1976).
- [37] M.J. Shilston and S.D. Probert. Thermal insulation provided by plain, horizontal annular cavities containing atmospheric pressure air. *Applied Energy* **5** (1): 61-80 (1979).
- [38] R.F. Babus'Haq, S.D. Probert and M.J. Shilston. Natural convection across cavities: design advice. *Applied Energy* **20** (3): 161-188 (1985).
- [39] R.F. Babus'Haq and S.D. Probert. Finite-element analysis of natural convections across horizontal air-filled cavities each surrounding a heated pipe. *Applied Energy* **30** (1): 15-28 (1988).
- [40] F.P. Incropera and D.P. DeWitt. *Fundamentals of Heat and Mass Transfer*, 5th Ed. John Wiley & Sons (2002).
- [41] A.M. Clausing, J.M Waldvogel and L.D. Lister. Natural convection from isothermal cubical cavities with a variety of side facing apertures. *ASME Journal of Heat Transfer* **109** (2): 407-412 (1987).
- [42] W.B. Stine and C.G. McDonald. Cavity receiver heat loss measurements. In: *Proceedings of ISES World Congress*. Kobe, Japan (1989).

- [43] U. Leibfried and J. Ortjohann. Convective heat loss from upward and downward-facing cavity solar receivers: measurements and calculations. *ASME Journal of Solar Energy Engineering* **117** (2): 75-84 (1995).
- [44] T. Taumoefolau, S. Paitoonsurikarn, G. Hughes and K. Lovegrove. Experimental investigation of natural convection heat loss from a model solar concentrator cavity receiver. *ASME Journal of Solar Energy Engineering* **126** (2): 801-807 (2004).
- [45] N. Sendhil Kumar and K.S. Reddy. Numerical investigation of natural convection heat loss in modified cavity receiver for fuzzy focal solar dish concentrator. *Solar Energy* **81** (7): 846-855 (2007).
- [46] K.S. Reddy and N. Sendhil Kumar. Combined laminar natural convection and surface radiation heat transfer in a modified cavity receiver of solar parabolic dish. *International Journal of Thermal Sciences* **47** (12): 1647-1657 (2008).
- [47] D. Hess. CFD modeling of convective heat loss from an upward-facing cavity solar receiver. Semester Thesis, ETH Zurich, Zurich (2007).
- [48] ANSYS CFX 10.0 (ANSYS, Inc., 2005).
- [49] S. Möller and R. Palumbo. Solar thermal decomposition kinetics of ZnO in the temperature range 1950-2400 K. *Chemical Engineering Science* **56** (15): 4505-4515 (2001).
- [50] S.H.P. Chen and S.C. Saxena. Thermal conductivity of argon in the temperature range 350 to 2500 K. *Molecular Physics* **29** (2): 455-466 (1975).
- [51] C.L. Yaws. *Chemical Properties Handbook*. McGraw-Hill, New York, NY (1999).
- [52] O. Levenspiel. *Chemical Reaction Engineering*. John Wiley & Sons, New York, NY (1999).
- [53] N. Piatkowski and A. Steinfeld. Solar-driven coal gasification in a thermally irradiated packed-bed reactor. *Energy & Fuels* **22** (3): 2043-2052 (2008).
- [54] A. Z'Graggen and A. Steinfeld. Heat and mass transfer analysis of a suspension of reacting particles subjected to concentrated solar radiation – application to the steam-

- gasification of carbonaceous materials. *International Journal of Heat and Mass Transfer* **52** (1-2): 385-395 (2009).
- [55] G. Maag, W. Lipiński and A. Steinfeld. Particle-gas reacting flow under concentrated solar irradiation. *International Journal of Heat and Mass Transfer* **52** (21-22): 4997-5004 (2009).
- [56] J. Lédé, E. Elorza-Ricart and M. Ferrer. Solar thermal splitting of zinc oxide: a review of some of the rate controlling factors. *ASME Journal of Solar Energy Engineering* **123** (2): 91-97 (2001).
- [57] C. Perkins, P.R. Lichty and A.W. Weimer. Thermal ZnO dissociation in a rapid aerosol reactor as part of a solar hydrogen production cycle. *International Journal of Hydrogen Energy* **33** (2): 499-510 (2008).
- [58] I. Alxneit. Assessing the feasibility of separating a stoichiometric mixture of zinc vapor and oxygen by a fast quench – Model calculations. *Solar Energy* **82** (11): 959-964 (2008).
- [59] M. Karlsson, I. Alxneit, F. Rütten, D. Willemin and H.R. Tschudi. A compact setup to study homogeneous nucleation and condensation. *Review of Scientific Instruments* **78** (3): 034102 (2007).
- [60] F. Rütten, I. Alxneit and H.R. Tschudi. Kinetics of homogeneous nucleation and condensation of *n*-butanol at high supersaturation. *Atmospheric Research* **92** (1): 124-130 (2009).
- [61] R. Müller and A. Steinfeld. H₂O-splitting thermochemical cycle based on ZnO/Zn-redox: quenching the effluents from the ZnO dissociation. *Chemical Engineering Science* **63** (1): 217-227 (2008).
- [62] D. Gstoehl, A. Brambilla, L.O. Schunk and A. Steinfeld. A quenching apparatus for the gaseous products of the solar thermal dissociation of ZnO. *Journal of Materials Science* **43** (14): 4729-4736 (2008).

- [63] E.A. Fletcher. Solar-thermal and solar quasi-electrolytic processing and separations: zinc from zinc oxide as an example. *Industrial Engineering Chemistry Research* **38** (6): 2275-2282 (1999).
- [64] A. Weidenkaff, A.W. Reller, A. Wokaun and A. Steinfeld. Thermogravimetric analysis of the ZnO/Zn water splitting cycle. *Thermochimica Acta* **359** (1): 69-75 (2000).
- [65] C. Perkins, P. Lichty and A.W. Weimer. Determination of aerosol kinetics of thermal ZnO dissociation by thermogravimetry. *Chemical Engineering Science* **62** (21): 5952-5962 (2007).
- [66] L.O. Schunk and A. Steinfeld. Kinetics of the thermal dissociation of ZnO exposed to concentrated solar irradiation using a solar-driven thermogravimeter in the 1800-2100 K range. *A.I.Ch.E. Journal* **55** (6): 1497-1504 (2009).
- [67] C. Perkins, P. Lichty, A.W. Weimer and C. Bingham. Fluid-wall effectiveness for preventing oxidation in solar-thermal ZnO reactors. *A.I.Ch.E. Journal* **53** (7): 1830-1844 (2007).
- [68] J.K. Dahl, K.J. Buechler, A.W. Weimer, A. Lewandowski and C. Bingham. Solar-thermal dissociation of methane in a fluid-wall aerosol flow reactor. *International Journal of Hydrogen Energy* **29** (7): 725-736 (2004).
- [69] J. Lédé. Solar thermochemical conversion of biomass. *Solar Energy* **65** (1): 3-13 (1999).
- [70] J.P. Murray and E.A. Fletcher. Reaction of steam with cellulose in a fluidized-bed using concentrated sunlight. *Energy* **19** (10): 1083-1098 (1994).
- [71] P. von Zedtwitz and A. Steinfeld. Steam-gasification of coal in a fluidized-bed/packed-bed reactor exposed to concentrated thermal radiation – modeling and experimental validation. *Industrial & Engineering Chemistry Research* **44** (11): 3852-3861 (2005).
- [72] A. Z'Graggen, P. Haueter, D. Trommer, M. Romero, J.C. de Jesus and A. Steinfeld. Hydrogen production by steam-gasification of petroleum coke using concentrated solar power – II Reactor design, testing, and modelling. *International Journal of Hydrogen Energy* **31** (6): 797-811 (2006).

- [73] A. Z'Graggen, P. Haueter, G. Maag, M. Romero and A. Steinfeld. Hydrogen production by steam-gasification of carbonaceous materials using concentrated solar power – IV. Reactor experimentation with vacuum residue. *International Journal of Hydrogen Energy* **33** (2): 679-684 (2008).
- [74] R. Adinberg, M. Epstein and J. Karni. Solar gasification of biomass: a molten salt pyrolysis study. *ASME Journal of Solar Energy Engineering* **126** (3): 850-857 (2004).
- [75] J. Feroso, B. Arias, C. Pevida, M.G. Plaza, F. Rubiera and J.J. Pis. Kinetic models comparison for steam gasification of different nature fuel chars. *Journal of Thermal Analysis and Calorimetry* **91** (3): 779-786 (2008).
- [76] F. Mermoud, S. Salvador, L. Van de Steene and F. Golfier. Influence of the pyrolysis heating rate on the steam gasification rate of large wood char particles. *Fuel* **85** (10-11): 1473-1482 (2006).
- [77] F. Mermoud, F. Golfier, S. Salvador, L. Van de Steene and J.L. Dirion. Experimental and numerical study of steam gasification of a single charcoal particle. *Combustion and Flame* **145** (1-2): 59-79 (2006).
- [78] S.T. Chaudhari, S.K. Bej, N.N. Bakhshi and A.K. Dalai. Steam gasification of biomass-derived char for the production of carbon monoxide-rich synthesis gas. *Energy & Fuels* **15** (3): 736-742 (2001).
- [79] S.T. Chaudhari, A.K. Dalai and N.N. Bakhshi. Production of hydrogen and/or syngas (H₂ + CO) via steam gasification of biomass-derived chars. *Energy & Fuels* **17** (4): 1062-1067 (2003).
- [80] A. Roine. *Outokumpu HSC Chemistry for Windows*. Outokumpu Research, Pori, Finland (1997).
- [81] H. Netz. *Verbrennung und Gasgewinnung bei Festbrennstoffen*. Resch, Gräfeling/München (1982).
- [82] F. Rizk. Pneumatic conveying at optimal operation conditions and a solution of Barth's equation. In: *Proceedings of Pneumotransport 3*, paper D4: pp. 43-58, Bedford, U.K. (1976).

- [83] M.J.A. Tijmensen, A.P.C. Faaij, C.N. Hamelinck and M.R.M. van Hardeveld. Exploration of the possibilities for production of Fischer Tropsch liquids and power via biomass gasification. *Biomass & Bioenergy* **23** (2): 129-152 (2002).
- [84] A. Berman and M. Epstein. The kinetics of hydrogen production in the oxidation of liquid zinc with water vapour. *International Journal of Hydrogen Energy* **25** (10): 957-967 (2000).
- [85] I. Vishnevetsky and M. Epstein. Production of hydrogen from solar zinc in steam atmosphere. *International Journal of Hydrogen Energy* **32** (14): 2791-2802 (2007).
- [86] J.A. Clarke and D.J. Fray. Oxidation of zinc vapour by hydrogen-water vapour mixtures. *Transactions of the Institution of Mining and Metallurgy Section C – Mineral Processing and Extractive Metallurgy* **88**: C161-C166 (1979).
- [87] A. Weidenkaff, A. Steinfeld, A. Wokaun, P.O. Auer, B. Eichler and A. Reller. Direct solar thermal dissociation of zinc oxide: condensation and crystallisation of zinc in the presence of oxygen. *Solar Energy* **65** (1): 59-69 (1999).
- [88] K. Wegner, H.C. Ly, R.J. Weiss, S.E. Pratsinis and A. Steinfeld. Process and apparatus for producing concurrently hydrogen or ammonia and metal oxide nanoparticles. EU Patent PCT/CH 2005/00315 Filed 3/06/05, and US 11/628,271 Filed 12/04/06.
- [89] R.J. Weiss, H.C. Ly, K. Wegner, S.E. Pratsinis and A. Steinfeld. H₂ production by Zn hydrolysis in a hot-wall aerosol reactor. *A.I.Ch.E. Journal* **51** (7): 1966-1970 (2005).
- [90] K. Wegner, H.C. Ly, R.J. Weiss, S.E. Pratsinis and A. Steinfeld. In situ formation and hydrolysis of Zn nanoparticles for H₂ production by the 2-step ZnO/Zn water-splitting thermochemical cycle. *International Journal of Hydrogen Energy* **31** (1): 55-61 (2006).
- [91] F.O. Ernst, A. Tricoli, S.E. Pratsinis and A. Steinfeld. Co-synthesis of H₂ and ZnO by in-situ aerosol formation and hydrolysis. *A.I.Ch.E. Journal* **52** (9): 3297-3303 (2006).
- [92] T. Abu Hamed, J.H. Davidson and M. Stolzenburg. Hydrogen production via hydrolysis of Zn in a hot wall flow reactor. *ASME Journal of Solar Energy Engineering* **130** (4): 041010 (2008).

- [93] H.H. Funke, H. Diaz, X. Liang, C.S. Carney, A.W. Weimer and P. Li. Hydrogen generation by hydrolysis of zinc powder aerosol. *International Journal of Hydrogen Energy* **33** (4): 1127-1134 (2008).
- [94] K. Wegner, B. Walker, S. Tsantilis and S.E. Pratsinis. Design of metal nanoparticle synthesis by vapour flow condensation. *Chemical Engineering Science* **57** (10): 1753-1762 (2002).
- [95] N. Piatkowski. Zn-nanoparticle in-situ hydrolysis for hydrogen production in a high quench rate reactor. Master Thesis, ETH Zurich, Zurich (2007).
- [96] R.W. Cheary and A.A. Coelho. Axial divergence in a conventional X-ray powder diffractometer. I: theoretical foundations. *Journal of Applied Crystallography* **31** (6): 851-861 (1998).
- [97] S. Polarz, A. Roy, M. Merz, S. Halm, D. Schröder, L. Schneider, G. Bacher and F. E. Kruis. Chemical vapor synthesis of size-selected zinc oxide nanoparticles. *Small* **1** (5): 540-552 (2005).
- [98] S.E. Pratsinis and K.S. Kim. Particle coagulation, diffusion and thermophoresis in laminar tube flows. *Journal of Aerosol Science* **20** (1): 101-111 (1989).
- [99] K.A. Kusters and S.E. Pratsinis. Strategies for control of ceramic powder synthesis by gas-to-particle conversion. *Powder Technology* **82** (1): 79-91 (1995).
- [100] G.D. Ulrich and J.W. Riehl. Aggregation and growth of submicron oxide particles in flames. *Journal of Colloid and Interface Science* **87** (1): 257-265 (1982).
- [101] W. Koch and S.K. Friedlander. Particle growth by coalescence and agglomeration. *Particle & Particle Systems Characterization* **8** (1): 86-89 (1991).
- [102] Y. Xiong and S.E. Pratsinis. Formation of agglomerate particles by coagulation and sintering – Part I. A two-dimensional solution of the population balance equation. *Journal of Aerosol Science* **24** (3): 283-300 (1993).
- [103] Y. Xiong, M.K. Akhtar and S.E. Pratsinis. Formation of agglomerate particles by coagulation and sintering – Part II. The evolution of the morphology of aerosol-made

- titania, silica and silica-doped titania powders. *Journal of Aerosol Science* **24** (3): 301-313 (1993).
- [104] Y. Xiong, S.E. Pratsinis and A.W. Weimer. Modeling the formation of boron carbide particles in an aerosol flow reactor. *A.I.Ch.E. Journal* **38** (11): 1685-1692 (1992).
- [105] F.E. Kruis, K.A. Kusters and S.E. Pratsinis. A simple model for the evolution of the characteristics of aggregate particles undergoing coagulation and sintering. *Aerosol Science and Technology* **19** (4): 514-526 (1993).
- [106] T. Matsoukas and S.K. Friedlander. Dynamics of aerosol agglomerate formation. *Journal of Colloid and Interface Science* **146** (2): 495-506 (1991).
- [107] S. Tsantilis, H.K. Kammler and S.E. Pratsinis. Population balance modeling of flame synthesis of titania nanoparticles. *Chemical Engineering Science* **57** (12): 2139-2156 (2002).
- [108] J.I. Jeong and M. Choi. A bimodal particle dynamics model considering coagulation, coalescence and surface growth, and its application to the growth of titania aggregates. *Journal of Colloid and Interface Science* **281** (2): 351-359 (2005).
- [109] A. Schild, A. Gutsch, H. Mühlenweg and S.E. Pratsinis. Simulation of nanoparticle production in premixed aerosol flow reactors by interfacing fluid mechanics and particle dynamics. *Journal of Nanoparticle Research* **1** (2): 305-315 (1999).
- [110] R.N. Grass, S. Tsantilis and S.E. Pratsinis. Design of high-temperature, gas-phase synthesis of hard or soft TiO₂ agglomerates. *A.I.Ch.E. Journal* **52** (4): 1318-1325 (2006).
- [111] M.C. Heine and S.E. Pratsinis. Agglomerate TiO₂ aerosol dynamics at high concentrations. *Particle & Particle Systems Characterization* **24** (1): 56-65 (2007).
- [112] A. Erriguible, F. Marias, F. Cansell and C. Aymonier. Monodisperse model to predict the growth of inorganic nanostructured particles in supercritical fluids through coalescence and aggregation mechanism. *Journal of Supercritical Fluids* **48** (1): 79-84 (2009).

- [113] F.O. Ernst. Co-Synthesis of H₂ and nanocrystalline ZnO particles by Zn aerosol formation and in-situ hydrolysis. PhD Thesis, ETH Zurich, Zurich (2007).
- [114] F.O. Ernst, A. Steinfeld and S.E. Pratsinis. Hydrolysis rate of submicron Zn particles for solar H₂ synthesis. *International Journal of Hydrogen Energy* **34** (3): 1166-1175 (2009).
- [115] S.W. Lyons, Y. Xiong, T.L. Ward, T.T. Kodas and S.E. Pratsinis. Role of particle evaporation during synthesis of lead oxide by aerosol decomposition. *Journal of Materials Research* **7** (12): 3333-3341 (1992).
- [116] E.W. McDaniel. *Collision Phenomena in Ionized Gases*. Wiley, New York (1964).
- [117] D.L. Swift and S.K. Friedlander. The coagulation of hydrosols by Brownian motion and laminar shear flow. *Journal of Colloid Science* **19** (7): 621-647 (1964).
- [118] J.H. Seinfeld. *Atmospheric Chemistry and Physics of Air Pollution*. John Wiley & Sons, New York (1986).
- [119] C.R. Kaplan and J.W. Gentry. Agglomeration of chain-like combustion aerosols due to Brownian motion. *Aerosol Science and Technology* **8** (1): 11-28 (1988).
- [120] T.M. Francis, C.J. Gump and A.W. Weimer. Spinning wheel powder feeding device – fundamentals and applications. *Powder Technology* **170** (1): 36-44 (2006).

Curriculum vitae

Name: Tom Melchior
Nationality: Luxembourgish
Date of birth: September 2nd, 1979

2005-2009 Doctoral studies at the Professorship in Renewable Energy Carriers, ETH Zurich; supervision: Prof. Dr. Aldo Steinfeld
1999-2005 Diploma studies in Mechanical Engineering at ETH Zurich
1992-1999 Athénée de Luxembourg, section B: mathématiques et sciences physiques

Publications

T. Melchior and A. Steinfeld. Radiative transfer within a cylindrical cavity with diffusely/specularly reflecting inner walls containing an array of tubular absorbers. *ASME Journal of Solar Energy Engineering* **130** (2): 021013 (2008).

T. Melchior, C. Perkins, A.W. Weimer and A. Steinfeld. A cavity-receiver containing a tubular absorber for high-temperature thermochemical processing using concentrated solar energy. *International Journal of Thermal Sciences* **47** (11): 1496-1503 (2008).

T. Melchior, N. Piatkowski and A. Steinfeld. H₂ production by steam-quenching of Zn vapor in a hot-wall aerosol flow reactor. *Chemical Engineering Science* **64** (5): 1095-1101 (2009).

T. Melchior, C. Perkins, P. Lichty, A.W. Weimer and A. Steinfeld. Solar-driven biochar gasification in a particle-flow reactor. *Chemical Engineering and Processing* **48** (8): 1279-1287 (2009).

Conference presentations

T. Melchior and A. Steinfeld. Radiative transfer within a cylindrical cavity with diffusely/specularly reflecting inner walls containing an array of tubular absorbers. Oral presentation at the ASME International Solar Energy Conference, Denver, CO, USA, July 2006.